UNIVERSITÀ DEGLI STUDI DI PADOVA

DIPARTIMENTO DI SCIENZE CHIMICHE

LAUREA MAGISTRALE IN CHIMICA INDUSTRIALE

TESI DI LAUREA MAGISTRALE

Synthesis under Ultra-High Vacuum conditions of MoS2 thin films for Hydrogen Production

Relatore: Prof. Stefano Agnoli
Corelatore: Dr. Mattia Cattelan
Controrelatore: Prof.ssa Sabina Antonello

Laureando: Giancarlo Milotti

ANNO ACCADEMICO 2023/2024

Abstract

Disolfuri di metalli di transizione sono materiali che hanno suscitato interesse negli ultimi anni, data la loro capacità di catalizzare la reazione di evoluzione di evoluzione di ossigeno. A questo proposito in questo lavoro è stato depositato Molibdeno Disolfuro su un cristallo singolo di Au (111), in condizioni di ultra-alto vuoto, mediante Physical Vapor Deposition (PVD) di Molibdeno e Zolfo. Inoltre, viene osservata l'interazione tra Molibdeno Disolfuro e Ferro o Ferro Disolfuro. Il materiale viene poi caratterizzato mediante X-ray Photoelectron Spectroscopy, Low Energy Electron Diffraction and Scanning Tunneling Microscopy.

Transition metal disulfides are materials that have attracted interest in recent years, given their ability to catalyze the oxygen evolution reaction. In this regard, in this work Molybdenum Disulfide was deposited on a single crystal of Au (111), under ultra-high vacuum conditions, by Physical Vapor Deposition (PVD) of Molybdenum and Sulfur. Furthermore, the interaction between Molybdenum Disulfide and Iron or Iron Disulfide is observed. The material is then characterized using X-ray Photoelectron Spectroscopy, Low Energy Electron Diffraction and Scanning Tunneling Microscopy.

Index

Acronyms used in this work

ADL - Atomic Layer Deposition

AEMWE - Anion Exchange Membrane Water Electrolyzers

AWE - Alkaline Water Electrolyzers

BE - Binding Energy

CAPEX – Capital Expense

CVD - Chemical Vapor Deposition

HER – Hydrogen Evolution Reaction

KE – Kinetic Energy

LEED - Low Energy Electron Diffraction

MEA - Membrane Electrode Assembly

NGSR – Natural Gas Steam Reforming

OER – Oxygen Evolution Reaction

OPEX – Operating Expense

PEMWE - Proton Exchange Membrane Water Electrolyzers

PVD - Physical Vapor Deposition

SCE - Standard Calomel Electrode

SOE - Solid Oxide Electrolyzers

STM - Scanning Tunneling Microscopy

UHV – Ultra-High Vacuum

XPS - X-ray Photoelectron Spectroscopy

Chapter 1 - Introduction

Ever since they were first introduced for industrial purposes, the use of catalysts has grown exponentially due to the necessity to obtain specific products or drive chemical reactions at lower and lower energies. Energy production and consumption, in particular, has become a critical aspect of technological development in chemistry and material science, industrial production, transportation, and everyday life. [1]

Much of the energy production still relies on fossil fuels, such as coal and petrol, because these energy sources remain cheap to extract and refine, and the design of engines powered by these fuels is very well established. Emissions of CO_2 related to energy production make up between 70 and 73% of total carbon emissions with about 14 to 16% of emissions related to transportation, about 21 to 25% related to industrial requirements, and 17 to 25% related to energy use in buildings (figure 1.1). [2,3]

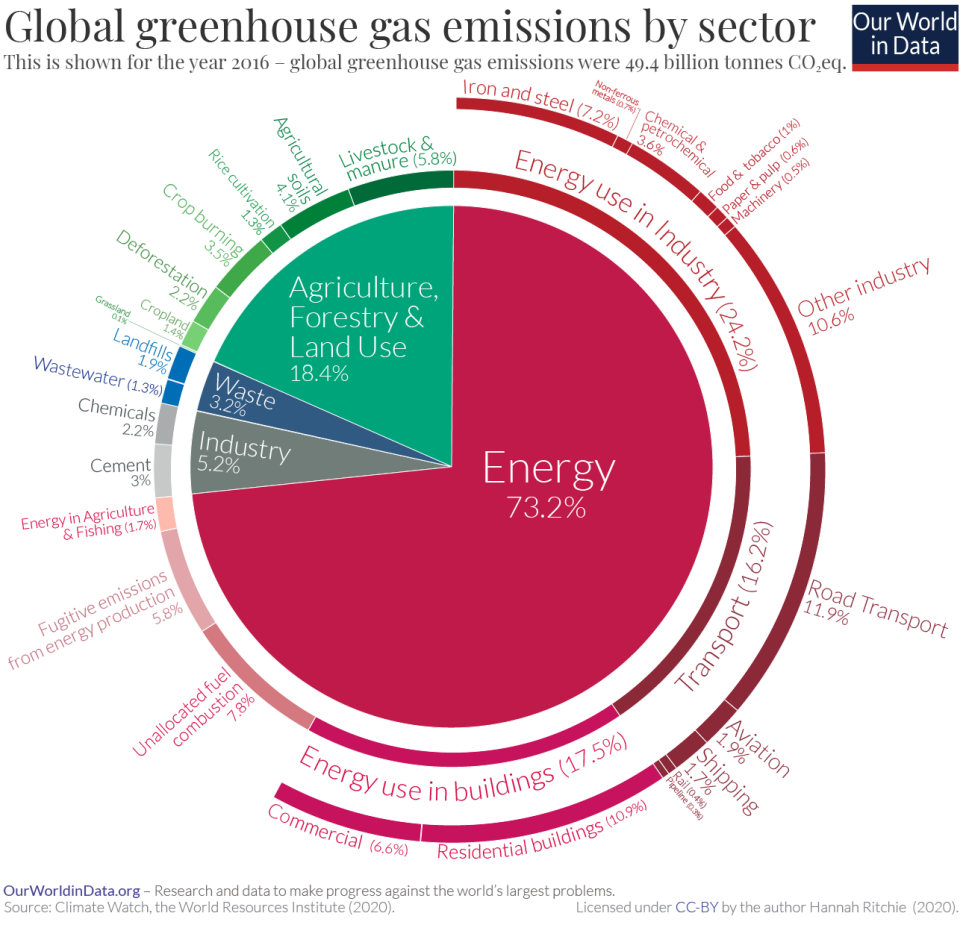

Figure 1.1 - Greenhouse gas emissions by sector.

The excess CO_2 produced by the combustion of fossil fuels is responsible for the increase in the average global temperature, having tipped the balance between carbon emissions and carbon capture. Because of the greenhouse gasses released into the atmosphere, not only by burning fossil fuels but also in the extraction

and refination processes, alternative energy production means have become not only convenient but necessary. [2–4]

Hydrogen is cited as a possible alternative to fossil fuel, either as a direct combustible or in fuel cells, but there are still issues in the implementation of these technologies, mainly due to production and storage difficulties and also because of safety concerns due to the extremely high explosive limits of hydrogen. [5–7] Despite these limitations and concerns, hydrogen presents many advantages, such as being non-toxic, having exceptional energy per mass content, being producible practically anywhere through electrolysis, and being an infinitely renewable resource; moreover, safety concerns can be addressed by proper storage and equipment maintenance. [5,7]

In the present day, several methods of hydrogen production are available, both at the industrial and experimental scale, and many of them have already been marketed as “blue”, “grey”,” white”, and “green” hydrogen, according to the environmental impact of their production. [8]

Steam reforming of natural gas makes up the vast majority of hydrogen production, with about 48% of all hydrogen being produced through this process. Another 30% of hydrogen is produced through petroleum fraction, 18% through coal gasification, and only 4% through electrolysis. Most of the alternative ways to produce hydrogen are still either not efficient or affordable, but a shift is possible and novel hydrogen production methods are evolving to be both highly efficient, sustainable, and cheaper. [5,7,9]

A brief review of the main methods of hydrogen production will be presented in the following sections; currently, there are other ways to produce hydrogen that include biomass gasification and reforming, production through microorganisms, and photocatalyzed water splitting, but many of these pathways are still not mature to be implemented at an industrial level. [7]

1.1 Hydrogen Production

1.1.1 Hydrogen production from hydrocarbons and fossil fuels

Production of hydrogen still relies heavily on fossil fuels, because it is based around the reactions of steam cracking and reforming of hydrocarbons, and due to energy requirements. Also, since it has not been economically viable to stock hydrogen thus far, production is performed on an “as-needed” basis.

The industrial process of steam reforming of natural gas involves the reactions of steam-hydrocarbon reforming, the partial oxidations of hydrocarbons, and the water-gas shift reaction, all of which contribute to the formation of molecular hydrogen. [7,10,11]

The reaction of Natural Gas Steam Reforming (NGSR) takes place at pressures between 3 to 25 bar [7,10] and at temperatures between 700 and 850 °C [7], involving the reaction:

$$CH_4 + H_2O + heat \rightarrow CO + 3H_2$$

In a more general form:

$$C_mH_n + m\,H_2O + heat \rightarrow m\,CO + \left(m + \frac{n}{2}\right) H_2$$ [7,10–12]

The reaction includes an output of about 12% CO by volume and this byproduct is used to convert more steam to CO_2 and H_2, through the water-gas shift reaction, with the equation:

$$CO + H_2O \rightarrow CO_2 + H_2 + heat$$

Due to the presence of oxygen in the reactor, the partial oxidation of hydrocarbons can occur, however, this oxidation is desirable, since it provides another pathway to produce hydrogen and CO, which can be further utilized in the water-gas shift reaction. The partial oxidation of hydrocarbons has the equation:

$$CH_4 + O_2 \rightarrow CO + 2H_2 + heat$$ [7,10–13]

One of the major costs of NGSR is the purification of the output gas, although it is possible to improve the efficiency of NGSR by the use of membrane reactors or reforming modules.[7,13]

Autothermal Reforming is a combination of steam reforming and partial oxidation of hydrocarbons, but it can be demanding due to high temperatures, between 950 and 1000 °C, and higher pressures, up to 100 bar. [7,12]

Similarly, hydrogen can be produced by a variety of processes of gasification of coal, with the general reaction:

$$C(s) + H_2O + heat \rightarrow CO + H_2$$

The carbon converted to CO is further oxidized to CO_2 and H_2O through the water-gas shift reaction. [7,14,15] Coal gasification and subsequent hydrogen production occur at temperatures over 900 °C by various techniques, such as fixed bed gasification, moving bed gasification, fluidized bed gasification, entrained bed gasification, and plasma gasification. The yield of the reaction can be improved with the addition of alkaline catalysts such as NaOH, K_2CO_3, or even CaO in the reactor, which captures the CO_2 that results from the water-gas shift reaction. [14,15]

One last major method to produce hydrogen from hydrocarbons is to obtain hydrogen from refined and decarbonized petroleum fraction that was subjected to thermal cracking: the fraction of gasses obtained can be reacted with steam to produce hydrogen in the same manner as the NGSR and water-gas shift reactions.[12,16]

1.1.2 Hydrogen production through Electrolysis

Water electrolysis is a process that consists of the transfer of electrons, from an external potential generator to water, to separate the water molecules into gaseous hydrogen and oxygen, according to the reaction:

$2H_2O\ (l) \rightarrow 2H_2(g) + O_2(g)$[17–19]

Water electrolysis is an endothermic and nonspontaneous chemical reaction and the required electrical energy for it to occur is given by the Gibbs' free energy change, ΔG:

$$\Delta G = \Delta H - T * \Delta S$$

At standard energy and pressure, $\Delta G° = 237.2\ kJ/mol$ with $\Delta H° = 285.8\ kJ/mol$ and $\Delta S° = 0.1631\ kJ/mol\ K$. [17,18,20]

For a reversible cell, the lowest required voltage to drive the electrolysis process is a function of ΔG and is:

$$V_{rev} = \frac{\Delta G}{z * F}$$

With z the number of electrons exchanged in the reaction and F Faraday's constant.

Because the electrolytic cell contains material that resists the current flow, the voltage applied to the cell has to be greater than the one applied at ideal conditions, and the corrective term, the overpotential, has to take into account all the sources of resistance in the cell. The potential supplied to the cell, V(i), needed to drive the water-splitting reaction is given by:

$$V(i) = V + \eta_a(i) + \eta_c(i) + IR_{el}(i) + \eta_{con}(i)$$

With I being the current, and R_{el} being the resistivity of the electrolyte and the terms, η_a and η_c, are the anodic and cathodic overpotentials respectively and are related to the current density; this potential is a function of the current density, i. [18,20–23]

In thermodynamical terms, the electrical energy requirements are represented by the variation of Gibbs' energy, ΔG, while thermal energy is represented by the product of temperature and entropy variation, $T\Delta S$. [17,18] As temperature increases, Gibbs' energy demands decrease, but thermal energy demands increase to maintain the temperature high. [17,19,20]

The overpotential, due to the Joule effect, has an impact on the operation temperature of the cell. Greater current densities can evolve gasses on the electrode surface significantly faster. While it is advantageous to use higher current densities to speed up the rate of production, some problems may arise: firstly, the concentration of electrolytes at the electrodes changes much faster, leading to higher overpotentials; secondly, the gasses that develop may bubble out of solution, preventing the solution from contacting the

electrodes, raising the resistance of the cell, and possibly cause mechanical stress on the electrode. For these reasons, some types of electrolyzers, such as the Alkaline Water Electrolyzer, operate at low current densities. [18,22,24]

Higher operating temperatures are typically beneficial, as the decrement of electrical energy to supply to the system is significant and can impact operating costs since thermal energy is significantly cheaper than electrical energy per kWh (figure 1.2), however they raise problems due to design and maintenance challenges, limiting the overall lifetime of the cell. [17,18,24,25]

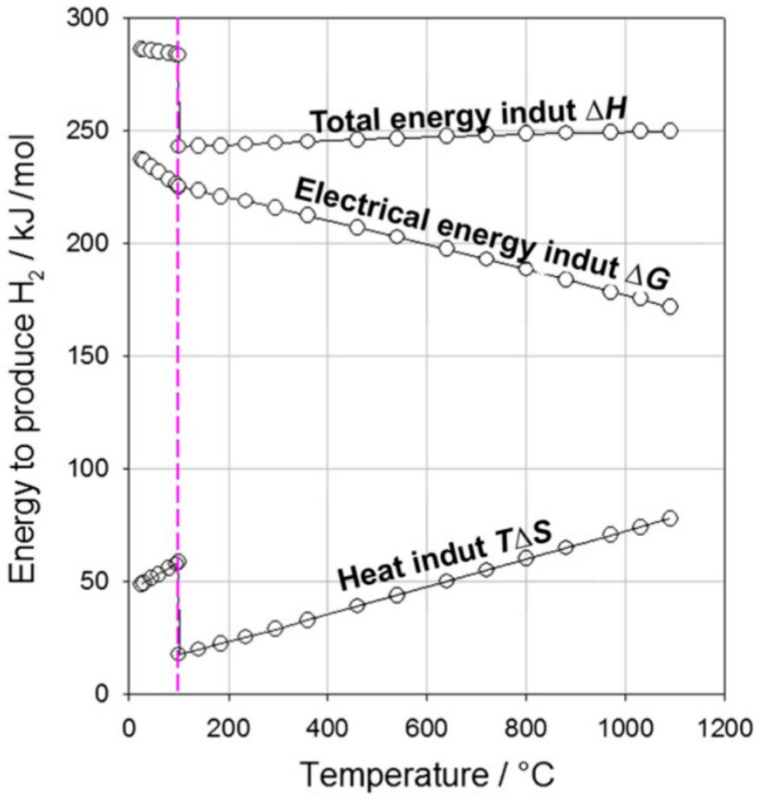

Figure 1.2 - Energy requirements to drive the water splitting reaction, based on the temperature of the system.[17]

Villagra and Millet have established a general way to estimate the possible cost of PEMWEs: the capital expense (CAPEX) for an electrolyzer system must take into account the cost of the electrolyzer stack as well as the costs of ancillary equipment, such as water purification, gas treatment units, and AC/DC converters; CAPEX can be calculated as:

$$CAPEX\ [€\ kg_{H_2}^{-1}] = \left(\frac{2F[C\ mol^{-1}]\ IC[€]}{T[s]\ S[cm^2]\ M_{H_2}[kg_{H_2} mol^{-1}]}\right)\frac{1}{j[A\ cm^{-2}]}$$

With F Faraday's constant, IC is the initial investment cost, T is the operational lifetime of the electrolyzer system, S is the area of the electrodes, M_{H2} is the mass of hydrogen produced, and j is the current density

applied to the cell. As it is shown the cost of cell, and in turn of the electrode, as well as the lifetime of the cell, impact the CAPEX, leading to the necessity of developing cheap and durable electrodes.

The operating expense (OPEX) includes maintenance costs and energy costs, of which the latter can fluctuate greatly each year, and is also a function of the operating current density and electricity costs (EC). The OPEX can be calculated as:

$$OPEX\left[€\ kg_{H_2}^{-1}\right] = \left(\frac{U_{cell}[V]\ F\left[C\ mol^{-1}\right]\ EC\left[€\ kWh^{-1}\right]}{3600\ J\left[kg_{H_2}\ kWh^{-1}\ mol^{-1}\right]}\right) EC[€\ kWh^{-1}] \quad [26]$$

CAPEX and OPEX show opposite trends with the current density and the costs of the cell materials should be minimized while trying to obtain the highest possible current density at the electrodes, in order to obtain the optimal balance between CAPEX and OPEX (figure 1.3). [17,26] As previoulsy mentioned, the durabilty and lifetime of an electrode affect the CAPEX, while the OPEX can be further lowered if the catalysts allow to maintain a desired current density while lowering the required cell voltage, and for these reasons the development of cheaper, more efficient electrodes and catalysts is crucial. [17]

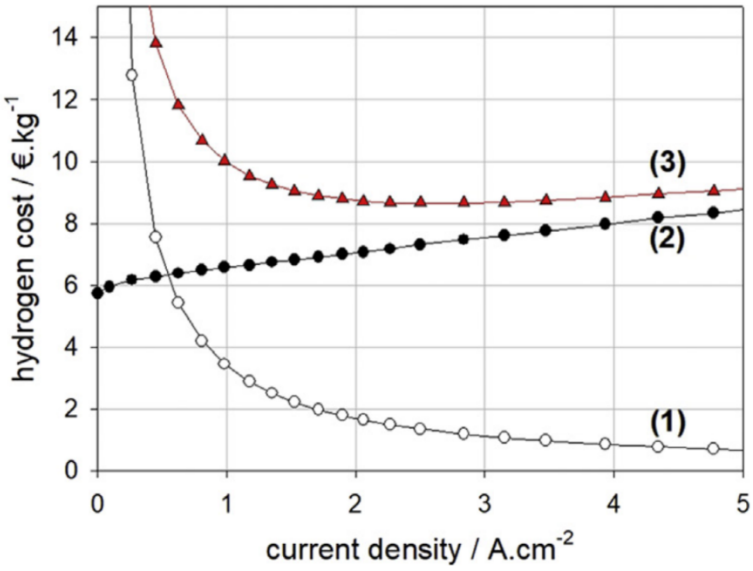

Figure 1.3 - Example of trendlines of (1) CAPEX, (2) OPEX, and (3) total costs for hydrogen production at different current densities. [17]

1.1.3 Electrochemical cells

The typical electrochemical cells used for water-splitting have two electrodes, that need to be resistant to corrosion, chemically inert, mechanically stable, and have good electric conductivity and catalytic properties. Usually, a diaphragm is also needed to separate the generated gasses and prevent the contact of the electrodes, thus preventing any short-circuiting of the cell. [17,18,21] The design for these cells is either monopolar or bipolar (figure 1.4): in monopolar designs, the electrodes are either positive or negative and electrodes with the same polarity are connected in parallel in the individual cells, while for bipolar cells the

electrodes are made of bipolar plates that serve on one side as anodes and cathodes on the other, with the individual cells connected in series electrically and geometrically. [17,18,20,21,25] To minimize the overpotentials given by the resistance of the solution, zero-gap designs have been proposed: the diaphragm is wetted by the electrolytic solution and sandwiched between the anode and the cathode. Both electrodes are perforated to allow the evacuation of the developed gasses from the back of the electrodes. The zero-gap design also helps in resolving the problem of the accumulation of gas on the surfaces of the electrodes. [18,21,25]

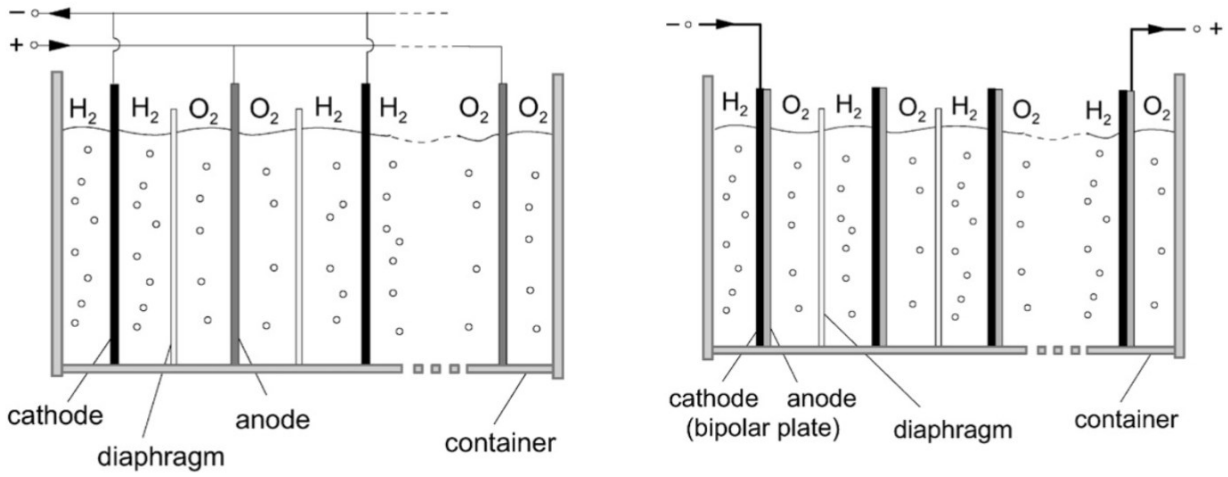

Figure 1.4 - Design of monopolar (left) and bipolar (right) electrolysis cells.[20]

At the industrial level there are two main types of electrolyzers, the Alkaline Water and Exchange Membrane Electrolyzers, and a third type, the Solid Oxide Electrolyzer, is in development and could be implemented at the industrial level in the near future. [7,17]

1.1.4 Types of electrochemical cells

Alkaline Water Electrolyzers (AWE) are the most mature technology, suitable for industrial-level applications, with a simple monopolar or bipolar design. These electrolyzers have low capital costs, because the electrode materials are cheap and easily sourced, and have low operating and maintenance costs. AWEs have fairly long lifetimes, reported up to 15 years, and large capacity units have been built. [7,17,18,21,25]

In an AWE cell, the two metal electrodes are submerged in a water solution containing an electrolyte, usually KOH between 25 to 30 wt%. In the typical AWE cell, the electrodes are steel grids coated with a layer of porous nickel, separated by a diaphragm. (figure 1.5) In earlier cells, the diaphragm was made of asbestos, but because of health concerns, nowadays different diaphragms are used. [7,17,21]

Although nickel is a very common electrode material, it provides high overpotentials for both hydrogen and oxygen evolution reactions, and other electrocatalytic materials, such as iron or molybdenum, are being researched for these electrodes. [21]

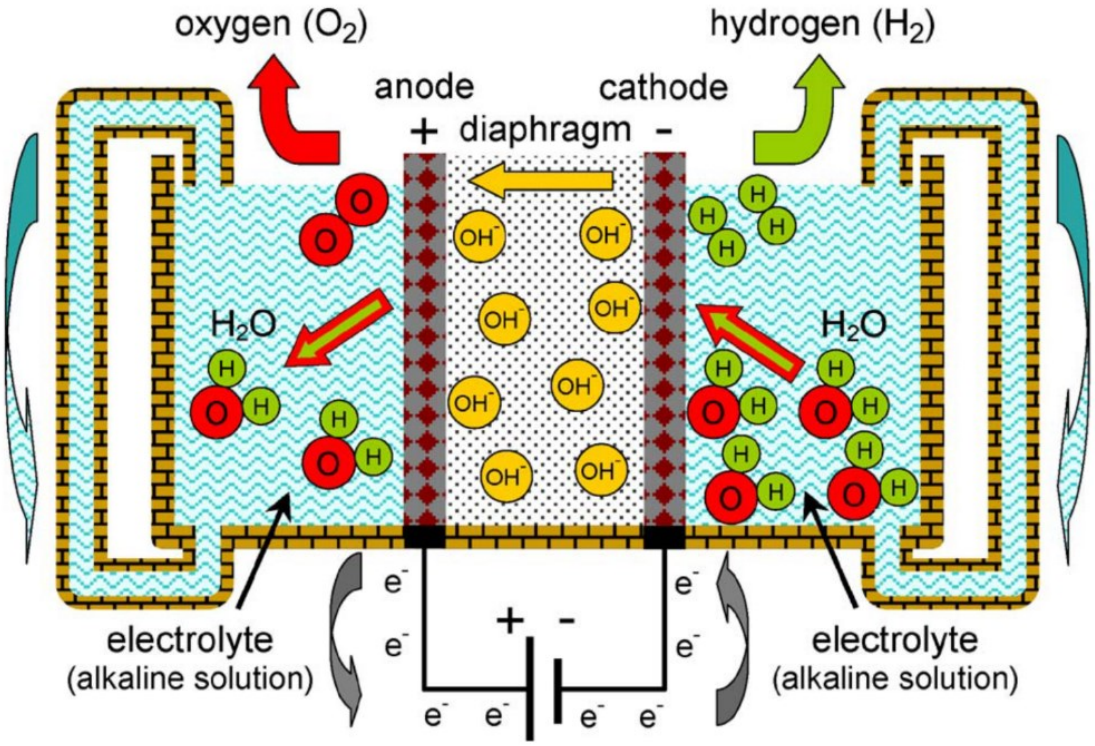

Figure 1.5 - Schematic design of an alkaline electrolysis cell [18]

In an alkaline solution, the overall reaction can be separated into two half-reactions:

$$Anode\ (+): 2OH^- \rightarrow H_2O(l) + \frac{1}{2}O_2(g) + 2e^-$$

$$Cathode\ (-): 2H_2O + 2e^- \rightarrow H_2(g) + 2OH^-$$ [7,17,21,24,25,27]

The cathodic reaction in the alkaline media usually proceeds with the initial "Volmer step", which is the adsorption of a proton on the surface of the metal:

$$Volmer\ step: H_2O + e^- + M \rightleftarrows M - H_{ad} + OH^-$$

This step is either followed by the "Heyrovsky step", a second adsorption of a proton on the metal surface, or by the "Tafel step", the combination of two adsorbed protons to form molecular hydrogen:

$$Heyrovsky\ step: H_2O + M - H_{ad} + e^- \rightleftarrows M + H_2 + OH^-$$

$$Tafel\ step: 2H_{ad} \rightleftarrows H_2$$ [28–30]

The AWE cell usually operates at temperatures between 60 to 80 °C and pressures between 1 to 30 bar, driving the reaction with current densities between 100 and 400 mA/cm^2. [17,18,25] These kinds of cells are able to produce hydrogen and oxygen with respective purity of 99.9% and 99.7% and often don't need further purification treatments. [7,17,18,21] Even though AWEs can operate at lower water purities than those required

for membrane electrolyzers, sufficiently pure water is required in order to maintain the efficiency of the cell and to prevent corrosion of the electrodes. [18,31]

Solid Oxide Electrolyzers (SOE) are still in development for industrial application, but present some promise for hydrogen production. Much of the information gained for this kind of electrolyzer have been obtained from Solid Oxide Fuel Cells operated in reverse mode; SOEs take advantage of the lower electrical energy demand at higher temperatures of the water electrolysis reaction. [7,17,18,32] This kind of electrolyzer has desirable characteristics for joint operation with nuclear reactors, that could supply both the electrical and thermal demands, but renewable sources such as geothermal energy have the potential as heat sources for steam electrolysis. [7,17,18]

The reaction to split water molecules follows the equation:

$$H_2O(g) + 2e^- \rightarrow H_2(g) + O^{2-}$$

And at the anode, the oxygen ions produced are oxidized:

$2O^{2-} + 2e^- \rightarrow O_2(g)$ [17,18]

These electrolyzers can operate at temperatures up to 1000 °C, utilizing a mixture of superheated steam and recycled hydrogen, which maintains reducing conditions at the cathode, and sometimes employing argon as a carrier gas. [17,32]

Exchange Membrane Electrolysers can be either Proton Exchange Membrane Water Electrolyzers (PEMWE) or Anion Exchange Membrane Water Electrolyzers (AEMWE). [31,33,34] Both of these types of cells are designed with a gas-tight membrane that separates the anode and the cathode in the zero-gap configuration, forming the Membrane Electrode Assembly (MEA). [17,18,31,33,34] Depending on the type of membrane, these electrolyzers operate either in acidic, as is the case for PEMWEs, or in alkaline conditions, in the case of AEMWEs (figure 1.6). [31,33,34]

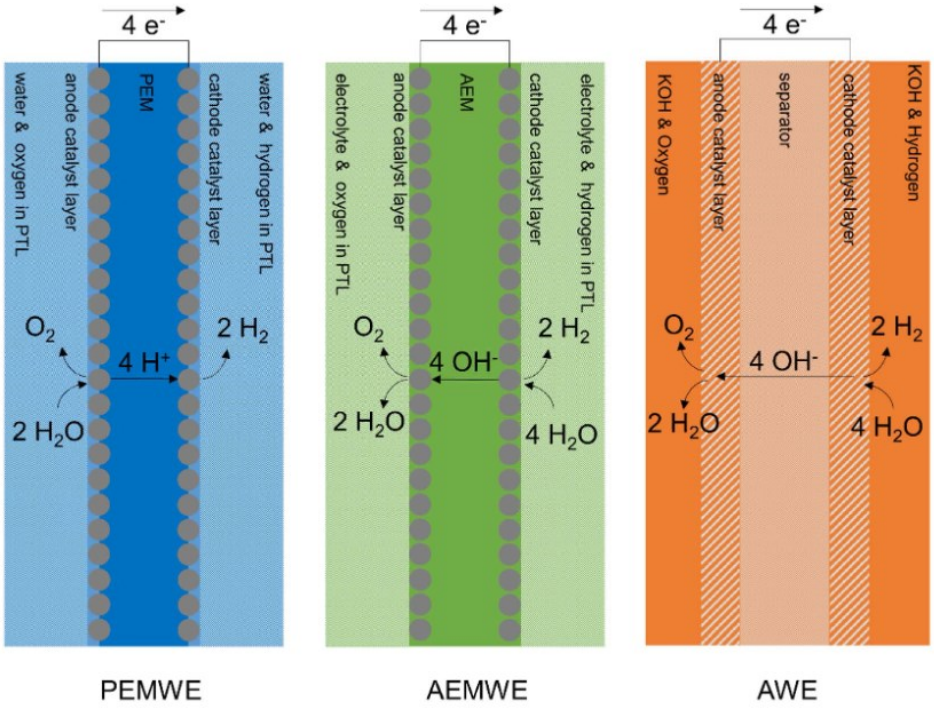

Figure 1.6 - Schematic comparison between PEMWEs, AEMWEs and AWEs

In PEMWEs the anode and cathode are pressed against a membrane of perfluorinated phosphonic acid copolymers (figure 1.7); one such membrane is Nafion® by DuPont, which is a copolymer of tetrafluoroethylene containing sulfonic groups. The anode is typically Iridium oxide, Iridium, and Ruthenium Oxides, or in some cases Platinum black, while the cathode is typically Platinum or Palladium. [7,17,18,26,31] For these electrolyzers, the reaction in acidic media can be separated into two half-reactions:

$$Anode\colon\ H_2O \rightarrow \frac{1}{2}O_2 + 2e^- + 2H^+$$

$$Cathode\colon\ H^+ + 2e^- \rightarrow H_2$$

In acidic conditions, the Volmer and Heyrovsky steps become:

$$Volmer\ step\colon H_3O^+ + e^- + M \rightleftarrows M - H_{ad} + H_2O$$

$$Heyrovsky\ step\colon H_3O^+ + M - H_{ad} + e^- \rightleftarrows M + H_2 + H_2O$$

While the Tafel step remains unchanged. [28–30] PEMWEs have high efficiencies, can produce hydrogen at 99.99% purity, and can operate at high current densities, sometimes of several A/cm^2. Typical operating conditions for PEMWEs are current densities in the 1-3 A/cm^2 and at temperatures around 80 °C; [17,18,26] they are usually fed water with electric conductivity below 1 µS/cm. [18,31] These electrolyzers respond well to fluctuating power sources and are therefore suitable for coupling with solar energy collectors. PEMWEs are already commercially available for low-scale hydrogen production and have been scaled up to have production capacities above 10 Nm^3 H_2/h, but they exhibit a number of problems: the main drawback of

PEMWEs is the high cost, since platinum group metals are needed, exacerbated by the shorter lifetime of the cell when compared to alkaline cells, typically of about 6 to 9 years; the acidic conditions limit the choice of catalysts to platinum group metals. To run the cell there is also the need for a high-purity water feed. [7,17,26,31,34] The low lifetime is due to membrane degradation, as the incomplete reduction of oxygen leads to the formation of small amounts of hydrogen peroxide, which leads to the gradual degradation of the polymer membrane. [18]

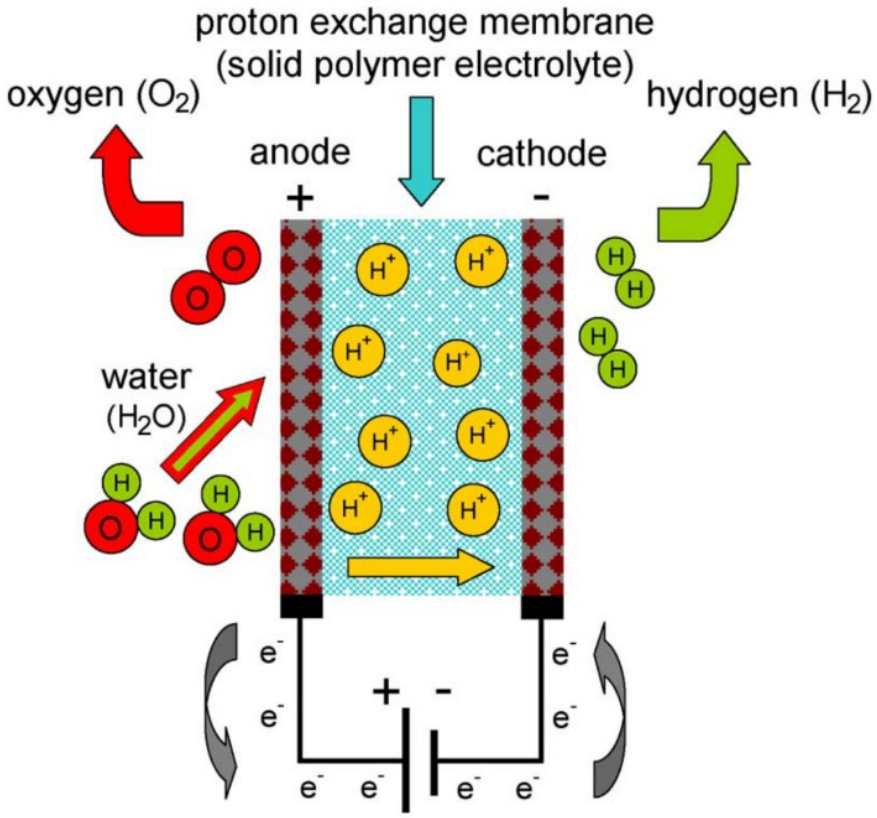

Figure 1.7 - Schematic view of a PEM water electrolysis cell. [18]

While PEMWEs are a semi-mature technology, AEMWEs are still in an early development stage.

The MEA for AEMWEs consists of a membrane made of a polymeric backbone on which cationic headgroups are attached. Since this kind of electrolyzer is still in the development stage, the materials to construct the electrodes vary and can be made of different metals such as Nickel, Iron, Cobalt, and Copper, but research has also focused on chalcogenides, sulfides, and phosphides of transition metals. [34–36] The electrodes for AEMWEs are typically based on a steel, carbon, or nickel substrate and a nickel-based catalyst, which may contain other non-precious elements such as cobalt, manganese, and iron; copper-based catalysts are also a possible alternative. [35,37] The membranes for the MEA are often made of imidazolium and benzimidazolium-based polymers and, alongside the electrodes, are still a subject of research, which focuses on creating membranes less susceptible to degradation. [31,33,34,38] Recently, polymers containing aromatic structures have

received growing attention due to their rigidity and thermal stability. [35] On the polymer backbone are attached ion exchange groups, such as $-NH_3^+$, $-RNH_2^+$, $-RN^+$, R_3P, and $-R_2S^+$. [37] Figure 1.8 shows an example of an AEMWE.

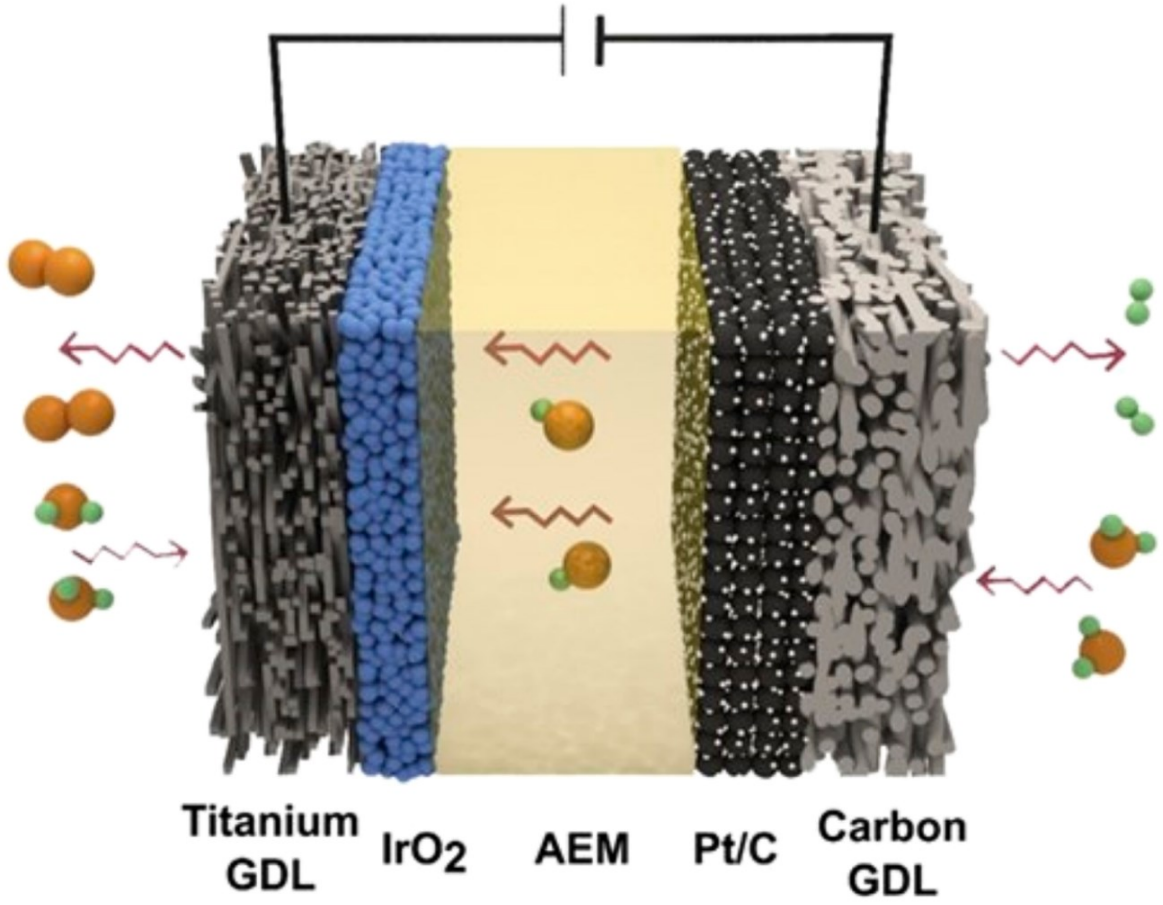

Figure 1.8 - Simplified representation of an AEMWE. For this cell, the anode is porous titanium on which IrO_2 is deposited (anode) and porous carbon on which is deposited Pt supported on carbon (cathode). [34]

The reaction that occurs in AEMWEs follows the same pathway as AWEs, and the electrolyzer solution is either a pure water feed or a dilute solution of KOH or K_2CO_3, with the main ionic species involved in the reaction being the hydroxide. [31,35,38] AEWWEs usually operate at around 60 to 80 °C, at potentials between 2.3 and 1.7 V, and at current densities between 1.7 and 2 A/cm^2, showing improved reaction kinetics and current densities at higher temperatures; [31,39,40] however, excessive temperatures can dry the membrane and degrade it. [35]

The main limitation of PEMWEs is the requirement of platinum-group metals in their construction, because of the high acidity of the membrane, which could corrode other transition metals; AEMWEs are a promising technology because they tend to share many of the desirable properties of PEMWEs, while not being limited by the need for rare and expensive materials. [31,33,34,38] AEMWEs need to mature further, to have application at the industrial scale. [34,38] One aspect of AEMWEs that needs to be developed is the electrodic material and

its catalytic loadings, and recently Transition Metal Sulfides (TMS) have been shown to have desirable characteristics for this purpose.

1.1.5 Transition Metals Sulfides

As previously mentioned chalcogenides and sulfides could be an alternative to platinum-group metals for the construction of electrodes for AEMWEs. Several studies in the literature mention nickel as the principal metal, both in its pure form, as a foam, or as sulfide or oxide. However, nickel is not the only promising material proposed for use as cathode in AEMWEs and, due to its well-known toxicity, its use should preferably be excluded in electrodes, both to avoid damage to the health of workers and to limit the possible presence of this metal in water. [34–37,41–43]

Iron sulfides are both possible candidates for the production of electrodes as well as possible dopant materials for other metals and metal sulfides. [36,44,45] For example, iron's affinity for nickel is well known, entering the lattice of the latter with ease, stabilizing it, and improving the overall catalytic performance. Similar effects on OER catalysis can be observed for cobalt-based electrodes. [34,45] Similarly, cobalt and cobalt sulfides exhibit favorable catalytic activity and can be used to improve the activity of MoS_2 and WS_2-based electrodes. [44,46] Improvements in catalysis were reported, for example, by Kong et al. as cobalt Selenide and cobalt disulfide display excellent catalytic activity, followed closely by nickel disulfide, nickel diselenide, $Co_{0.32}Ni_{0.68}S_2$, and $Fe_{0.43}Co_{0.57}S_2$. [45]

Molybdenum Disulfide has shown to be a promising catalyst as a cathode for HER, both as a pure material and when doped with other metals, MoS_2 is one of the most widely investigated materials in the TMS family because of its catalytic activity [44,47–50] and because of its low toxicity. [51]

1.2 Molybdenum Disulfide

1.2.1 Physical and chemical properties of Molybdenum Disulfide

Molybdenum Disulfide can be commonly found in nature as the mineral molybdenite, a dark lead-grey crystalline solid with a metallic luster. [52–54] The bulk crystal of molybdenum disulfide is made of stacked layers, much like graphite, with each layer made of Molybdenum (Mo^{4+}) atoms sandwiched between two layers of sulfur (S^{2-}) atoms. Each atom of Mo has strong covalent bonds with six sulfur atoms, which are 0.24 nm in length, resulting in planar sheets. The stacked layers of MoS_2 are only weakly bonded with each other through van der Waals interactions, with an interlayer spacing that is typically 0.62-0.65 nm, and can slide over each other easily and can be exfoliated similarly to graphite. [47–50,52,55–59]

Figure 1.9 - MoS2 crystal embedded in rock. [60]

In the bulk crystal, the disposition of the sheets and the atoms of MoS_2 can result in multiple polymorphs, with three main ones: the 2H, the 1T, and the 3R phases (figure 1.10). [47–49,55,56] These phases are defined by their unit cells, with the letters "H", "T", and "R", used to refer to the hexagonal, tetragonal, and rhombohedral unit cells respectively, and the enumeration, which refers to the number of layers per unit cell. [48,61]

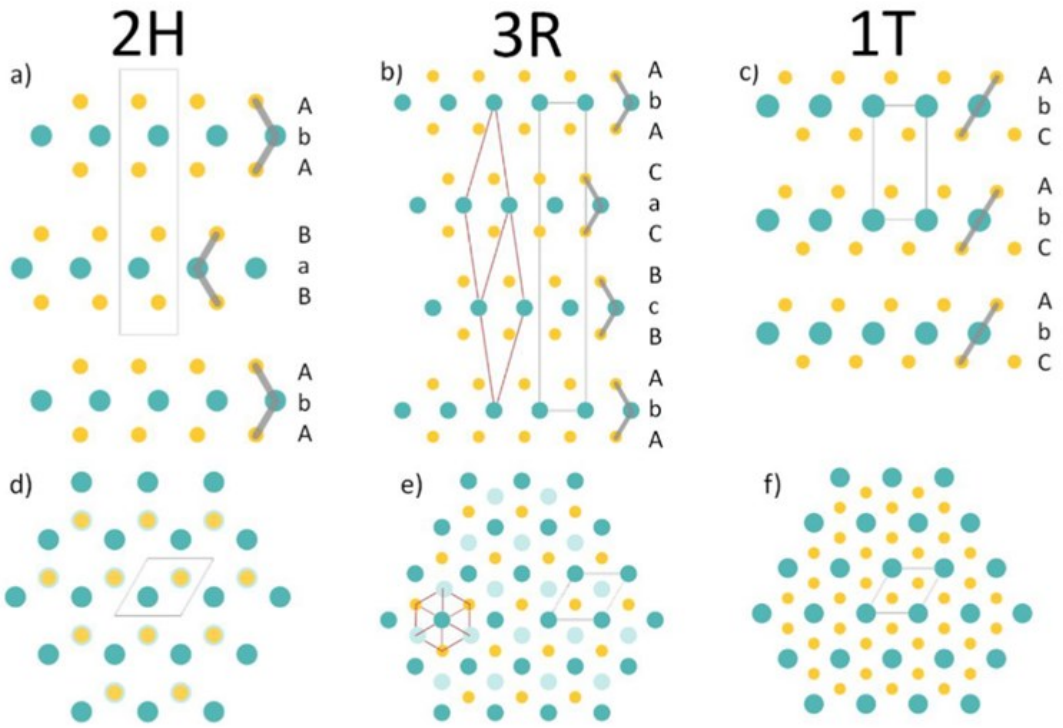

Figure 1.10 - Representation of the different 2H, 3R and 1T phases of MoS2.[62]

The 2H-MoS_2 phase has a hexagonal Bravais lattice structure and belongs to the $P6_3/mmc$ space group. The crystal lattice is described by hexagonal unit cells with cell parameters $a = b = 0.315\ nm$ and $c = 1.230\ nm$. [56,58,60,63–66]

In the bulk material, 2H-MoS_2 has alternating layers oriented in opposite directions with AbA-BaB layer stacking, where upper case letters represent sulfur atoms and lower-case letters represent molybdenum atoms. [48,49,62,67,68]

As with other bidimensional layered materials, MoS_2 presents an inert basal plane and exposed active edge sites, as shown in figure 1.11. The basal plane of 2H-MoS_2 does not contribute to catalysis but can be modified to resemble the active basal plane of the 1T-MoS_2 phase, through heteroatom doping and by inducing strain in the MoS_2 sheet. [44,69]

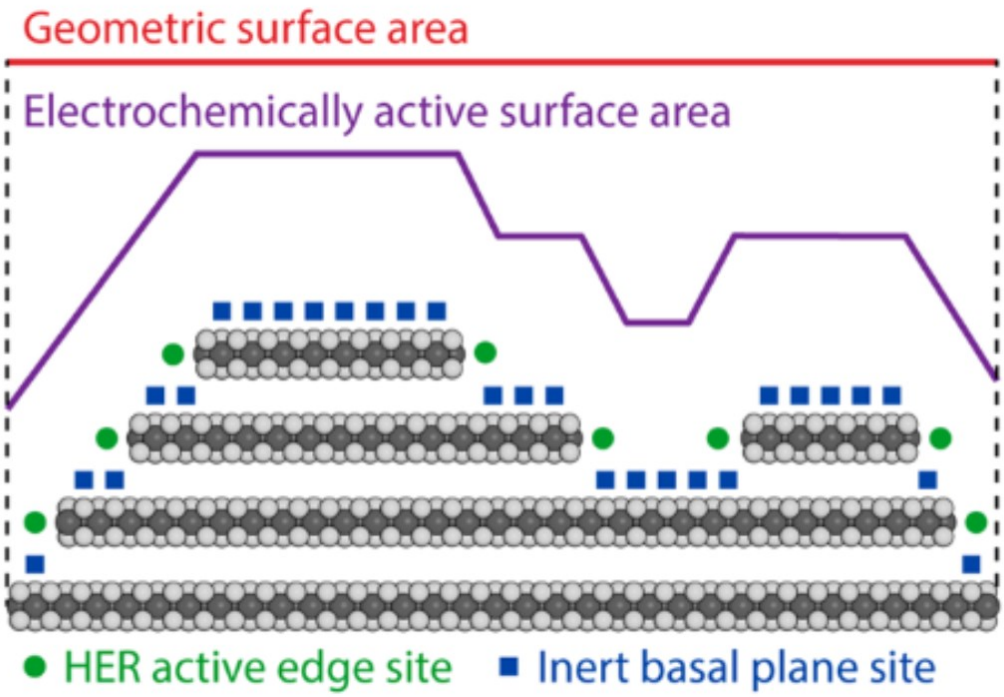

Figure 1.11 - Representation of basal plane and edge sites of MoS_2.

Bulk 2H-MoS_2 is the most stable and naturally MoS_2 crystallizes in this phase, while both the 1T and the 3R phases are metastable and convert to the 2H-MoS_2 phase over time or with annealing. [48,56,62,70] The 1T phase is a particular case, because it has metallic behavior, unlike the 2H and the 3R phase that are semiconductors. Also unlike the 2H-MoS_2 and 3R-MoS_2 phases, the 1T phase has octahedral coordination and belongs to the P-3m1 space group. [48,49,56,70] The 1T phase would be the more desirable one, since its basal plane, alongside the edge sites, is catalytically active given the affinity of its surface S sites for binding H species. [71] Surface engineering of layers of 2H-MoS2 focuses on recreating similar binding sites on the basal plane by inducing S vacancies that allow hydrogen binding on exposed Mo sites. [44]

The 3R phase of MoS_2 has trigonal prismatic coordination of Mo-S, and 3R-MoS_2 can be described by a hexagonal unit cell with cell parameters $a = b = 0.317\ nm$ and $c = 1.841\ nm$, with the 3R phase belongs to the R3m space group. When comparing 2H-MoS_2 and 3R-MoS_2 it can be observed that the sheets of 3R-

MoS_2 are both offset and oriented differently from those of the 2H phase: each layer of the 3R phase is oriented in the same direction, in an AbA-CaC-BcB stacking order (figure 1.12). [48,62,67,72]

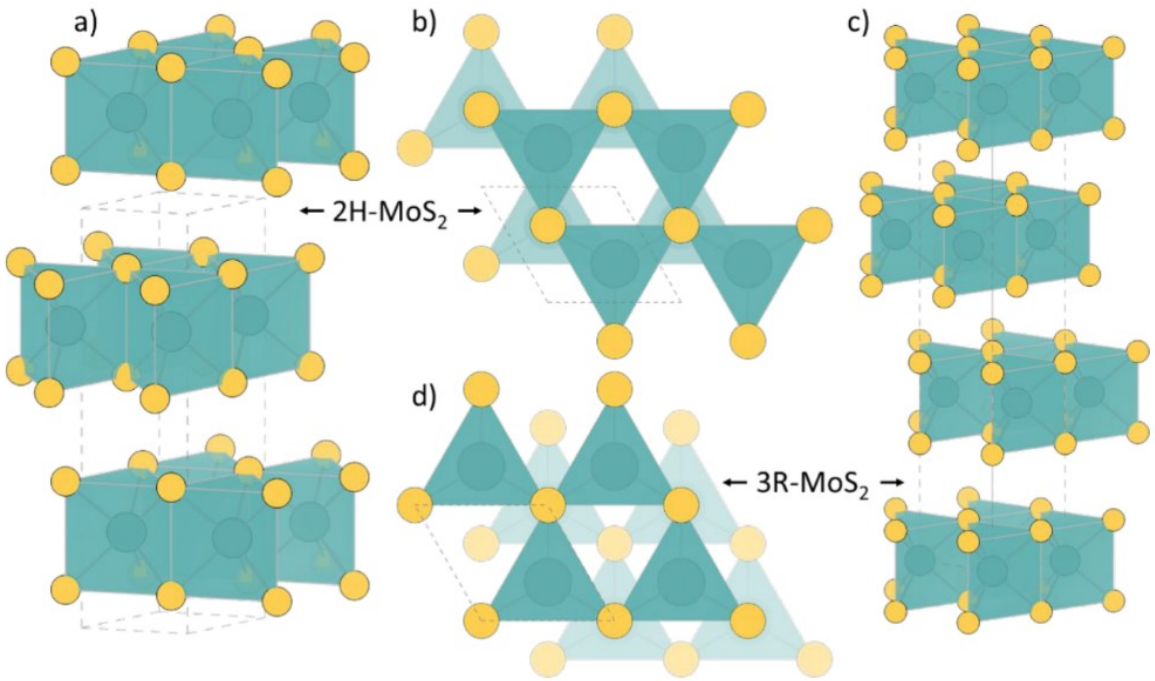

Figure 1.12 - Difference in layer stacking in the 2H and 3R phases. [62]

With exfoliation of MoS_2 up to the monolayer, the 2H phase, which is defined by unit cells that span multiple layers, exfoliation eventually leads to phase 1H, corresponding to a single-layer defined by a hexagonal unit cell. The 1H-MoS_2 is the most stable of the possible monolayer structures. [47–50,73]

When exfoliated to a single layer, the nature of the electronic band structure of MoS_2 changes from an indirect band gap of 1.2-1.3 eV to a direct band gap of 1.8-1.9 eV. The band structure and bandgap of 2H-MoS_2 are dependent on the number of layers present, with an increase of the bandgap width, from 1.2 eV to 1.7 eV, as the number of layers decreases. [48,64,74]

In bulk 2H-MoS_2, the layers per unit cell present inversion symmetry: by considering the Mo atom as the center of inversion, the sulfur atoms of the first monolayer will transform into the sulfur atoms of the second monolayer by inversion. [66] In the case of a monolayer, the sulfur atoms that should be found, corresponding to the second MoS_2 monolayer, are instead replaced by empty sites. The transition from bulk 2H-MoS_2 to 1H-MoS_2 removes the inversion symmetry and since the 2H phase has trigonal prismatic coordination, the outermost Mo^{4+} $4d^2$ orbitals are not degenerate and the symmetry-splitting results in the separation of the lower energy, d_{z^2} band, and the d_{xy}, d_{xz}, d_{zy} and $d_{x^2-y^2}$ sub-bands, which are unoccupied and have higher energy (figure 1.13). The electronic configuration of the d_{z^2} band, filled with two electrons, in the Mo^{4+} $4d^2$ orbitals results in the semiconducting behavior of 2H-MoS_2. [48–50,56,63,74,75] Conversely, because of the octahedral coordination, the symmetry-splitting of 1T-MoS_2 leads to orbitals having partially occupied

d_{xy}, d_{yz}, d_{xz} orbitals, at lower energy, and the $d_{x^2-y^2}, d_{z^2}$ orbitals with higher energy. Due to the partially filled orbitals of 1T-MoS_2, this phase shows metallic behavior. [48–50,56,63,74,75] The density of states of the Mo 4d and S 3p orbitals, in the bulk 1T-MoS_2 phase, confirms its metallic nature, since it distributes at the Fermi level. [48,74–77]

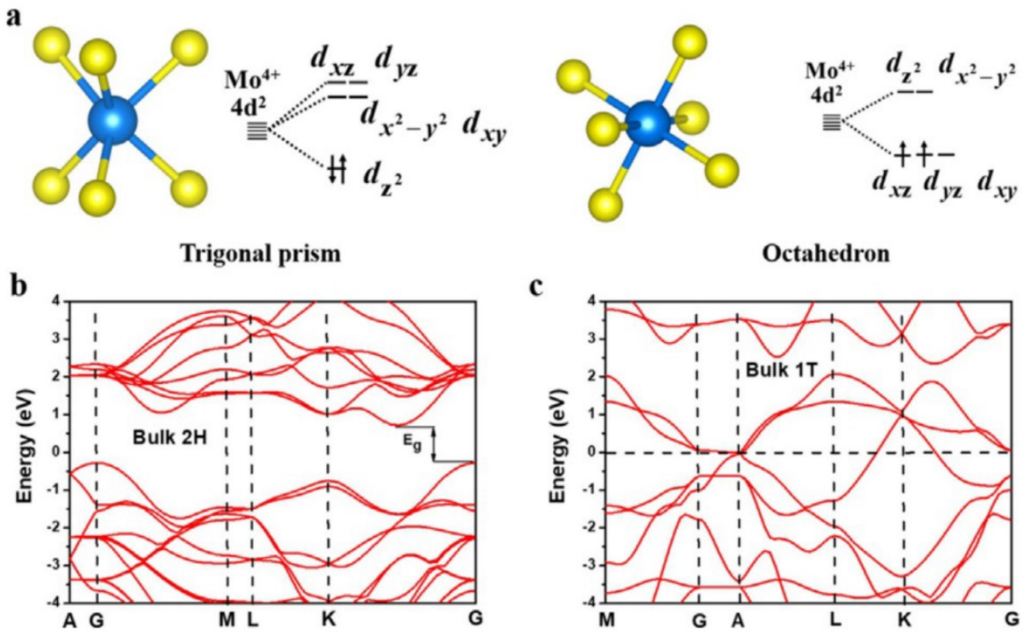

Figure 1.13 - (a) Structures of 2H-MoS_2 and 1T-MoS_2 and energy bandgaps of (b) trigonal prismatic 2H and (c) octahedral 1T structures of MoS_2.

Bulk 2H-MoS_2 has an indirect bandgap, with the conduction band located almost halfway between the Γ-K direction, and the valence band located at the G point; these bands consist mainly of Mo 4d and S 3p orbitals respectively. The valence band maximum of the multilayer 2H-MoS_2 is located at the Γ point of the Brillouin zone, while for the single layer 1H-MoS_2, the valence band maximum is located at the K point of the first Brillouin zone. [48,74–77]

1.2.2 State-of-the-art production of MoS_2 and new approaches

Industrially, molybdenum disulfide is obtained mainly from open pit mining of molybdenite or as a byproduct of copper processing. While abundant, the ore does not contain large amounts of MoS_2, which has to be concentrated via foam flotation. This production method results in 90-95% MoS2 concentrate, which can be further concentrated to 99% MoS_2 in secondary flotation processes. [52,78] Due to the purity level required in nanotechnology applications, however, alternate routes have been found.

One common top-down approach to the production of MoS_2 nano sheets involves its mechanical properties: since it can be exfoliated similarly to graphite, using sticky tape it is possible to exfoliate sheets of MoS_2 from the bulk material and deposit them on a substrate. This kind of approach cannot be scaled up, however.

Chemical exfoliation instead exploits the intercalation of lithium ions in between the MoS_2 sheets, for example using with n-butyllithium, and this kind of approach is being investigated as a possible path for large-scale MoS_2 sheets production. [50,79,80]

Typical bottom-up approaches involve the use of molybdenum coordination compounds as precursors for the synthesis, and two common synthesis paths are the production via hydrothermal methods, such as the reaction between ammonium molybdate ($(NH_4)_6Mo_7O_{24}$) and thiourea (H_2NCSNH_2), [81–83] or through Chemical Vapor Deposition avenue for the synthesis of the MoS_2 films or crystallite. [83–86] More recently, Physical Vapor Deposition (PVD) has also been investigated as an alternative path for synthesis, often using H_2S as the sulfurizing agent. [57,83,87,88] Due to the toxicity of the latter, however, it is of particular interest to find alternative synthesis methods.

The deposition of MoS_2 thin films, i.e. layer of controlled thickness directly on a support, is a topic that received much attention in the past, giving the promising electronic properties of this 2D material, which has been proposed as a novel platform for advanced (bendable) microelectronics. [89] In addition to the previously methods based on PVD, chemical vapor deposition has been widely employed to produce large mono or few layer flakes of MoS_2 of a variety of supports (silicon wafers, metal foils, glasses etc.). Sometimes, CVD methods employ also multistep strategies consisting in the deposition of MoO_x thin films followed by sulphidization.

Regarding the growth of MoS_2 on Au (111) through surface science methods, it is worth mentioning the works by P. Hoffmann's group, among the first to propose a method for the growth of epitaxial MoS_2 monolayers by evaporating Mo metal and dosing H_2S. In a series of works, based on low energy electron diffraction and atomically resolved STM it was shown that MoS_2 forms a moiré superstructure interpreted either as a simple (9x9) of MoS_2 on a (10x10) super cell of Au (111) or with a slight rotational angle (about 6°). Angle resolved photoemission experiments demonstrated that the band structure of MoS_2/Au (111) is very similar to that of self-standing films, only around some notable point of the Brillouin zone (i.e. gamma) some difference can be observed such as the removal of spin degeneracy, because of a small interaction between the S p_z and Mo d_{z^2} orbital with the metal states. [90]

1.3 Scope of this thesis

The scope of this thesis is the development of 2D films of transition metal sulfides, as a model surface for future fundamental investigations and development of new nanomaterials. In particular, this work will focus on the development of a synthetic procedure for the deposition of a 2D molybdenum disulfide film on an Au (111) single crystal substrate in ultra-high vacuum, through Physical Vapor Deposition; the metals will be deposited using Electron Beam evaporators, while the sulfurizing agent will be elemental sulfur sublimated in ultra-high vacuum.

The aim of the first part of this work is to produce a pure, clean 2D surface of MoS_2, while the second part will focus on the inclusion of iron atoms inside the molybdenum disulfide mesh, in order to observe how the structure is modified in the presence of doping atoms and how the latter can arrange within the lattice. The introduction of iron is quite interesting because it is a cheap and largely abundant transition metal with the potential of modifying the electronic and chemical properties of MoS_2, possibly boosting the catalytic properties. Indeed, several papers in the literature point to the improvement in the hydrogen evolution reaction of Fe doped MoS_2 compared to pristine materials, however it is still unclear where exactly the dopant is located, and what is the reason for the better performance. [91] The films produced in the deposition will be characterized using X-ray Photoelectron Spectroscopy, Low Energy Electron Diffraction and Scanning Tunneling Microscopy, to obtain information not only on the chemical composition and atomic structure of the samples, but also the morphology at the nanoscale of the prepared films. In particular, it will be evaluated whether the iron atoms can be inserted atomically as substitutional or interstitial dopants into the MoS_2 lattice forming so called single atom catalysts or rather the iron phase remained separated forming a metallic or sulphidized additional phase. [92]

Bibliography for chapter 1:

1. Armor, J. N. A history of industrial catalysis. *Catal. Today* **163**, 3–9 (2011).

2. Ritchie, H., Roser, M. & Rosado, P. CO_2 and Greenhouse Gas Emissions. *Our World Data* (2020).

3. US EPA, O. Global Greenhouse Gas Emissions Data. https://www.epa.gov/ghgemissions/global-greenhouse-gas-emissions-data (2016).

4. Ritchie, H. & Roser, M. Sector by sector: where do global greenhouse gas emissions come from? *Our World Data* (2023).

5. Mazloomi, K. & Gomes, C. Hydrogen as an energy carrier: Prospects and challenges. *Renew. Sustain. Energy Rev.* **16**, 3024–3033 (2012).

6. Häussinger, P., Lohmüller, R. & Watson, A. M. Hydrogen, 1. Properties and Occurence. in *Ullmann's Encyclopedia of Industrial Chemistry* (ed. Wiley-VCH) (Wiley, 2011). doi:10.1002/14356007.a13_297.pub2.

7. Acar, C. & Dincer, I. 3.1 Hydrogen Production. in *Comprehensive Energy Systems* 1–40 (Elsevier, 2018). doi:10.1016/B978-0-12-809597-3.00304-7.

8. Technology, S. U. of. The colors of hydrogen explained. https://techxplore.com/news/2022-05-hydrogen.html.

9. Das, D. & Veziroglu, T. N. Advances in biological hydrogen production processes. *Int. J. Hydrog. Energy* **33**, 6046–6057 (2008).

10. Hydrogen Production: Natural Gas Reforming. *Energy.gov* https://www.energy.gov/eere/fuelcells/hydrogen-production-natural-gas-reforming.

11. *Hydrogen and Syngas Production and Purification Technologies*. (Wiley ; AIChE, Hoboken, N.J. : [New York], 2010).

12. *Handbook of Petroleum Refining Processes, Third Edition*. (McGraw-Hill Education, 2004).

13. Franchi, G., Capocelli, M., De Falco, M., Piemonte, V. & Barba, D. Hydrogen Production via Steam Reforming: A Critical Analysis of MR and RMM Technologies. *Membranes* **10**, 10 (2020).

14. Midilli, A., Kucuk, H., Topal, M. E., Akbulut, U. & Dincer, I. A comprehensive review on hydrogen production from coal gasification: Challenges and Opportunities. *Int. J. Hydrog. Energy* **46**, 25385–25412 (2021).

15. Lin, S., Harada, M., Suzuki, Y. & Hatano, H. Hydrogen production from coal by separating carbon dioxide during gasification. *Fuel* **81**, 2079–2085 (2002).

16. Halloran, J. W. Extraction of hydrogen from fossil fuels with production of solid carbon materials. *Int. J. Hydrog. Energy* **33**, 2218–2224 (2008).

17. Millet, P. & Grigoriev, S. Water Electrolysis Technologies. in *Renewable Hydrogen Technologies* 19–41 (Elsevier, 2013). doi:10.1016/B978-0-444-56352-1.00002-7.

18. Ursua, A., Gandia, L. M. & Sanchis, P. Hydrogen Production From Water Electrolysis: Current Status and Future Trends. *Proc. IEEE* **100**, 410–426 (2012).

19. Hu, C., Zhang, L. & Gong, J. Recent progress made in the mechanism comprehension and design of electrocatalysts for alkaline water splitting. *Energy Environ. Sci.* **12**, 2620–2645 (2019).

20. Abdin, Z., Webb, C. J. & Gray, E. MacA. Modelling and simulation of a proton exchange membrane (PEM) electrolyser cell. *Int. J. Hydrog. Energy* **40**, 13243–13257 (2015).

21. Brauns, J. & Turek, T. Alkaline Water Electrolysis Powered by Renewable Energy: A Review. *Processes* **8**, 248 (2020).

22. Amores, E., Rodríguez, J. & Carreras, C. Influence of operation parameters in the modeling of alkaline water electrolyzers for hydrogen production. *Int. J. Hydrog. Energy* **39**, 13063–13078 (2014).

23. Kai, J. *et al.* Effect of Temperature on the Performance of Polymer Electrolyte Membrane Water Electrolysis: Numerical Analysis of Electrolysis Voltage Considering Gas/Liquid Two-Phase Flow. *J. Electrochem. Soc.* **166**, F246 (2019).

24. Hourng, L. W., Tsai, T. T. & Lin, M. Y. The analysis of energy efficiency in water electrolysis under high temperature and high pressure. *IOP Conf. Ser. Earth Environ. Sci.* **93**, 012035 (2017).

25. Ulleberg, Ø. Modeling of advanced alkaline electrolyzers: a system simulation approach. *Int. J. Hydrog. Energy* **28**, 21–33 (2003).

26. Villagra, A. & Millet, P. An analysis of PEM water electrolysis cells operating at elevated current densities. *Int. J. Hydrog. Energy* **44**, 9708–9717 (2019).

27. Appleby, A., Crepy, G. & Jacquelin, J. High efficiency water electrolysis in alkaline solution. *Int. J. Hydrog. Energy* **3**, 21–37 (1978).

28. Bao, F. *et al.* Understanding the Hydrogen Evolution Reaction Kinetics of Electrodeposited Nickel-Molybdenum in Acidic, Near-Neutral, and Alkaline Conditions. *ChemElectroChem* **8**, 195–208 (2021).

29. Strmcnik, D., Lopes, P. P., Genorio, B., Stamenkovic, V. R. & Markovic, N. M. Design principles for hydrogen evolution reaction catalyst materials. *Nano Energy* **29**, 29–36 (2016).

30. Sheng, W., Gasteiger, H. A. & Shao-Horn, Y. Hydrogen Oxidation and Evolution Reaction Kinetics on Platinum: Acid vs Alkaline Electrolytes. *J. Electrochem. Soc.* **157**, B1529 (2010).

31. Becker, H. *et al.* Impact of impurities on water electrolysis: a review. *Sustain. Energy Fuels* **7**, 1565–1603 (2023).

32. Shin, Y., Park, W., Chang, J. & Park, J. Evaluation of the high temperature electrolysis of steam to produce hydrogen. *Int. J. Hydrog. Energy* **32**, 1486–1491 (2007).

33. Khataee, A., Shirole, A., Jannasch, P., Krüger, A. & Cornell, A. Anion exchange membrane water electrolysis using Aemion™ membranes and nickel electrodes. *J. Mater. Chem. A* **10**, 16061–16070 (2022).

34. Du, N. *et al.* Anion-Exchange Membrane Water Electrolyzers. *Chem. Rev.* **122**, 11830–11895 (2022).

35. Ng, W. K., Wong, W. Y., Rosli, N. A. H. & Loh, K. S. Commercial Anion Exchange Membranes (AEMs) for Fuel Cell and Water Electrolyzer Applications: Performance, Durability, and Materials Advancement. *Separations* **10**, 424 (2023).

36. Zeng, K. & Zhang, D. Recent progress in alkaline water electrolysis for hydrogen production and applications. *Prog. Energy Combust. Sci.* **36**, 307–326 (2010).

37. Vincent, I. & Bessarabov, D. Low cost hydrogen production by anion exchange membrane electrolysis: A review. *Renew. Sustain. Energy Rev.* **81**, 1690–1704 (2018).

38. Andrew Miller, H. *et al.* Green hydrogen from anion exchange membrane water electrolysis: a review of recent developments in critical materials and operating conditions. *Sustain. Energy Fuels* **4**, 2114–2133 (2020).

39. Kraglund, M. R. *et al.* Ion-solvating membranes as a new approach towards high rate alkaline electrolyzers. *Energy Environ. Sci.* **12**, 3313–3318 (2019).

40. Gatto, I. *et al.* Optimal operating conditions evaluation of an anion-exchange-membrane electrolyzer based on FUMASEP® FAA3-50 membrane. *Int. J. Hydrog. Energy* **48**, 11914–11921 (2023).

41. Coman, V., Robotin, B. & Ilea, P. Nickel recovery/removal from industrial wastes: A review. *Resour. Conserv. Recycl.* **73**, 229–238 (2013).

42. Gates, A., Jakubowski, J. A. & Regina, A. C. Nickel Toxicology. in *StatPearls* (StatPearls Publishing, Treasure Island (FL), 2024).

43. Genchi, G., Carocci, A., Lauria, G., Sinicropi, M. S. & Catalano, A. Nickel: Human Health and Environmental Toxicology. *Int. J. Environ. Res. Public. Health* **17**, 679 (2020).

44. Wang, M., Zhang, L., He, Y. & Zhu, H. Recent advances in transition-metal-sulfide-based bifunctional electrocatalysts for overall water splitting. *J. Mater. Chem. A* **9**, 5320–5363 (2021).

45. Kong, D., Cha, J. J., Wang, H., Lee, H. R. & Cui, Y. First-row transition metal dichalcogenide catalysts for hydrogen evolution reaction. *Energy Environ. Sci.* **6**, 3553–3558 (2013).

46. Bonde, J., Moses, P. G., Jaramillo, T. F., Nørskov, J. K. & Chorkendorff, I. Hydrogen evolution on nano-particulate transition metal sulfides. *Faraday Discuss.* **140**, 219–231 (2008).

47. Li, Z., Meng, X. & Zhang, Z. Recent development on MoS2-based photocatalysis: A review. *J. Photochem. Photobiol. C Photochem. Rev.* **35**, 39–55 (2018).

48. Zhao, W. *et al.* Metastable MoS_2 : Crystal Structure, Electronic Band Structure, Synthetic Approach and Intriguing Physical Properties. *Chem. - Eur. J.* **24**, 15942–15954 (2018).

49. Wu, F. *et al.* Formation of Coherent 1H–1T Heterostructures in Single-Layer MoS2 on Au(111). *ACS Nano* **14**, 16939–16950 (2020).

50. He, Z. & Que, W. Molybdenum disulfide nanomaterials: Structures, properties, synthesis and recent progress on hydrogen evolution reaction. *Appl. Mater. Today* **3**, 23–56 (2016).

51. Chen, W. *et al.* Direct Assessment of the Toxicity of Molybdenum Disulfide Atomically Thin Film and Microparticles via Cytotoxicity and Patch Testing. *Small* **14**, 1702600 (2018).

52. Sebenik, R. F. *et al.* Molybdenum and Molybdenum Compounds. in *Ullmann's Encyclopedia of Industrial Chemistry* (ed. Wiley-VCH Verlag GmbH & Co. KGaA) a16_655 (Wiley-VCH Verlag GmbH & Co. KGaA, Weinheim, Germany, 2000). doi:10.1002/14356007.a16_655.

53. MAT, M. Molybdenite Mineral | Physical - Optical Properties, Occurrence, Uses. *Geology Science* https://geologyscience.com/minerals/molybdenite/ (2018).

54. Molybdenite. https://www.mindat.org/min-2746.html.

55. Sarma, S. & Ray, S. C. Trigonal (1T) and hexagonal (2H) mixed phases MoS2 thin films. *Appl. Surf. Sci.* **474**, 227–231 (2019).

56. Krishnan, U., Kaur, M., Singh, K., Kumar, M. & Kumar, A. A synoptic review of MoS2: Synthesis to applications. *Superlattices Microstruct.* **128**, 274–297 (2019).

57. Bana, H. *et al.* Epitaxial growth of single-orientation high-quality MoS2 monolayers. *2D Mater.* **5**, 035012 (2018).

58. Sun, J. *et al.* Synthesis Methods of Two-Dimensional MoS2: A Brief Review. *Crystals* **7**, 198 (2017).

59. Li, X. *et al.* One-step hydrothermal synthesis of high-percentage 1T-phase MoS2 quantum dots for remarkably enhanced visible-light-driven photocatalytic H2 evolution. *Appl. Catal. B Environ.* **243**, 76–85 (2019).

60. Molybdenite-2H. https://www.mindat.org/min-31721.html.

61. Jayabal, S., Wu, J., Chen, J., Geng, D. & Meng, X. Metallic 1T-MoS2 nanosheets and their composite materials: Preparation, properties and emerging applications. *Mater. Today Energy* **10**, 264–279 (2018).

62. Strachan, J., Masters, A. F. & Maschmeyer, T. 3R-MoS_2 in Review: History, Status, and Outlook. *ACS Appl. Energy Mater.* **4**, 7405–7418 (2021).

63. Kan, M. *et al.* Structures and Phase Transition of a MoS_2 Monolayer. *J. Phys. Chem. C* **118**, 1515–1522 (2014).

64. Jones, L. A. H. *et al.* Band Alignments, Electronic Structure, and Core-Level Spectra of Bulk Molybdenum Dichalcogenides (MoS_2, $MoSe_2$, and $MoTe_2$). *J. Phys. Chem. C* **126**, 21022–21033 (2022).

65. Potoczek, M., Przybylski, K. & Rekas, M. Defect structure and electrical properties of molybdenum disulphide. *J. Phys. Chem. Solids* **67**, 2528–2535 (2006).

66. Kadantsev, E. S. & Hawrylak, P. Electronic structure of a single MoS2 monolayer. *Solid State Commun.* **152**, 909–913 (2012).

67. Shi, J. *et al.* 3R MoS_2 with Broken Inversion Symmetry: A Promising Ultrathin Nonlinear Optical Device. *Adv. Mater.* **29**, 1701486 (2017).

68. Jiao, Y. *et al.* Metallic MoS2 for High Performance Energy Storage and Energy Conversion. *Small* **14**, 1800640 (2018).

69. Benck, J. D., Hellstern, T. R., Kibsgaard, J., Chakthranont, P. & Jaramillo, T. F. Catalyzing the Hydrogen Evolution Reaction (HER) with Molybdenum Sulfide Nanomaterials. *ACS Catal.* **4**, 3957–3971 (2014).

70. Wypych, F. & Schöllhorn, R. 1T-MoS_2, a new metallic modification of molybdenum disulfide. *J Chem Soc Chem Commun* 1386–1388 (1992) doi:10.1039/C39920001386.

71. Tang, Q. & Jiang, D. Mechanism of Hydrogen Evolution Reaction on 1T-MoS2 from First Principles. *ACS Catal.* **6**, 4953–4961 (2016).

72. Molybdenite-3R. https://www.mindat.org/min-2745.html.

73. Calandra, M. Chemically exfoliated single-layer MoS_2: Stability, lattice dynamics, and catalytic adsorption from first principles. *Phys. Rev. B* **88**, 245428 (2013).

74. Jin, W. *et al.* Direct Measurement of the Thickness-Dependent Electronic Band Structure of ${\mathrm{MoS}}_{2}$ Using Angle-Resolved Photoemission Spectroscopy. *Phys. Rev. Lett.* **111**, 106801 (2013).

75. Mak, K. F., Lee, C., Hone, J., Shan, J. & Heinz, T. F. Atomically Thin MoS_2: A New Direct-Gap Semiconductor. *Phys. Rev. Lett.* **105**, 136805 (2010).

76. Coehoorn, R. *et al.* Electronic structure of ${\mathrm{MoSe}}_{2}$, ${\mathrm{MoS}}_{2}$, and ${\mathrm{WSe}}_{2}$. I. Band-structure calculations and photoelectron spectroscopy. *Phys. Rev. B* **35**, 6195–6202 (1987).

77. Mattheiss, L. F. Band Structures of Transition-Metal-Dichalcogenide Layer Compounds. *Phys. Rev. B* **8**, 3719–3740 (1973).

78. Benavente, E., Santa Ana, M. A., Mendizábal, F. & González, G. Intercalation chemistry of molybdenum disulfide. *Coord. Chem. Rev.* **224**, 87–109 (2002).

79. Quinn, M. D. J., Ho, N. H. & Notley, S. M. Aqueous Dispersions of Exfoliated Molybdenum Disulfide for Use in Visible-Light Photocatalysis. *ACS Appl. Mater. Interfaces* **5**, 12751–12756 (2013).

80. Saliba, M., Pierre Atanas, J., Maria Howayek, T. & Habchi, R. Molybdenum disulfide, exfoliation methods and applications to photocatalysis: a review. *Nanoscale Adv.* **5**, 6787–6803 (2023).

81. Bonneau, P. R., Wiley, J. B., Kaner, R. B. & Mansuktto, M. F. Metathetical Precursor Route to Molybdenum Disulfide. in *Inorganic Syntheses* 33–37 (John Wiley & Sons, Ltd, 1995). doi:10.1002/9780470132616.ch8.

82. Karim, S. S. *et al.* A contemplating review on different synthesis methods of 2D-Molybdenum disulfide (MoS2) nanosheets. *Fuel* **351**, 128923 (2023).

83. Gupta, D., Chauhan, V. & Kumar, R. A comprehensive review on synthesis and applications of molybdenum disulfide (MoS2) material: Past and recent developments. *Inorg. Chem. Commun.* **121**, 108200 (2020).

84. Ahn, C. *et al.* Low-Temperature Synthesis of Large-Scale Molybdenum Disulfide Thin Films Directly on a Plastic Substrate Using Plasma-Enhanced Chemical Vapor Deposition. *Adv. Mater.* **27**, 5223–5229 (2015).

85. Li, J. *et al.* Single-Crystal MoS2 Monolayer Wafer Grown on Au (111) Film Substrates. *Small* **17**, 2100743 (2021).

86. Bilgin, I. *et al.* Chemical Vapor Deposition Synthesized Atomically Thin Molybdenum Disulfide with Optoelectronic-Grade Crystalline Quality. *ACS Nano* **9**, 8822–8832 (2015).

87. Grønborg, S. S. *et al.* Synthesis of Epitaxial Single-Layer MoS2 on Au(111). *Langmuir* **31**, 9700–9706 (2015).

88. Lim, Y. R. *et al.* Roll-to-Roll Production of Layer-Controlled Molybdenum Disulfide: A Platform for 2D Semiconductor-Based Industrial Applications. *Adv. Mater.* **30**, 1705270 (2018).

89. Volmer, F. *et al.* Twist angle dependent interlayer transfer of valley polarization from excitons to free charge carriers in WSe2/MoSe2 heterobilayers. *Npj 2D Mater. Appl.* **7**, 1–10 (2023).

90. Bruix, A. *et al.* Single-layer ${\text{MoS}}_{2}$ on Au(111): Band gap renormalization and substrate interaction. *Phys. Rev. B* **93**, 165422 (2016).

91. Qi, K. *et al.* Single-atom cobalt array bound to distorted 1T MoS2 with ensemble effect for hydrogen evolution catalysis. *Nat. Commun.* **10**, 5231 (2019).

92. Zhang, Y. Heterogeneous catalysis: Single atoms on a roll. *Nat. Rev. Chem.* **2**, 1–1 (2018).

Chapter 2 – Materials and Instrumentation

2.1 Materials

2.1.1 Gold substrate

The substrate chosen upon which to grow the layer of MoS_2 is a monocrystal of Au (111).

While the unreconstructed surface of Au (111) follows the fcc structure and presents hexagonal lattices, the reconstructed surface exhibits a corrugated structure of paired rows (figure 1). The reconstructed of the Au (111) surface, is subjected to a 4 % compression along one of the $[1\bar{1}0]$directions, yielding a $(22 \times \sqrt{3})$ unit cell. This contraction leads to 23 surface atoms of gold to be matched over 22 bulk sites of the unit cell, alternating fcc and hcp stacking regions, parallel to the $[11\bar{2}]$ direction. The corrugation of the surface, shown as brighter lines in figure 2.1, forms near the separation of the fcc and hcp areas. [1,2]

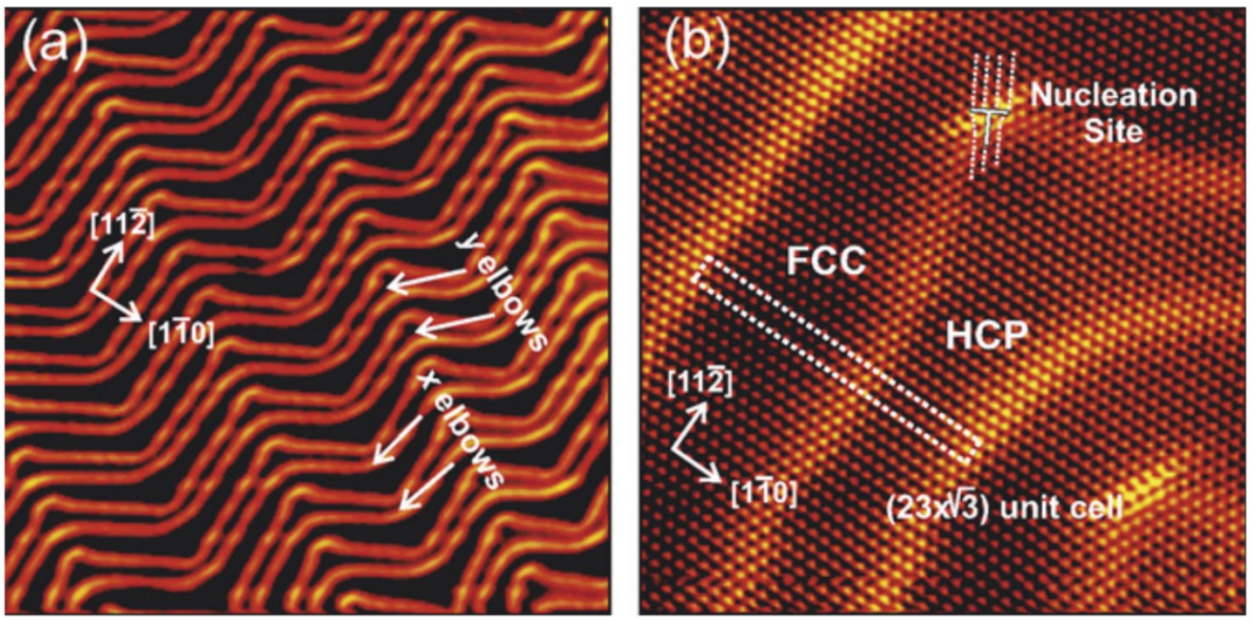

Figure 2.2 - (a) Herringbone reconstruction of a clean Au (111) surface. (b) Atom-resolved STM image of the Au (111) surface, showing the fcc and hcp areas. The $(22x\sqrt{3})$ unit cell is indicated by a rectangle. [2]

The Au (111) substrate was provided from MaTeck and is a hat-shaped single crystal of 99.999% purity, polished on the top side. This shape is required to fit on a molybdenum sample holder as shown in figure 2.2. The roughness of the polished side is lower than 30 nm, with orientation accuracy better than 0.1°.

Before each deposition the substrate has to be cleaned through cycles of sputtering and annealing, to remove impurities from the surface.

Several cycles of sputtering and annealing were made to ensure a clean surface on which to deposit the Molybdenum Disulfide:

- The sputtering with Ar+ ions is performed for 10 to 15 minutes at pressures between 6.5×10^{-6} to 1.2×10^{-5} torr, at a voltage of 1.5 kV
- The annealing is performed for 30 minutes, up to 1 hour at 600 to 650 °C. The sample is heated directly on the manipulator arm by a thorium-coated tantalum filament, achieving the ascending thermal ramp by raising the current by 0.2 A/min. The descending thermal ramp is achieved by lowering the current by 0.133 A/min.

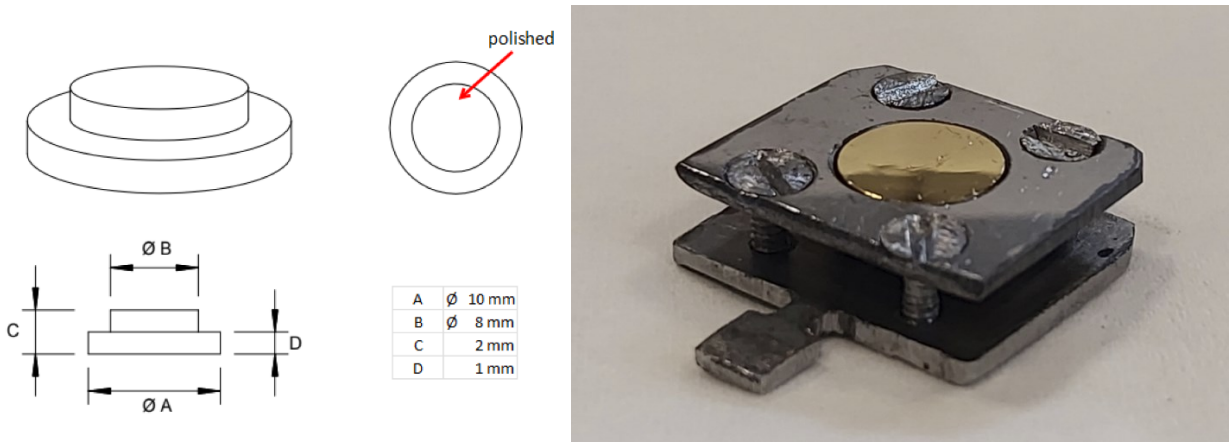

Figure 2.3 - Dimensions and shape of the Au (111) single crystal (left) and Au (111) crystal mounted on the sample holder.

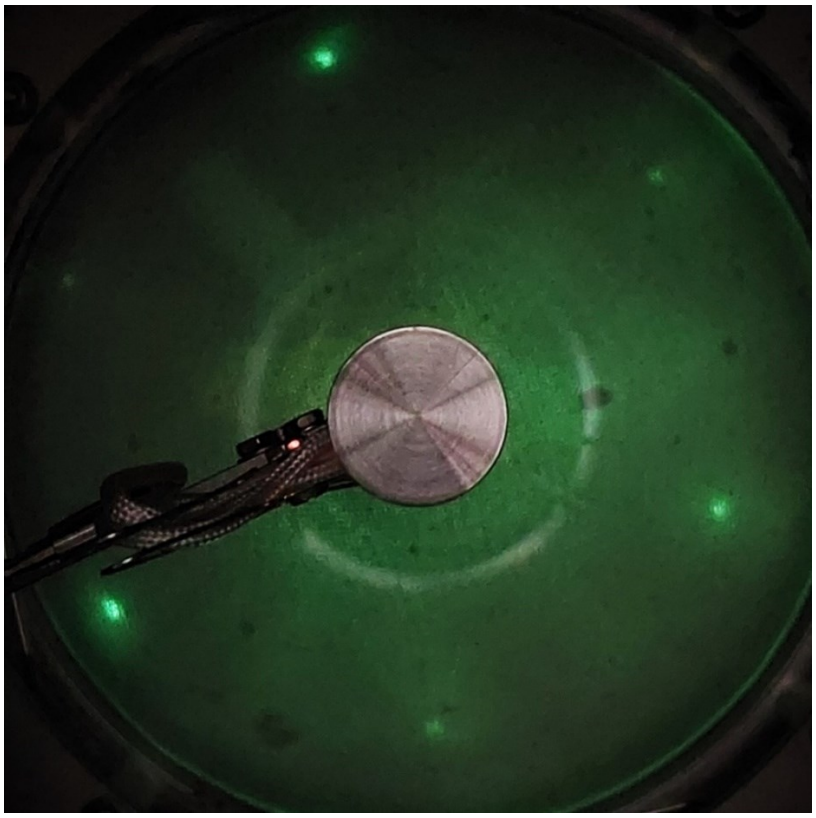

Figure 2.4 - LEED of the cleaned Au (111) crystal after sputtering and annealing.

2.2 Instrumentation

The Molybdenum is deposited by direct metal vapor deposition with an e-beam evaporator (e-flux evaporator by Tectra GmbH) loaded with a Mo rod, controlling the deposition rate by modifying either the emission current or the deposition time (figure 2.4). The flux of Mo vapors is allowed to hit the Au sample by opening a shutter in front of the Mo rod.

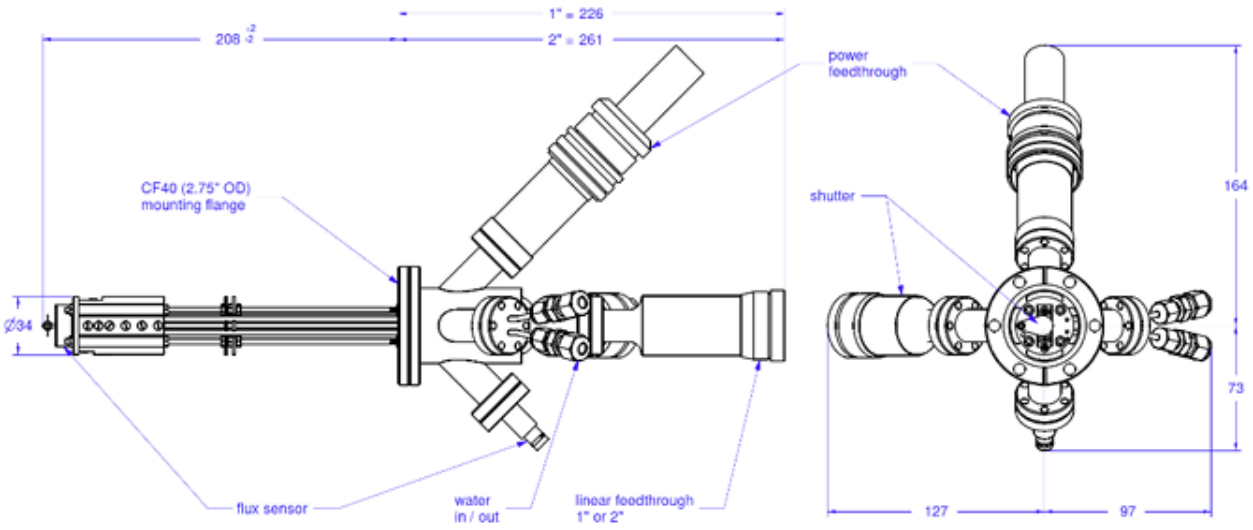

Figure 2.5 - Schematic view of the Tectra E-beam evaporator in which the Mo rod is mounted.

Because in this work Iron is to be used as a dopant for the MoS_2 surface, a Fe rod is mounted in another e-beam evaporator (EBE-4 configurable evaporator by SPECS).

The Mo rod loaded in the evaporator was purchased from Advent Research Materials as a one-meter long rod, 2.0 mm in diameter, of 99.95% purity. The Fe rod was purchased from Mateck as a one-meter long rod, 2.0 mm in diameter, of 99.99% purity. For loading into the evaporators, 2.5 cm long sections were cut from each rod and installed accordingly.

Sulfur is needed to form the MoS_2 layer, and during the deposition is dosed on the substrate by sublimation: for this purpose, a vial is filled with elemental sulfur powder of 99.998 % purity, sourced from Sigma Aldrich; the vial is then placed in a secondary chamber, adjacent to the preparation chamber and the low pressure allows the sulfur to sublimate. The elemental sulfur, now in gaseous form, mainly consists of S_2 and S_8 clusters, that enter the preparation chamber by opening a gate valve, which separates the latter from the secondary chamber hosting the sulfur vial. In later depositions, to atomize the sulfur clusters, a homemade cracker (an hot filament placed in front of the sulfur vial and heated to orange glowing) is used to heat up and atomize the sulfur in the secondary chamber, before and during the depositions.

2.3 Sample characterization

After the deposition of the MoS_2 on the surface of the Au (111) crystal, the sample is characterized by X-ray Photoelectron Spectroscopy (XPS), Low Energy Electron Diffraction (LEED), and Scanning Tunneling Microscopy.

2.3.1 X-ray Photoelectron Spectroscopy

X-ray photoelectron spectroscopy (XPS) is a powerful technique to identify the elements that constitute a surface and their chemical states. It uses electrons expelled from the sample surface when its atoms are irradiated with high-energy photons.

The process of photoelectric emission starts when high-energy photons, with wavelengths in the order of magnitude of X-rays, hit the sample's surface; these photons interact with electrons from the innermost atomic shells of the atom and can eject them. The ejected electrons can move through the solid and surface and are scattered in various processes: for this reason, photoemission only involves electrons that do not undergo inelastic scattering and manage to escape from the surface, therefore being emitted by atoms in the more superficial layers. [3,4]

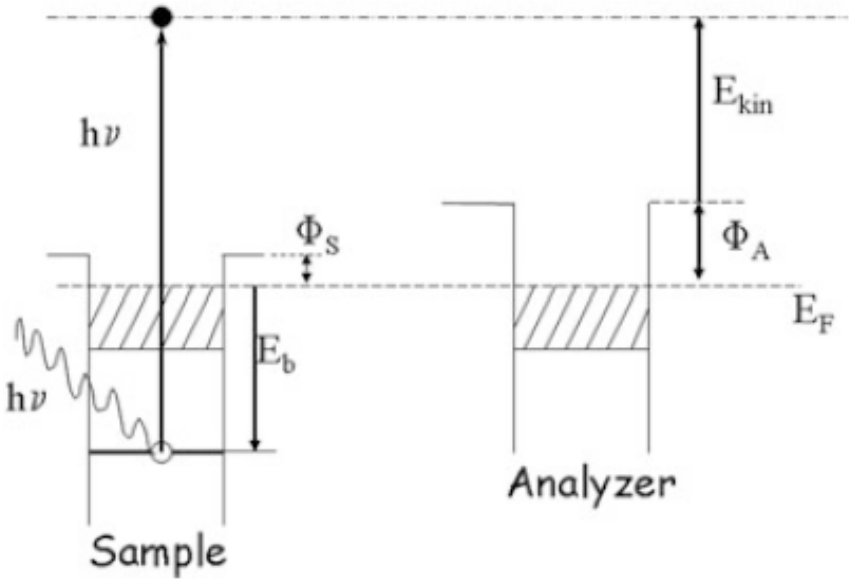

Figure 2.6 - Schematic example of the difference between energy levels in the sample and the analyzer, and shift of the Fermi Level when the two are put in electrical contact. [3]

The kinetic energy (KE) of the emitted photoelectrons is determined by the energy of the incident photon, the binding energy, and the sample's work function, ϕ_s:

$$KE = h\upsilon - BE - \varphi_s$$

The work function is defined as the potential energy difference to bring an electron from the highest occupied energy level of the material, i.e. from the Fermi level to the vacuum level. This vacuum level corresponds to the energy of an electron at rest at a point, in a vacuum, outside the surface.

When the sample is in electrical contact with the analyzer, the kinetic energy of the emitted electrons is diminished by the difference between the work function of the analyzer, ϕ_A, and of the sample, thus:

$$KE' = h\upsilon - BE - \varphi_s - (\varphi_A - \varphi_s) = h\upsilon - BE - \varphi_a$$

The work function of the analyzer can be found, through reference samples, by setting it to zero at the Fermi edge. [3–5]

The analyzer measures the energy of the emitted photoelectrons and, by knowing the work function of the analyzer and the energy of the photons that impact on the sample, the only energy left to determine is the binding energy. The binding energy is given by the equation:

$$BE = h\upsilon - KE' - \varphi_a$$

The binding energy refers to the energy difference between the initial energy of the atom with n electrons and the final energy of the ion with n-1 electrons, corresponding to the energy necessary to expel the photoelectron from the innermost shells of the atom.

Because the energy of an electronic state is determined not only by its electronic configuration but also, by its angular momentum, the spin-orbit coupling influences the binding energy. The total angular momentum of the electron results from the sum between the orbital angular momentum, l, and spin angular momentum, s, as expressed in the sum:

$$j = |l + s|$$

When one unpaired electron has orbital angular momentum $l > 0$ the total angular momentum is:

$$j = l \pm \left(\frac{1}{2}\right)$$

So for electrons from s orbitals, only one peak is present in the spectrum, while for electrons coming from p,d or f orbitals the peak is split in a doublet. Moreover, the degeneracy is equal to $2j + 1$, and determines how many combinations exist for a parallel or anti-parallel pairing of electrons; these combinations result in doublets whose individual peaks have well-defined intensity ratios: for example for a photoelectron that is expelled from a p orbital (which has l=1) the two peaks $p_{1/2}$ and $p_{3/2}$ have a ratio of intensity 1:2, however for photoelectrons expelled from d orbitals (which has l=2) the intensity ratio for the $d_{3/2}$ and $d_{5/2}$ peaks is 2:3. The notation for the peaks indicates the main quantum number, the electron configuration, and if present, the subscript denotes the total angular momentum for the considered peak. [3,5]

Chemical bonding can also influence the electronic configuration of the atom, causing an energy shift known as a chemical shift. As a good approximation, it's possible to assume that the chemical shift is dependent solely on initial state effects, caused by chemical bonding, and that all core levels in an atom shift to the same extent. The chemical shift is influenced by the oxidation state of the atom and, generally, as the oxidation state increases, the binding energy increases. This is because if the positive charge on the atom is larger, the binding energy experienced by the photoelectron will be higher. [3,4]

The binding energy positions of the photoemission peaks produced by the the samples are compared to database found in the literature for pure elements or materials, making it possible to identify the sample elements qualitatively and quantitatively.

The peaks obtained in XPS would theoretically be Lorentzian curves with linewidth, ΔE_0, inversely proportional to the lifetime of the core hole state, τ, that results from the photoemission process.

$$\Delta E_0 = \frac{h}{\tau}$$

With h being Planck constant.

However, for crystalline materials, atomic vibrations impose a small Gaussian broadening on the peak shape, and in practice, for many materials, the peaks are well represented by a convolution of a Lorentzian function with a Gaussian, called Voigt function.

In conducting materials, electrons present at the Fermi edge can interact with emitted photoelectrons, resulting in many-bodies interactions, and for this reason, the peak presents a tail at higher energies. For this type of peak, the curve can be reconstructed using a Lorentzian function with an asymmetric component, called Doniach-Sunjic line shape. [3–5]

2.3.2 Low Energy Electron Diffraction

Diffraction techniques are often used for the study of solids, being able to probe the long-range order of a crystal or a crystalline surface. The Bragg or von Laue equations allow to find the conditions for constructive interference. With Bragg's equation, it's possible to find the conditions for constructive interference as a relation between the interplanar distance, a, the observation angle, θ, and the electromagnetic radiation of wavelength λ as:

$$n\lambda = a\ sin\theta$$

With n an integer number. [3,6,7]

For a particle, the estimated wavelength can be calculated using the De Broglie equation:

$$\lambda = \frac{h}{m_e v}$$

With h Planck's constant, me is the mass of the particle, and v its velocity. [3] The wavelength of electrons can be easily found using the equation:

$$\lambda(\text{Å}) = \sqrt{\frac{150.4}{E\ (eV)}}$$

With E the energy of the electrons.

While X-rays penetrate deeply into matter, in the order of 100 Å, and allow to study the bulk crystalline lattice, they can be used in the study of the surface of a crystal only at glancing angles. A more widely used diffraction technique for the study of surface meshes is electron diffraction, such as Low Energy Electron Diffraction (LEED), in which electrons penetrate and can escape only from a depth in the order of 10-100 Å. [6]

In particular, Low Energy Electrons interact strongly with matter leading to a very short inelastic mean free path, which means only 3 to 4 atomic layers contribute to diffraction. [3]

LEED uses a beam of electrons diffracted on the 2D surface lattice, which are then collected on a fluorescent screen. The Bragg equation can be used to estimate the positions of the main diffraction spots, called the Bragg peaks, having obtained the electron wavelength from the De Broglie equation. The energies of the electrons used are usually in the range of 20 to 200 eV. [6,7]

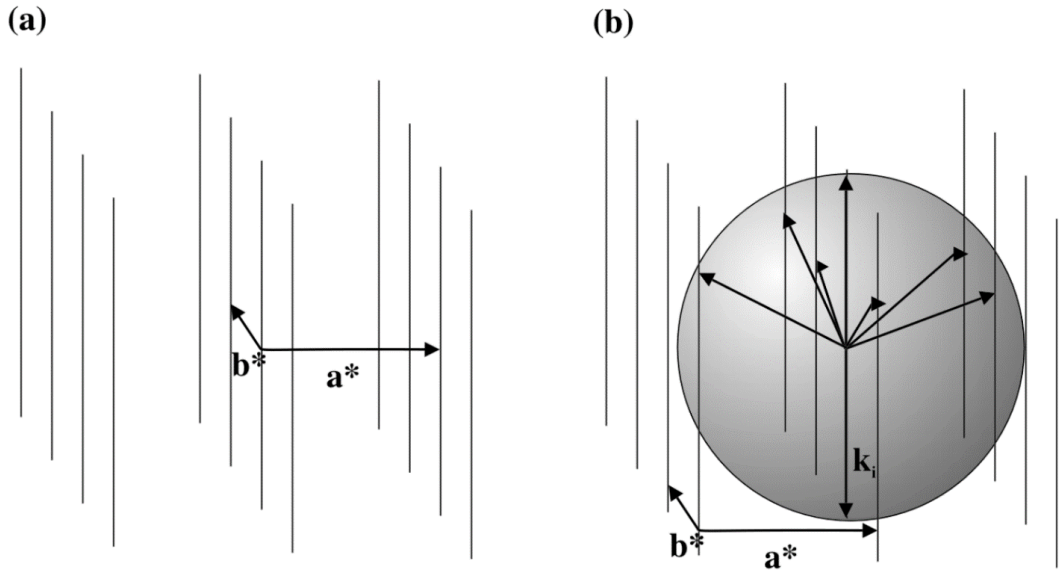

Figure 2.7 - (a) Reciprocal lattice vectors and the reciprocal lattice rods. (b) Ewald sphere construction, showing the intercepts with the projected rods. The incident wavevector is noted as k_i. [8]

The diffraction spots may be thought of as intercepts between the surface rods, projected from the point surface reciprocal lattice and perpendicular to it, and a construction called the Ewald sphere (figure 6) whose radius is given by the wavevector of the electron beam impinging on the surface in normal direction. The diffracted electron beam produced specific spots on a fluorescent screen, which allow the identification of the vectors of the reciprocal lattice labelled with the indices hk:

$$g = hc_1^* + kc_2^*$$

With c_1^* and c_2^* primitive vectors of the reciprocal lattice. [7,8]

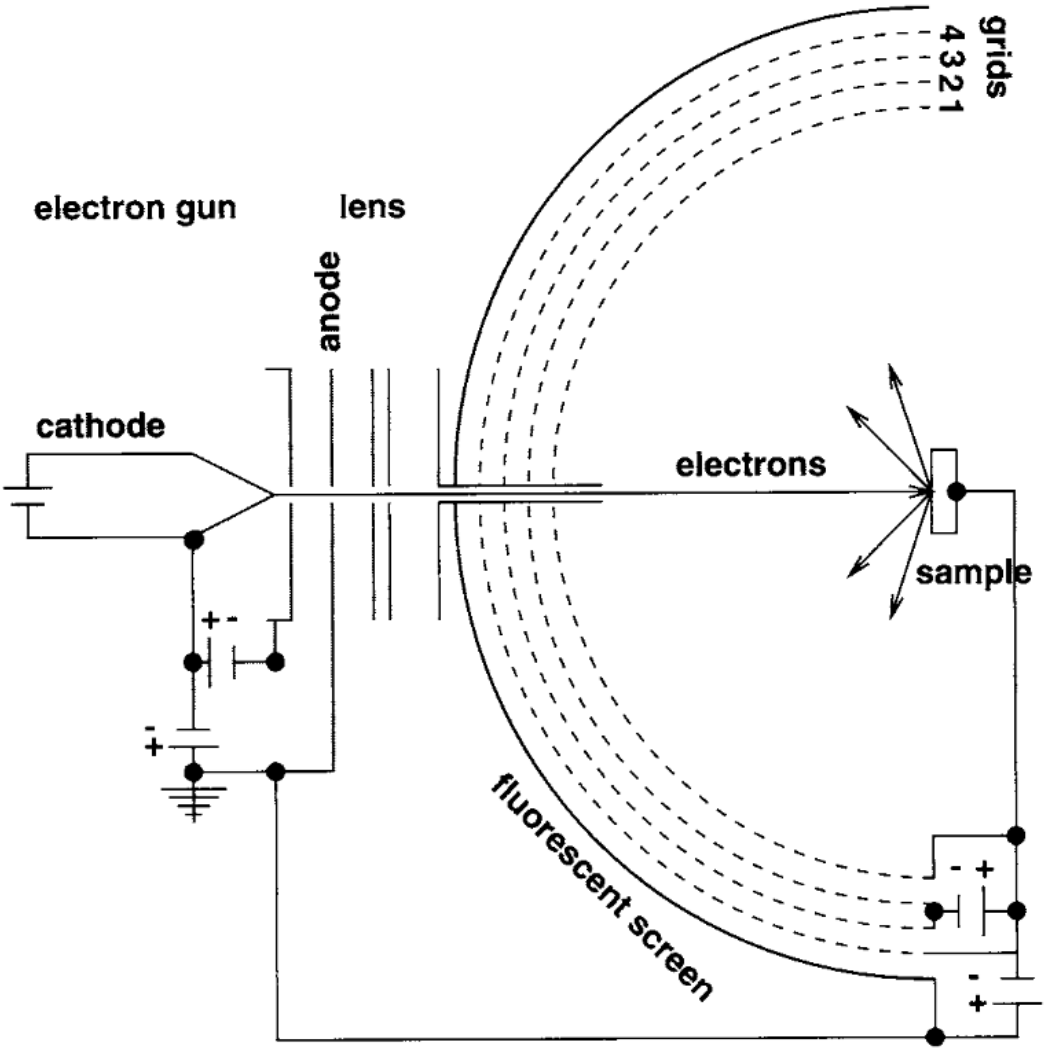

Figure 2.8 - Schematic view of a LEED experiment with a fluorescent screen. [6]

2.3.3 Scanning Tunneling Microscopy

Scanning Tunneling Microscopy belongs to the larger class of scanning probe microscopy imaging modes, and is a very powerful technique, capable of achieving atomic resolution.

In this kind of microscopy a probe, typically a sharp tip etched from a W or Pt/Ir wire, is mounted on piezo-electric crystals. For this kind of microscopy, both the tip and sample have to be made of conductive material. [3,6,9,10]

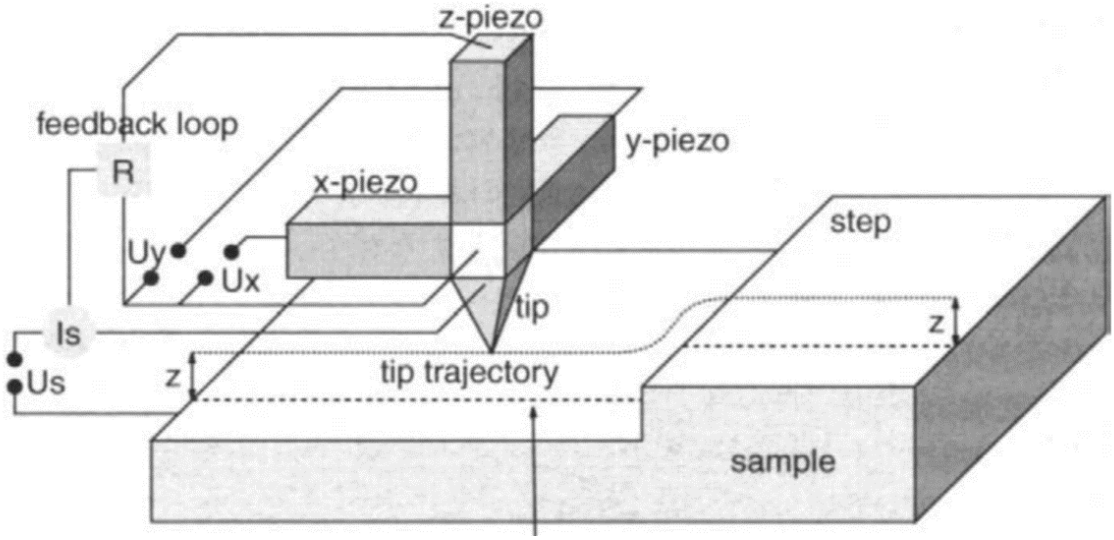

Figure 2.9 - Schematic illustration of the working principles of an STM. [6]

The tip is brought at a distance in the order of fractions of nanometers from the sample surface, as the vacuum gap between the tip and the surface represents an energy barrier for electron waves, whose magnitude can be approximated by the average work function of the tip and the sample. The electron waves in the conductive material of either tip or sample can move quasi-freely, while they are exponentially dampened in the region of the barrier, depending on the tip to sample separation and work function:

$$I \propto e^{-2\kappa d} \;\; with\, \kappa = \frac{\sqrt{2m\overline{\Phi}}}{\hbar}$$

where I is the tunneling current, d is the width of the gap, m is the mass of the electrons and $\overline{\Phi}$ is the height of the energy barrier. [6,7,9,11] Because the wavefunction of the electrons in the tip and the sample surface have a slight overlap, finite tunneling conductance is generated. [10] The tunneling current results from the movement of electrons from the tip to the surface of the sample when a voltage bias, V, is applied between the two. [6,7,11] Typical tunneling currents are in the order of 1 nA, corresponding to a distance between tip and sample in the order of 10 Å. [6]

The piezoelectric elements, which expand or contract upon application of a voltage, on which the tip is mounted are three mutually perpendicular piezoelectric transducers that move the tip in the three axes x, y, and z. The vertical movement is controlled by the z-piezo, and the height of the tip is controlled by the feedback circuit, in order to maintain constant the current. This imaging mode is called constant current imaging, and the topographic signal is generated by the feedback signal to the z piezoscanner. Meanwhile, a voltage ramp is applied on the y piezo and a sawtooth potential is applied to the x piezo to scan the tip on the xy plane. [10] In constant current mode, the measured current is converted to a voltage and then compared to a reference value, the tip is then withdrawn or moved closer to the surface to re-establish the current close to the reference value. This mode of operation allows the observation of samples that are not flat on an atomic scale, but because of the feedback loop response time, scan speeds have to be relatively low.

STMs can operate also at constant height mode, where the tip is kept at an established height above the sample while measuring point by point the tunneling current.

In constant current mode, the measured current is converted to a voltage and then compared to a reference value, the tip is then withdrawn or moved closer to the surface to re-establish the current close to the reference value. This mode of operation allows the observation of samples that are not flat on an atomic scale, but because of the feedback loop response time, scan speeds have to be relatively low. In reality, the image does not represent a true topological profile but a surface of density of states with constant Fermi-level. For planar tunneling, the current is found as:

$$I \propto \int_0^{eU} \rho_s(E) D(E) dE$$

With ρ_s the surface density of states at energy E from the Fermi-level, and D(E) the transmission probability through the barrier; U is the sample to tip bias.[3,6,10]

With constant height mode, scanning speeds are considerably higher, reducing image distortions given by thermal drifts and hysteresis of the piezoelectric elements, and dynamic processes on the sample surface can be followed better. However, in constant height mode, it's more difficult to extract topographic height, as the tunneling current is often not known exactly and it's the only source of topographic information for this operating mode. [3,6,9]

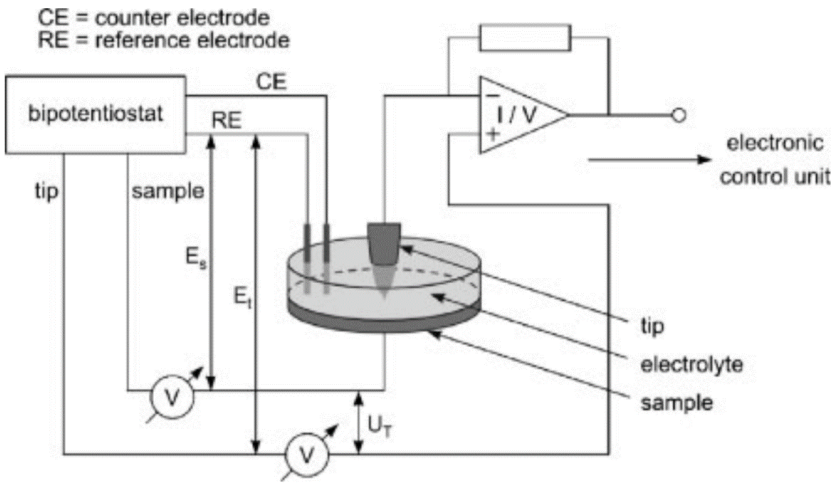

Figure 2.10 – Schematic experimental set-up for in situ STM. E_s and E_t are, respectively, the potential of the sample and the tip, which can be controlled independently. [12]

Unlike other kinds of microscopy, such as Transmission Electron Microscopy, STM is not limited by the need for UHV, but it can achieve atomic resolution also in air or liquid. In particular, STMs can be employed to obtain images of surfaces when combined with electrochemical methods. In this case, the STM tip becomes the fourth electrode in a standard electrochemistry cell (figure 2.9), where the Working Electrode is the substrate being studied.

The reference electrode in the case of this work is a platinum wire submerged in the electrolyte solution, but it can also be a Standard Calomel Electrode (SCE) or other kinds of reference electrodes. The counter electrode has to close the circuit with the Working Electrode, and in the case of this work consists of a gold wire also submerged in the electrolyte solution.

When the imaging occurs in solution, the tip has to be coated with an insulating thin film, except for the very end of the tip, to reduce as much as possible the surface of the tip exposed to the electrolyte. [10,12] While submerged in the electrolyte solution, the tip becomes a fourth electrode and electrochemical processes will occur at the interface between tip and solution as well; these processes give rise to a current at the tip which is superimposed to the tunnel current and causes interference to the feedback circuit, leading to imaging errors and malfunctions. Since the tip potential can be controlled via a bipotentiostat, it may be set to be as close as possible to the resting potential. By controlling the potential of the tip and by reducing the exposed area of the tip, thus reducing electrochemical processes, imaging malfunctions in solution can be mitigated. [12]

Bibliography for Chapter 2

1. Kolb, D. M., Dakkouri, A. S. & Batina, N. The Surface Structure of Gold Single-Crystal Electrodes. in *Nanoscale Probes of the Solid/Liquid Interface* (eds. Gewirth, A. A. & Siegenthaler, H.) 263–284 (Springer Netherlands, Dordrecht, 1995). doi:10.1007/978-94-015-8435-7_15.
2. Morgenstern, K., Kibsgaard, J., Lauritsen, J. V., Lægsgaard, E. & Besenbacher, F. Cobalt growth on two related close-packed noble metal surfaces. *Surf. Sci.* **601**, 1967–1972 (2007).
3. Kolasinski, K. W. *Surface Science: Foundations of Catalysis and Nanoscience*.
4. Hofmann, S. *Auger- and X-Ray Photoelectron Spectroscopy in Materials Science: A User-Oriented Guide*. vol. 49 (Springer Berlin Heidelberg, Berlin, Heidelberg, 2013).
5. *Handbook of X-Ray Photoelectron Spectroscopy: A Reference Book of Standard Spectra for Identification and Interpretation of XPS Data*. (Perkin-Elmer Corporation, Eden Prairie, Minn, 1992).
6. Speller, S., Heiland, W. & Schleberger, M. Chapter 1 - SURFACE CHARACTERIZATION: COMPOSITION, STRUCTURE AND TOPOGRAPHY. in *Handbook of Surfaces and Interfaces of Materials* (ed. Nalwa, H. S.) 1–53 (Academic Press, Burlington, 2001). doi:10.1016/B978-012513910-6/50020-7.
7. Kittel, C. *Introduction to Solid State Physics*. (Wiley, Hoboken, NJ, 20).
8. Diehl, R., Ledieu, J., Ferralis, N., Szmodis, A. & Mcgrath, R. Low-energy electron diffraction from quasicrystal surfaces. *J. Phys. Condens. Matter* **15**, R63 (2003).
9. *Scanning Tunneling Microscopy I: General Principles and Applications to Clean and Absorbate-Covered Surfaces*. vol. 20 (Springer Berlin Heidelberg, Berlin, Heidelberg, 1994).
10. Chen, C. J. & Smith, W. F. Introduction to Scanning Tunneling Microscopy. *Am. J. Phys.* **62**, 573–574 (1994).
11. DiNardo, N. J. *Nanoscale Characterization of Surfaces and Interfaces*. (VCH, Weinheim, 1994).
12. Tierney, H. L. & Sykes, E. C. H. Scanning Tunneling Microscopy in Surface Science, Nanoscience and Catalysis. *J. Am. Chem. Soc.* **132**, 11387–11387 (2010).

Chapter 3 - Deposition of MoS_2

3.1 Deposition trials

Initially, a satisfactory procedure to obtain a single layer of pure and structurally ordered MoS_2 had to be found. The finalized deposition procedure had to be determined from several trials, inspired by a previous work by Cattelan et al., in which WS_2 was deposited on a Ni (111) crystal and other works in the literature on MoS_2 growth under UHV conditions. [1,2] Parameters such as substrate temperature, energy supplied to the evaporators and time of exposure of the substrate to the sulfur and metal vapors, were changed in order to optimize the deposition of a film of MoS_2.

3.1.1 First deposition

For the deposition, the Au (111) crystal is first heated to the deposition temperature, T_d, then it is exposed to vapors of elemental S, made up of mostly S_2 and S_8 clusters, for 10 minutes before the metal deposition. The deposition of Mo then begins by opening the shutter regulating the Mo flow from the E-Beam evaporator for 20 minutes, while still dosing S in the chamber; the pressure in the preparation chamber during the deposition increases to 3.0×10^{-8} torr. After the metal deposition, the sample's temperature is brought and kept at the annealing temperature, T_a, for 5 minutes, while still dosing sulfur. After the post-deposition treatment, the S vapor flow is shut off and the sample is allowed to cool to room temperature. The conditions used for the deposition are described in table 3.1.

Table 3.1 - Conditions of the experimental parameters for the first deposition.

Temperature control parameters			
Heating speed	**22 K/min**	**Cooling speed**	**16.5 K/min**
T_d (°C)	**120**	**T_a (°C)**	**400**
E-Beam evaporator parameters			
	Applied bias (kV)	**Emission current (mA)**	**Filament current (A)**
Mo E-beam parameters	**1.15**	**70.0**	**4.5**

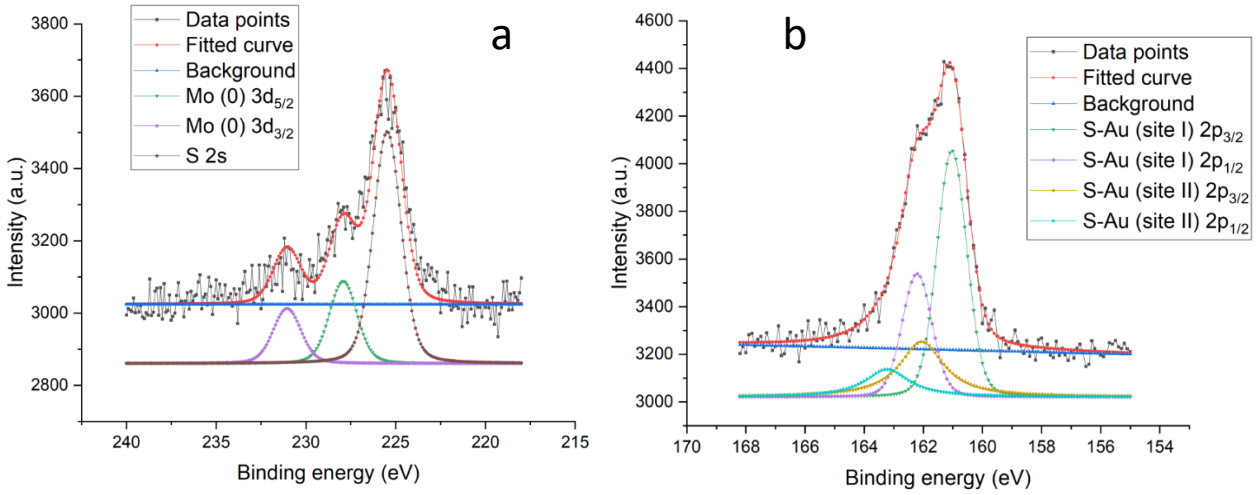

Figure 3.11 - XPS spectra for (a) Mo 3d and (b) S 2p orbitals of the first deposition attempt.

The chemical nature of the deposited layer was investigated by XPS. Notably, in figure 3.1a, the S 2p and Mo 3d peaks are observed in the same binding energy (BE) region, requiring therefore a fitting procedure to distinguish the chemical origin of the different signals. The data are fitted with multiple Voigt curves, and the corresponding peaks are compared to those reported in the literature: the spectrum in figure 3.1a shows a large peak that corresponds to the S 2s orbital, at a BE of 225.6 eV, and two smaller peaks, at BE of 227.9 and of 231 eV, that correspond to those of the Mo 3d orbitals of metallic molybdenum. [3–5] In the multipeak analysis of the spectrum, only the peaks associated with the metallic component can be distinguished, while no signal of the desired Mo^{4+} is present. Further information is deduced by the analysis of the S 2p photoemission peak, in this case, showing two major for peaks for S $2p_{3/2}$ and $2p_{1/2}$, at 161.2 and 162.4 eV respectively, which have been attributed to a sulfur chemisorption phase on Au. The less intense peaks at 162.1 and 163.3 eV are similarly attributed to sulfur chemisorbed on the Au (111) surface but on different adsorpiton sites. [6–8]

Figure 3.12 - LEED after the first deposition, $I_{filament}$=1.730 A, Bias=45 V. No reconstruction is observed, but the points usually observed for Au (111) look less intense (highlighted in the red circles).

From the LEED pattern obtained after the deposition is very faint, almost identical to that of the clean Au (111) substrate and, combined with the observations form the XPS spectra, it can be concluded that in this attempt it was not possible to form an ordered layer of MoS_2.

Since the attempt did not yield a film of MoS_2 on the surface of theAu (111), to supply sufficient energy to promote the reaction between Mo and S, it was decide to significantly increase the temperature of the substrate.

3.1.2 Second deposition

The Au (111) crystal is heated to deposition temperature, T_d, before being exposed to S vapors for 5 minutes. The pressure inside the preparation chamber, after the flow of S vapors is let in, reached $2.2x10^{-8}$ torr. Conditions for temperature control and the parameters for the e-beam evaporator of Mo are reported in table 3.2. Mo vapors are dosed on the substrate for 10 minutes, while maintaining the S flow, then the Mo vapor is shut off. After the deposition of Mo, the sample is kept at deposition temperature for 5 minutes. With the S flux still present, the sample temperature is then lowered to the post-treatment temperature, T_a, and

kept at this temperature for 5 minutes. The flow of S vapor is then shut off and the sample is allowed to cool to room temperature.

Table 3.2 - Conditions of the experimental set-up for the second deposition.

Temperature control parameters			
Heating speed	**22 K/min**	**Cooling speed**	**16.5 K/min**
T_d (°C)	**400**	**T_a (°C)**	**250**
E-Beam evaporator parameters			
	Applied bias (kV)	**Emission current (mA)**	**Filament current (A)**
Mo E-beam parameters	**1.10**	**45.0**	**7.5**

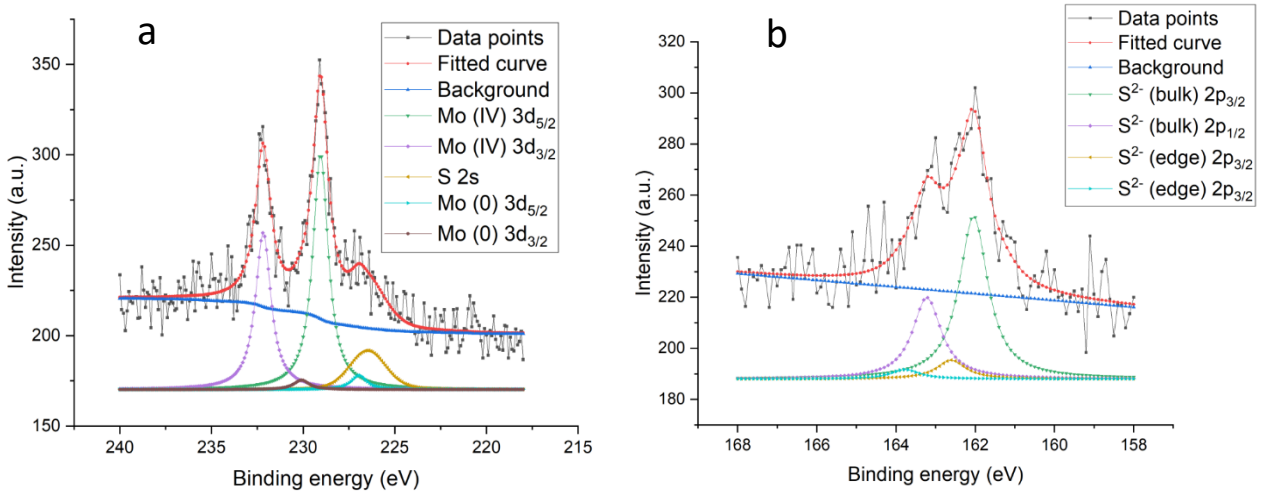

Figure 3.13 - XPS spectra for (a) Mo 3d and (b) S 2p orbitals of the second deposition attempt.

The spectrum shown in figure 3.3a displays the doublets of Mo $3d_{5/2}$ and $3d_{3/2}$ centered at BE of 229.1 and 232.2 eV respectively, corresponding to the desired Mo^{4+}, however another peak for S 2s with its maximum at 226.8 eV. an additional doublet at 226.9 and 230.2 eV is necessary for a good fit, which indicates the presence of some metallic molybdenum in direct contact with the surface of the Au (111) crystal that did not react. [9,10]

In figure 3.3b, the peaks for S $2p_{3/2}$ and $2p_{1/2}$ show their respective maximum at BE of 161.9 and of 163.1 eV, attributed to the monosulfide (S^{2-}) bonded to the Mo^{4+} ions. These peaks are a first indication that the reaction between Mo and S, at least partially, occurred as intended. Alongside these peaks, an additional doublet, at 162.4 and 163.6 eV, is used in the fit and is attributed to monsulfide ions along the step-edges. [6,11,12]

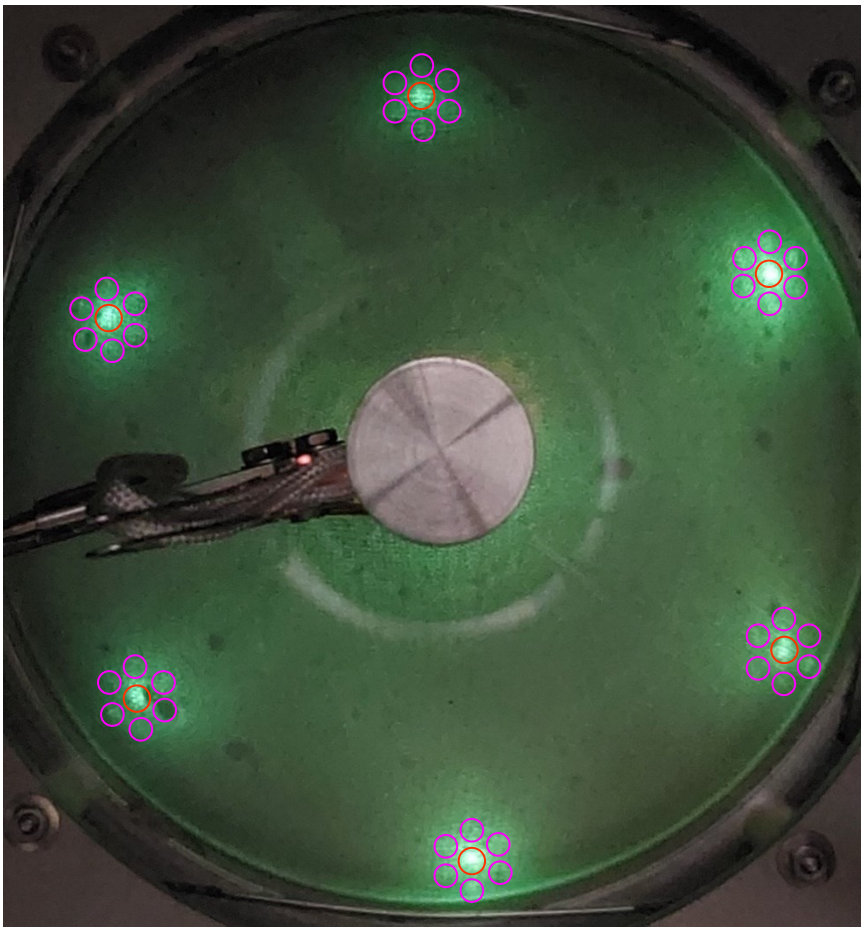

Figure 3.14 - LEED after the second deposition, $I_{filament}$=1.730 A, Bias=60 V. It is possible to observe the brighter spots of the Au (111) surface (highlighted in the red circles) surrounded by six spots, a pattern recognizable as the desired reconstruction given by the Moiré pattern of MoS_2 on Au (111) (highlighted with the purple circles).

The LEED of the prepared film, in figure 3.4, shows additional spots in the pattern previously not observed, which correspond to the spots reported in the literature for MoS2 films on Au (111). [13,14] This deposition attempt was almost successful; however, it still did not yield a pure layer of MoS_2, presenting a considerable amount of metallic molybdenum on the surface. In the following deposition, an attempt was made to ensure the sulfurization of Mo by forming an atmosphere of sulfur vapors before the deposition of the metal on the substrate.

3.1.3 Third deposition

To determine whether or not it is necessary to create an atmosphere of sulfur vapor before the deposition of molybdenum, the simultaneous deposition of sulfur and molybdenum was attempted. First, the Au (111) crystal is heated to and kept at the deposition temperature, T_d. The Mo rod e-beam parameters and temperatures used in the procedure are reported in table 3.3. The sulfur and molybdenum vapors are dosed simultaneously on the Au crystal for 20 minutes. The pressure in the preparation chamber after the opening of the S flow is 2.8×10^{-8} torr. After the deposition of Mo, the flow of S on the substrate is maintained for 10 more minutes at the deposition temperature. Afterwards the sample temperature is lowered and kept at

post-treatment temperature, T_a, for 5 minutes, while still maintaining the S gas flow. The flow of S vapor is then shut off and the sample is allowed to cool to room temperature.

Table 3.3 – Conditions of the experimental set-up for the third deposition.

Temperature control parameters			
Heating speed	**22 K/min**	**Cooling speed**	**16.5 K/min**
T_d (°C)	**300**	**T_a (°C)**	**170**
E-Beam evaporator parameters			
	Applied bias (kV)	**Emission current (mA)**	**Filament current (A)**
Mo E-beam parameters	**1.00**	**50.0**	**8.0**

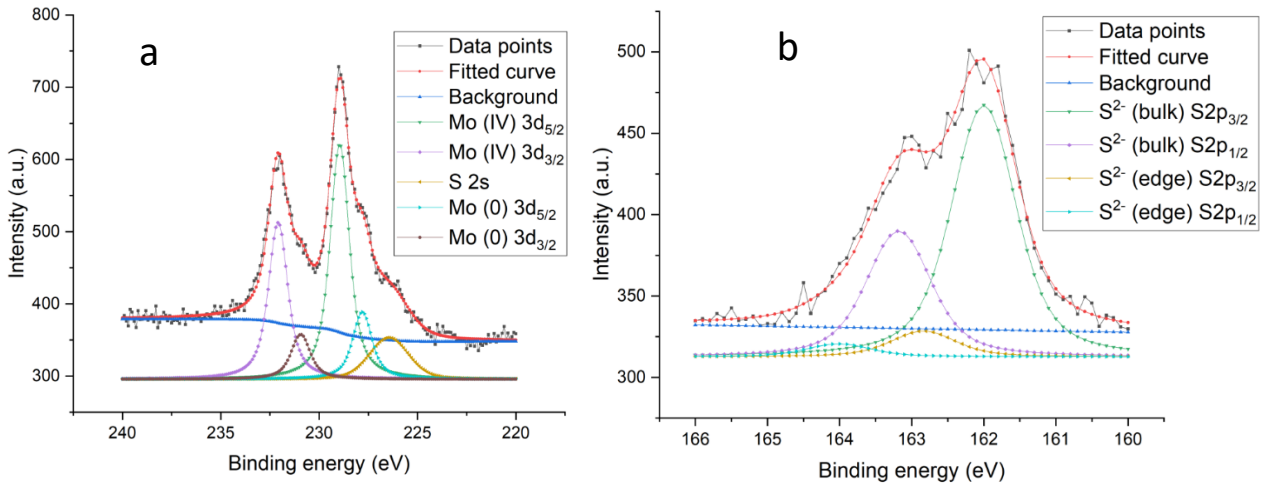

Figure 3.15 - XPS spectra for (a) Mo 3d and (b) S 2p orbitals of the third deposition attempt before annealing under a current of sulfur.

Again this attempt did not yield a pure layer of MoS_2, since a noticeable shoulder at 227.6 and 230.9 eV, corresponding to metallic molybdenum, can be observed in the photoemission spectrum of Mo 3d.

The peaks associated with sulfur are found at 226.8 eV, corresponding to the orbital S 2s, and at 162.0 and 163.2 eV, corresponding to the S $2p_{3/2}$ and $2p_{1/2}$ orbitals. Also present, are peaks attributed to sulfur in contact with the substrate at BE of 162.9 eV and 164.1 eV.[15,16]

Because a noticeable presence of metallic molybdenum was found in this deposition, further sulfurization of the deposited material is attempted by annealing the sample at 200 °C, under a flux of S vapors at a pressure of 2.6×10^{-8} torr, for 15 minutes. However, as shown in figure 3.6, the material already deposited was not sulfurized to any appreciable extent.

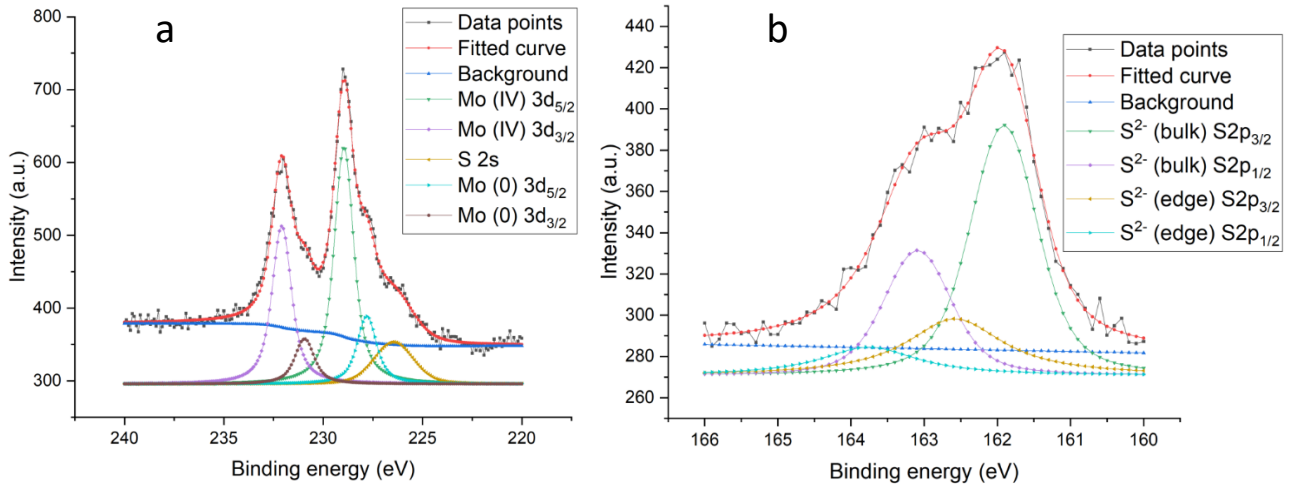

Figure 3.16 - XPS spectra for (a) Mo 3d and (b) S 2p orbitals of the third deposition attempt after annealing under a current of sulfur.

Unfortunately this post deposition sulfurization did not yield satisfactory results, as confirmed by the comparison of the spectra in figure 3.5 (before) and 3.6 (after) that are nearly identical. The LEED pattern, in figure 3.7, also presents very blurry spots, possibly because of the presence of adsorbed sulfur species, whose XPS peaks could be undistinguishable from the other peaks.

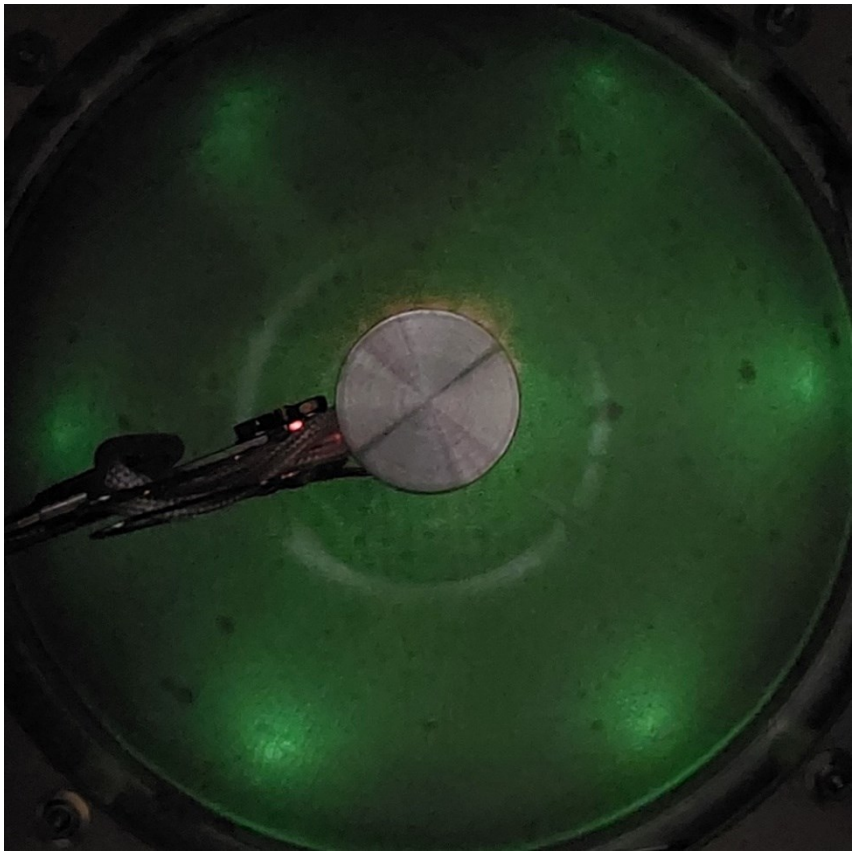

Figure 3.17 - LEED, $I_{filament}$=1.730 A, Bias=60 V, of the sample after the annealing under sulfur gas flow. The points are very out of focus, but it is still possible to distingush very weak points from the Moiré pattern.

3.1.4 Fourth deposition

To further investigate whether or not sulfurization of the sample is possible, in the fourth deposition attempt, the material was deposited and then further exposed to S vapors after the deposition. Firstly, the Au (111) crystal is heated and kept at temperature, T_d, through the deposition. Because the simultaneous deposition was not succesful, it was decided to continue to start the sulfur gas dosing before the deposition of molybdenum. The sulfur gas dosing on the substrate, at a pressure of $2.6x10^{-8}$ torr, starts 3 minutes before the Mo deposition. The parameters for the e-beam molybdenum evaporator and the temperatures recorded during the preparation are reported in table 3.4. The substrate is exposed to Mo vapor for 5 minutes, then the Mo flow is shut off while maintaining the flow of S vapor. After the deposition of Mo, the sample is kept at the deposition temperature for 10 minutes. The sample temperature is then lowered and kept at the post-treatment temperature, T_a, for 5 minutes, while still maintaining a S backpressure. The flow of S vapor is then shut off and the sample is allowed to cool to room temperature.

Table 3.4 -Conditions of the experimental set-up for the fourth deposition.

Temperature control parameters			
Heating speed	**22 K/min**	**Cooling speed**	**16.5 K/min**
T_d (°C)	**450**	**T_a (°C)**	**250**
E-Beam evaporator parameters			
	Applied bias (kV)	**Emission current (mA)**	**Filament current (A)**
Mo E-beam parameters	**1.00**	**50.0**	**8.0**

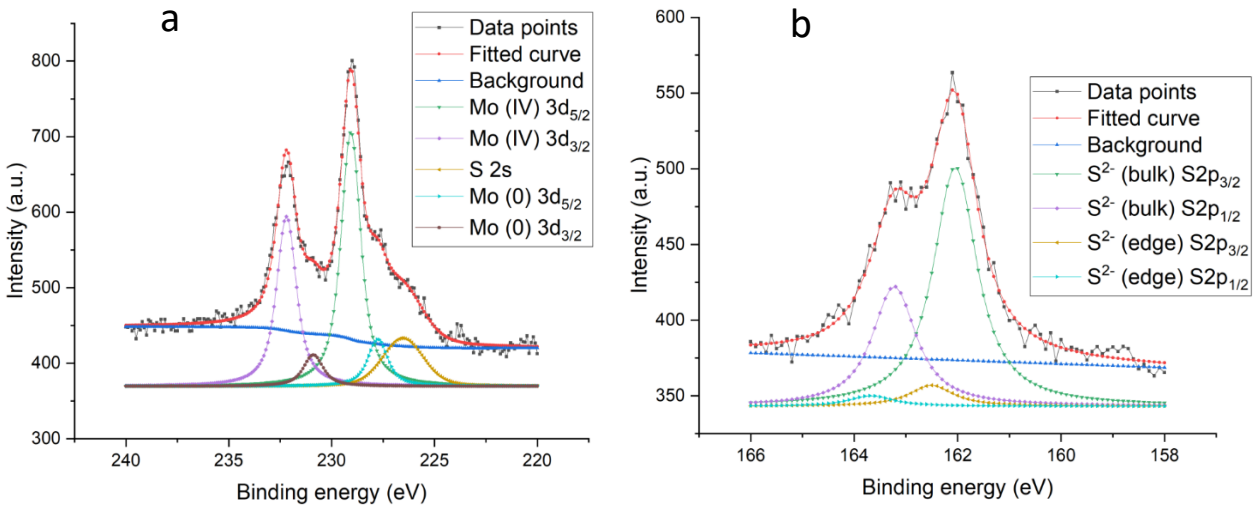

Figure 3.18 - XPS spectra for (a) Mo 3d and (b) S 2p orbitals of the fourth deposition attempt before annealing under a flux of sulfur.

After the deposition, as shown in figure 3.8a, a noticeable amount of metallic Mo is present on the surface of the crystal. In order to investigate whether or not it is possible to sulfurize the metallic molybdenum the sample was first heated to 550 °C and kept at this temperature, then the sample as exposed to a S backpressure of $2.3x10^{-8}$ torr for 30 minutes. Afterwards, the S flow was shut off and the sample was allowed to cool to room temperature. This procedure is unsatisfactory for the production of pure MoS_2: while some of the molybdenum is sulfurized, there is still a significant component of metallic molybdenum on in the sample. It is possible that molybdenum clusters are still present and mostly covered by a layer of MoS_2, forming some sort of core@shell Mo@MoSx nanoparticles.

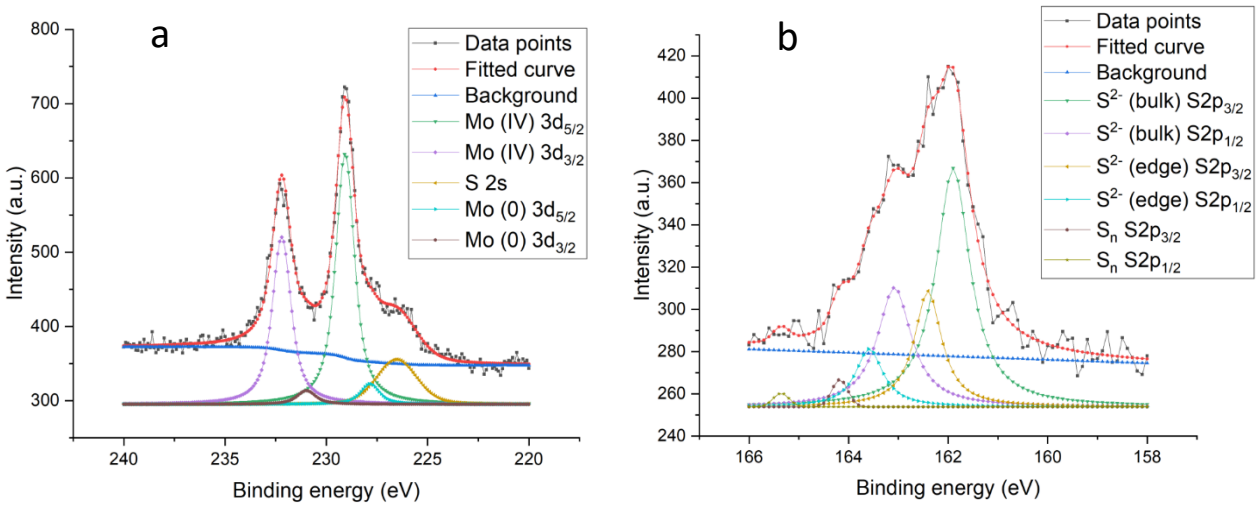

Figure 3.19 - XPS spectra for Mo 3d (left) and S 2p orbitals (right) of the fourth deposition attempt after annealing under a flux of sulfur.

The material deposited on the surface was sulfurized further in this attempt, as it can be seen by confronting the spectra for the Mo 3d in figure 3.8 and 3.9, but a fraction of metallic molybdenum still remained on the surface. It is possible that metallic molybdenum clusters are still present and mostly covered by a layer of MoS_2, which acts as a barrier to further sulfurization. These spectra 3d exhibit only a small difference between figure 3.8a and 3.9. The spectra for S 2p share doublets for monosulfide in the bulk of the film, at 162.0 and 163.2 eV, and 161.9 and 163.0 eV, and for the mono/di-sulfide at the edges, at 162.6 and 163.8 eV, and 162.5 and 163.6 eV, respectively for the film before and after the sulfurization. The only difference between these spectra seems to be that, after the sulfurization, the intensity of the peaks of the edge sulfide ions increases and there is the presence of an additional doublet, at 164.2 and 165.3 eV, attributed to the polysulfide.

3.1.5 Fifth deposition

The Au (111) crystal is heated and kept at temperature, T_d, before the deposition of Mo; after the crystal has reached the desired deposition temperature, the sulfur gas is dosed on the substrate beginning 5 minutes before the Mo deposition, raising the pressure inside the preparation chamber to $2.4x10^{-8}$ torr. The

temperature control and e-beam evaporator parameters for the deposition are reported in table 3.5. Mo vapors are dosed on the substrate for 25 minutes, then shut off. Afterwards the sample temperature is kept at T_d for 15 minutes, while maintaining the S atmosphere. The sample temperature is then lowered to post-treatment temperature, T_a, and kept at this temperature for 5 minutes. The flow of S gas is then shut off and the sample is allowed to cool to room temperature.

In this attempt, the deposition time is longer while the power supplied to the Mo evaporator is lower than in the previous deposition. By changing these parameters, the Mo/S ratio is changed in order to more effectively sulfurize the metal.

Table 3.5 - Conditions of the experimental set-up for the fifth deposition.

Temperature control parameters			
Heating speed	**22 K/min**	**Cooling speed**	**16.5 K/min**
T_d (°C)	**450**	**T_a (°C)**	**250**
E-Beam evaporator parameters			
	Applied bias (kV)	**Emission current (mA)**	**Filament current (A)**
Mo E-beam parameters	**1.10**	**40.0**	**7.8**

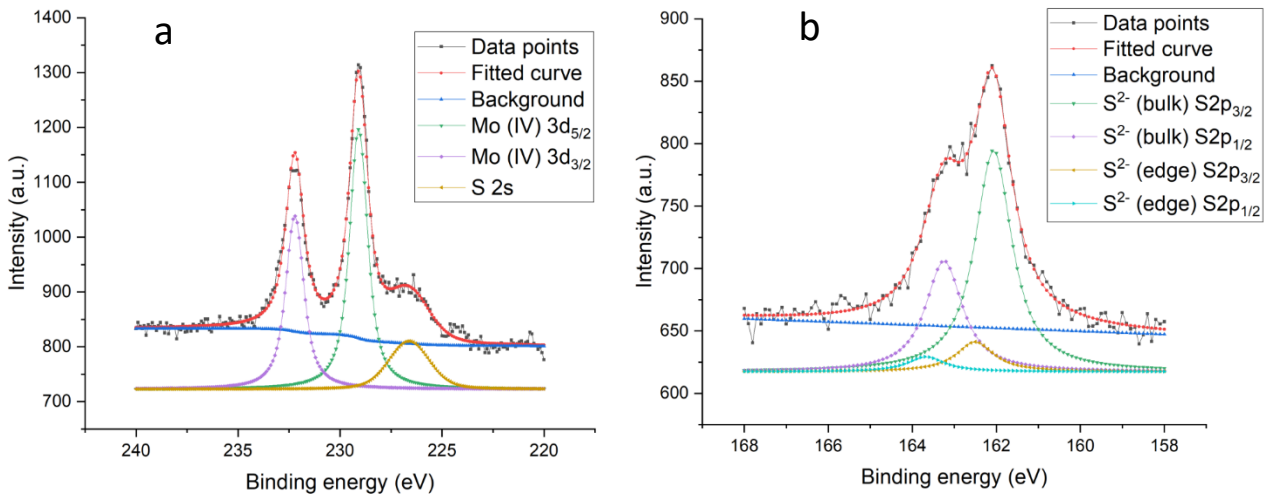

Figure 3.20 - XPS spectra for (a) Mo 3d and (b) S 2p orbitals of the fifth deposition attempt.

In figure 3.10a, the peaks found at 229.1 and 232.2 eV fit the curve, without the need for auxiliary peaks: these peaks correspond to Mo (IV), without other peaks for metallic molybdenum being present. By comparing these spectra with the data reported in the literature, the peaks match very closely those for pure MoS_2.

The sulfur peaks, in figure 3.10a, are found at 226.5 eV for the S 2s orbital, while in figure 3.10b the peaks for S $2p_{3/2}$ and $2p_{1/2}$ are found at 162.1 and 163.3 eV, and at 162.4 and 163.7 eV, also matching those reported in the literature for S^{2-} in the bulk of the lattice and at the edges of the film respectively. [9,10,17,18]

This procedure yielded a layer of pure MoS_2 on the surface of the Au (111) crystal, even though some excess elemental sulfur is present and likely was adsorbed either on the suface of the Au (111) crystal not covered by stoichiometric MoS_2 or even on the MoS_2 layer itself, particularly along the edges.

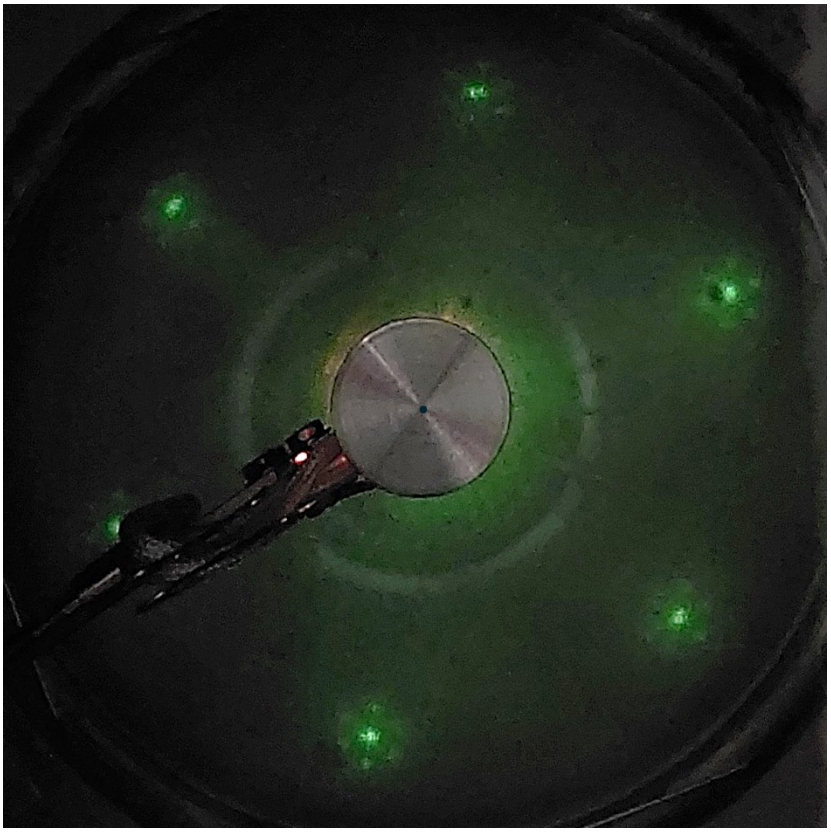

Figure 3.21 - LEED ($I_{filament}$=1.730 A, 80 V) of the pristine MoS_2 fim obtained in the fifth deposition.

The LEED pattern obtained, shown in figure 3.11, is very close to the pattern reported by Bana et al. for pure MoS_2. [13] Around the spots, which correspond to the diffraction points for gold, six other points are visible which can be related to the Moiré superlattice. [13,14] After the deposition, the hexagonal diffraction pattern of Au undergoes a profound modification, and around each first-order diffraction spots, we can identify additional diffraction spots arranged into a hexagon at a distance of 0.781 ± 0.054 $angs^{-1}$ in reciprocal space, which are the distinctive fingerprints of a (10x10) superstructure.

The thin film produced through this deposition procedure presents an excess of sulfur, given the relatively long and repeated exposure to S vapors. However, this proved to be an advantage since in case it is necessary to protect the film from the interaction with the atmosphere. In fact a thin layer of elemental sulfur can prevent the interaction with the gas phase and then can be removed in vacuum simply by annealing. Indeed,

after the prepareation such a layer was deposited on the prepared surface and the sample was taken out of the vacuum and placed in a homemade receptacle.

The receptacle is built out of flanged steel vacuum chamber components (figure 3.12) and fitted with an alumina window and a needle valve. Once the sample is transferred inside, the receptacle can be evacuated to $1x10^{-8}$ torr. The receptacle is sealed by closing the needle valve to allow for sample transportation while maintaining a static vacuum.

Figure 3.22 - Vacuum receptacle to transport the sample of Au (111) with deposited MoS_2. In the picture the receptacle is not yet complete, missing its valve, seen in the top left-hand corner, to seal it once the vacuum has been pulled.

Thanks to the use of the UHV receptacle, the sample was exposed only briefly to air under the protection of the sulfur capping layer, and in total for less than 30 minutes, transitioning from the growing chamber in Padova to the experimental station of the BACH beamline facility at the Elettra Synchrotron radiation facility in Trieste. Moreover, prior to XPS analyses, it underwent annealing at 350°C under ultra-high vacuum (UHV) conditionsto remove the adventitious contaminants and the capping layer of sulfur.

The XPS spectra are registered using a photon energy of 525 eV for the S 2p and Mo 3d photoemission lines, with an overall energy resolution of about 200 meV.

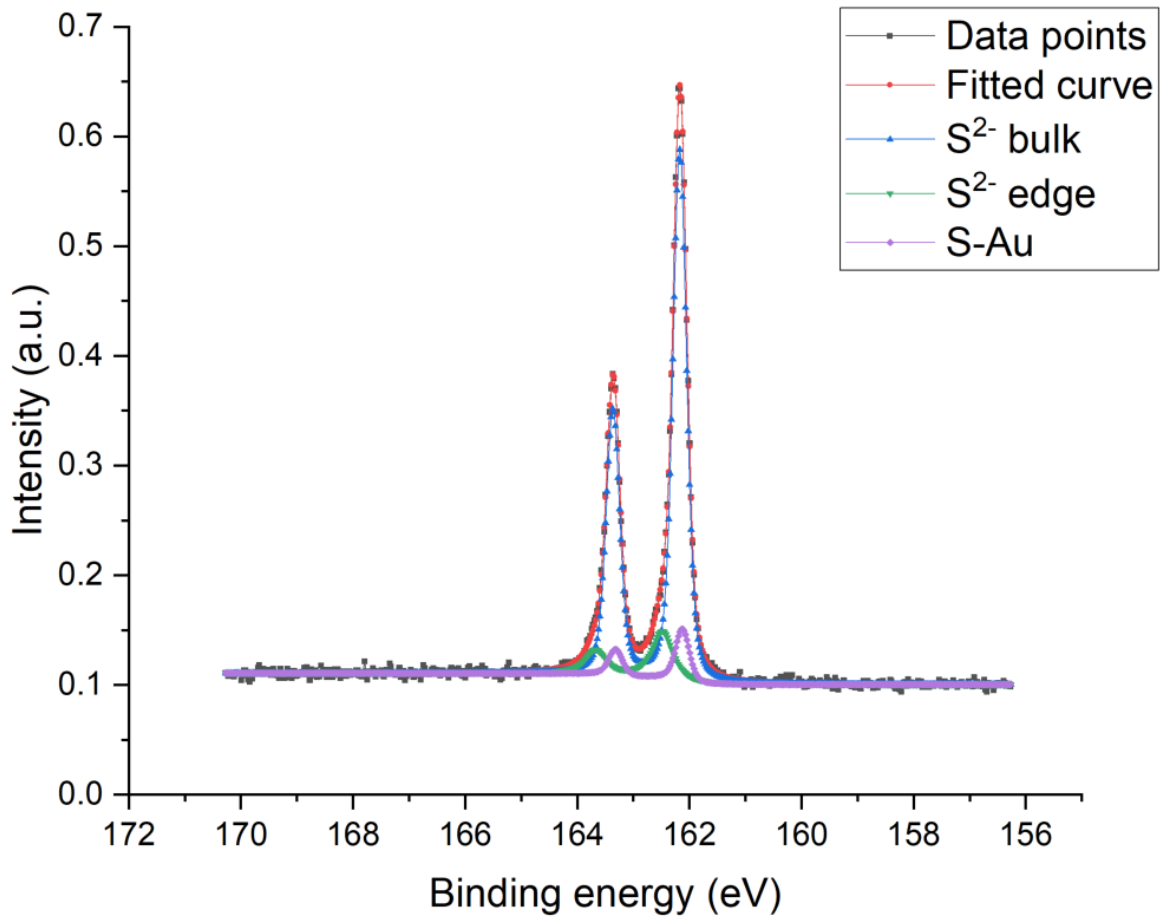

Figure 3.23 - XPS spectrum of the fifth deposition of MoS_2 for the S 2p orbitals, obtained with synchrotron radiation at 525 eV.

The S $2p_{3/2}$ line exhibited two components (figure 3.13): one at 162.2 eV representing the majority component attributed to divalent sulfide ions (S^{2-}), and a minority component at 162.6 eV corresponding to defects created by the fractal edge growth, as observed in figure 3.20a. The shift in binding energy indicates a more positively charged sulfur; however, at the moment it cannot be directly compared to μ-$S2^{2-}$ and/or apical S^{2-}, which should exhibit larger energy shifts. [13,18–21] The curve is fitted with an additional component, attributed to the excess sulfur bonded to the Au substrate. [7]

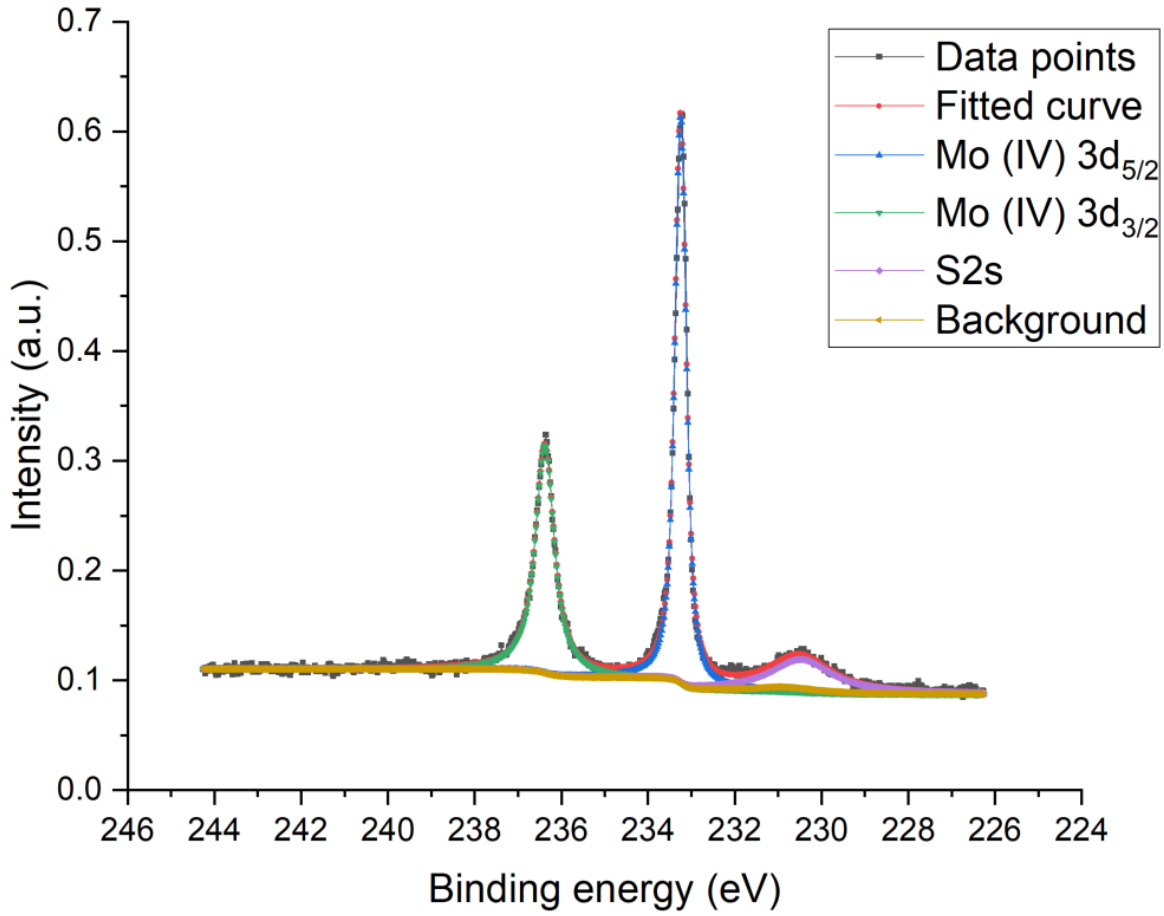

Figure 3.24 - XPS spectrum of the fifth deposition of MoS_2 for the Mo 3d orbitals, obtained with synchrotron radiation at 525 eV.

The Mo 3d spectra (figure 3.14) of the as-prepared samples displayed only one chemical shift component, with Mo $3d_{5/2}$ at 229.2 eV and Mo $3d_{3/2}$ at 232.4 eV related to 2H-MoS_2. To simplify the fitting procedure, the S 2s line was fitted with only one component, focusing our analysis on sulfur's most intense signals, given by the S 2p doublet.

Interestingly, no oxidized Mo and S were detected, indicating the material's resilience to ambient conditions despite being grown with a significant number of fractal edges. The fractal edges formed in the deposition affect only the XPS lines of the sulfur but not the molybdenum. This effect is attributed to the predominant presence of sulfur on the edge with a fully saturated layer, as expected due to the significant excess of sulfur in the growth conditions.

3.1.6 Comparison between the depositions

In figure 3.15 and 3.16 presented the spectra of most of the deposition attempts. The XPS spectra of the first deposition are not depicted for clarity because the lines found are almost exclusively those of the elemental sulfur and metallic molybdenum.

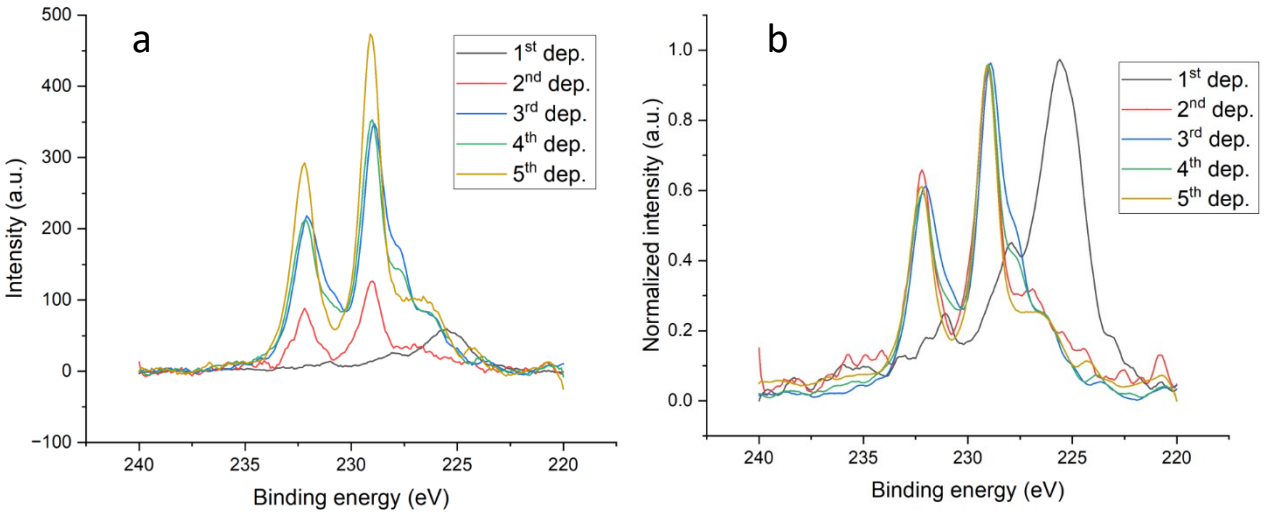

Figure 3.25 – (a) Comparison of the XPS spectra of the Mo 3d for the deposition trials (note that the spectrum of the first deposition is not to scale, and the values have been divided by 10). (b) Comparison of the normalized spectra of the Mo 3d for the deposition trials.

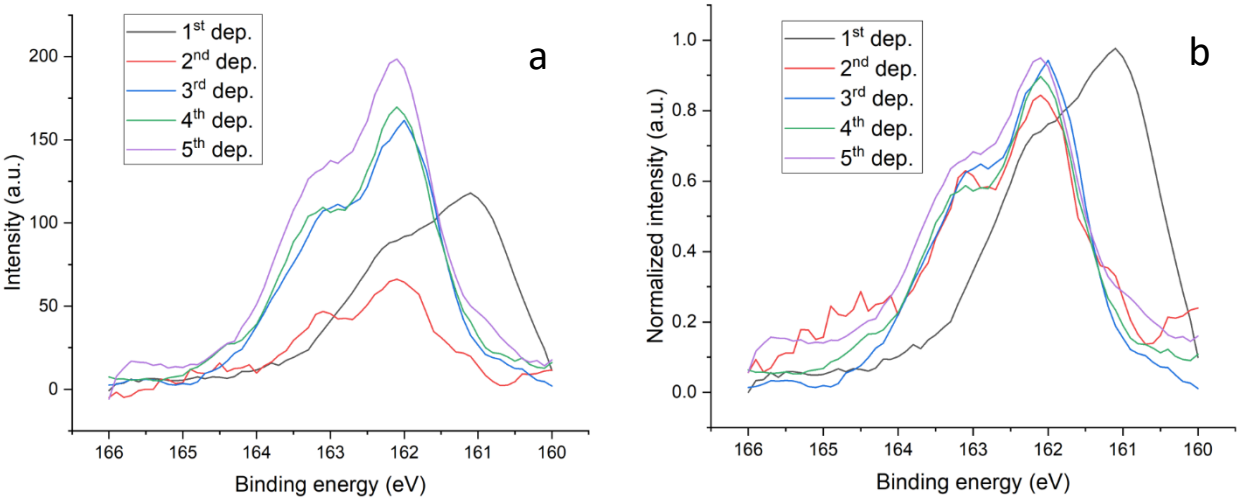

Figure 3.26 - (a) Comparison of the XPS spectra of the S 2p for the deposition trials (note that the spectrum of the first deposition is not to scale, and the values have been divided by 10). (b) Comparison of the normalized spectra of the S2p for the deposition trials.

Table 3.6 - Comparison of the conditions for the five depositions.

	T_d (°C)	T_a (°C)	Voltage of evaporator (V)	Emission current (mA)	Filament current (A)	Mo/S
First deposition	120	400	1.15	70.0	4.5	0.067
Second deposition	400	250	1.10	45.0	7.5	0.320
Third deposition	300	170	1.00	50.0	8.0	1.032
Fourth deposition	450	250	1.00	50.0	8.0	0.442
Fifth deposition	450	250	1.10	40.0	7.8	0.559

With the data presented in table 3.6 it is possible to see how the temperature of the substrate, the Au (111) crystal, is important to drive the reaction between sulfur and molybdenum on the surface. The ratio of molybdenum to sulfur is calculated by using the areas of the peaks determined in the fit procedure of Mo^{4+} and S^{2-} chemically shifted components in the XPS spectra, divided by the relative sensitivity factors: this ratio gives a good approximation of the stoichiometry of the Mo/S material deposited on the surface, although it is imperfect since it takes into account only one component of the sulfur peaks. Also, as previously stated, the deposition occurs in excess of sulfur, and in most XPS spectra it is still possible to see a small signal related to sulfur clusters on the surface of the sample.

3.2 STM of the prepared samples

After characterization with XPS, some of the deposited samples were investigated with a Scanning Tunneling Microscope in Ultra-High Vacuum. In the following we report constant current topographic images acquired at room temperature using a chemically etched tungsten tip mounted on a Kolibri sensor. In general, the tip was sputtered with Ar^+ before image acquisition. In the following sections, the images presented were recorded on the films produced in the second, third and fifth deposition.

3.2.1 Morphology of the MoS_2

As with a typical STM topography, it is possible to recognise quite easily the formation of a monolayer film on the unreconstructed Au (111) terraces. The film morphology consists of large islands of triangular shape (as seen in figure 3.17) that are compact and continuous in their center whereas towards the periphery can show some holes, eventually forming interconnected meandering trenches.

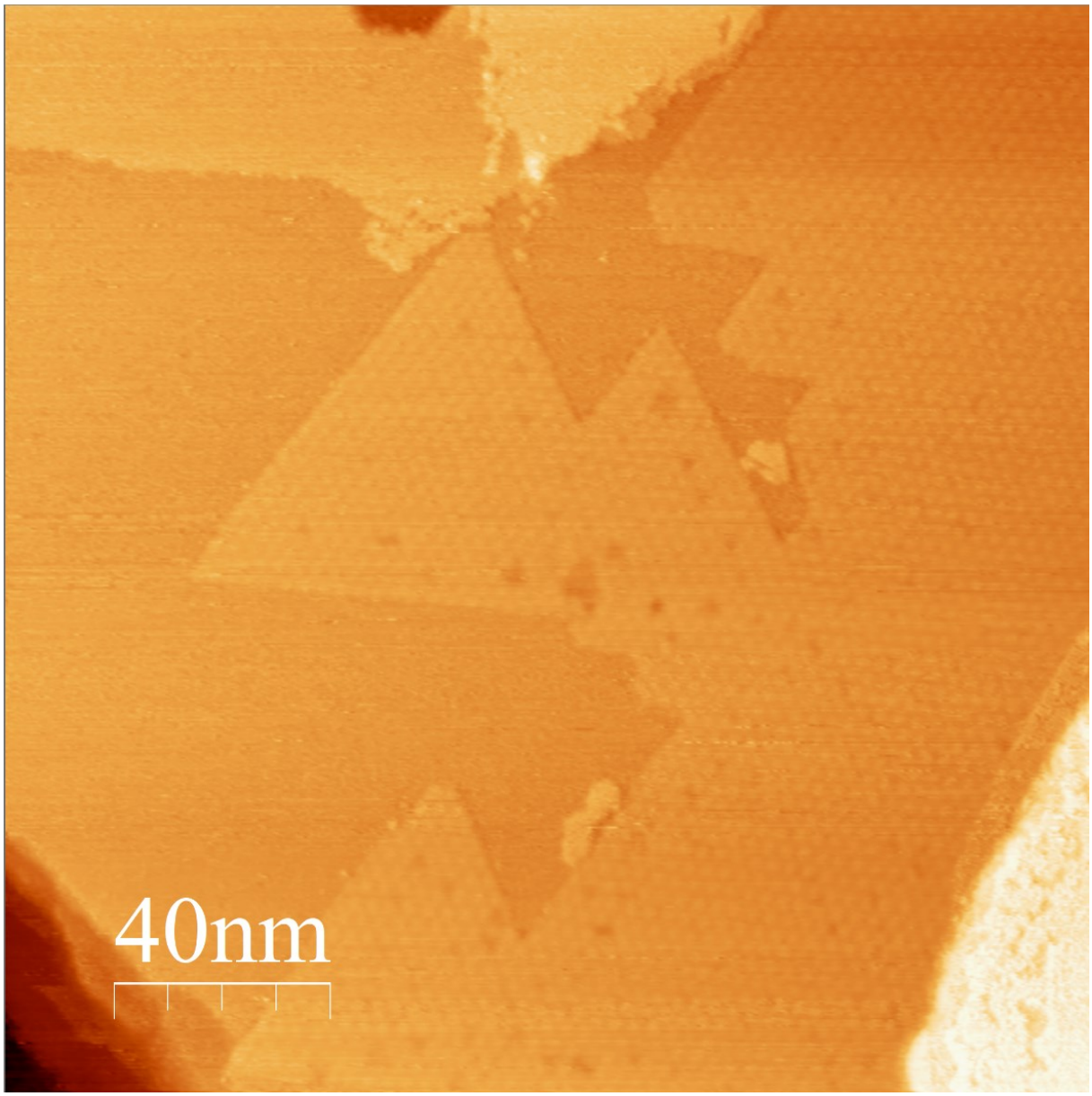

Figure 3.27 - (I=1.0 nA, V=1.0 V, 200x200 nm) Layer of MoS_2 on the surface of the Au (111) crystal from the second deposition, showing extended triangular islands.

The images in figures 3.17 and 3.18 show the morphology of the sample obtained in the second deposition, in which a film of MoS2 was produced, even though the results were unsatisfactory as seen from the photoemission spectra. In particular the film shown in figure 3.17 does not cover large portions of the Au substrate and presents several terraces covered with disordered material or sulfur adsorbed on the Au crystal. Where the film is present, however, it has the expected characteristic of the desired MoS_2, confirming the results obtained from the XPS spectra. The larger islands present periodical modulation of the corrugation that produces a hexagonal moiré pattern (figure 3.18). This is well in agreement with previous data [13,22] reporting that MoS_2 form (10x10) epitaxial superstructure on the Au (111), confirming what was previously found through LEED measurements.

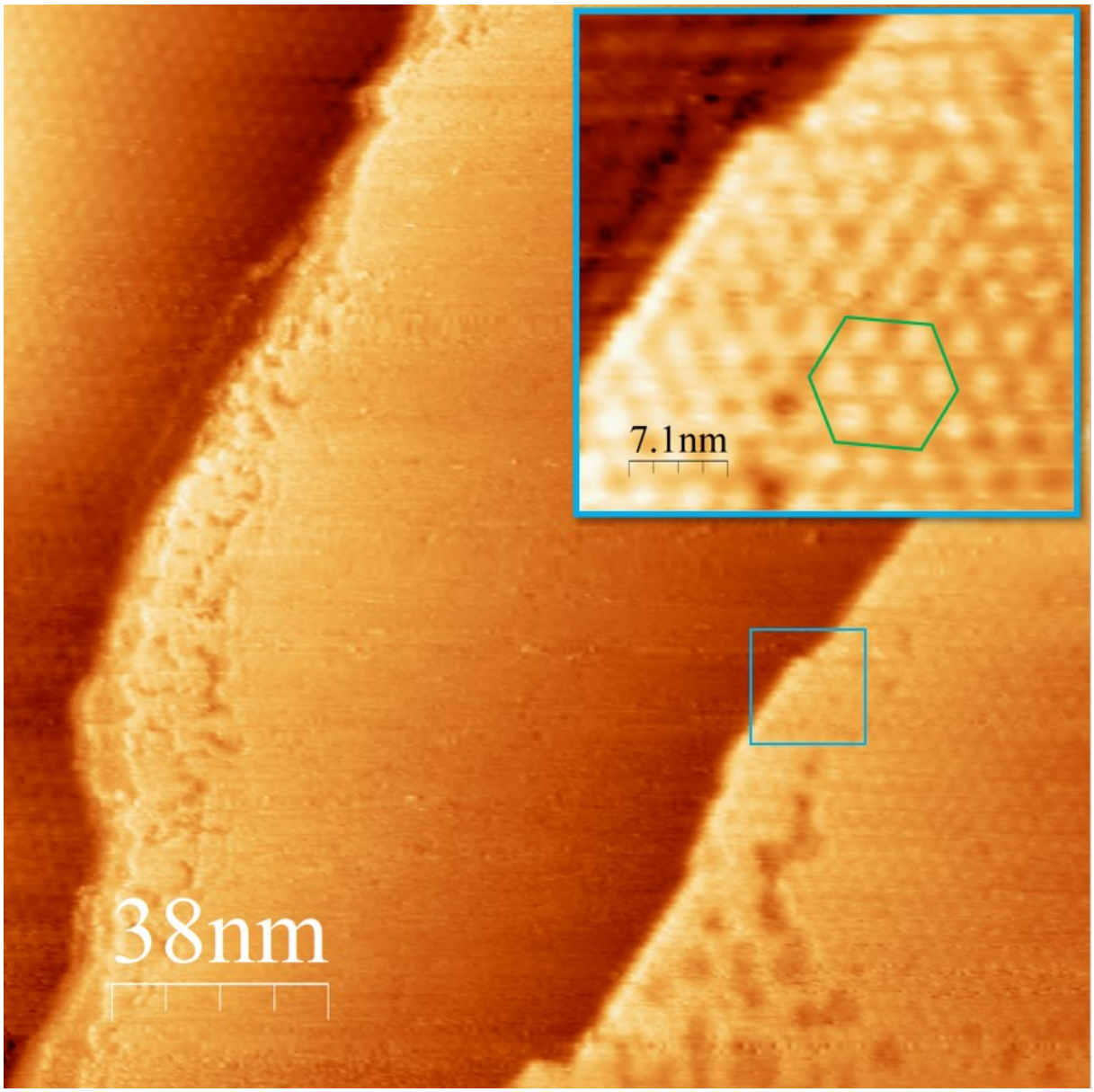

Figure 3.28 - (I=1.0 nA, V=1.0 V) (a) Terraces that exhibit the characteristic Moiré pattern of MoS_2 (190x190 nm, left), formed in the second deposition, and a zoom (b, highlighted by blue box) on a terrace covered in MoS_2 that shows the characteristic Moiré pattern (highlighted with the green hexagon) in more detail (35x35 nm).

In the third deposition the film, consistently with what was found in the photoemission spectra, appears to be disordered and presents several triangular islands, that accumulate alongside the step-edge but are otherwise randomly distributed on the surface. The growth of the triangular islands occurs in two possible orientations, which are rotated in respect to each other by 180°, as can be seen in figure 3.19.

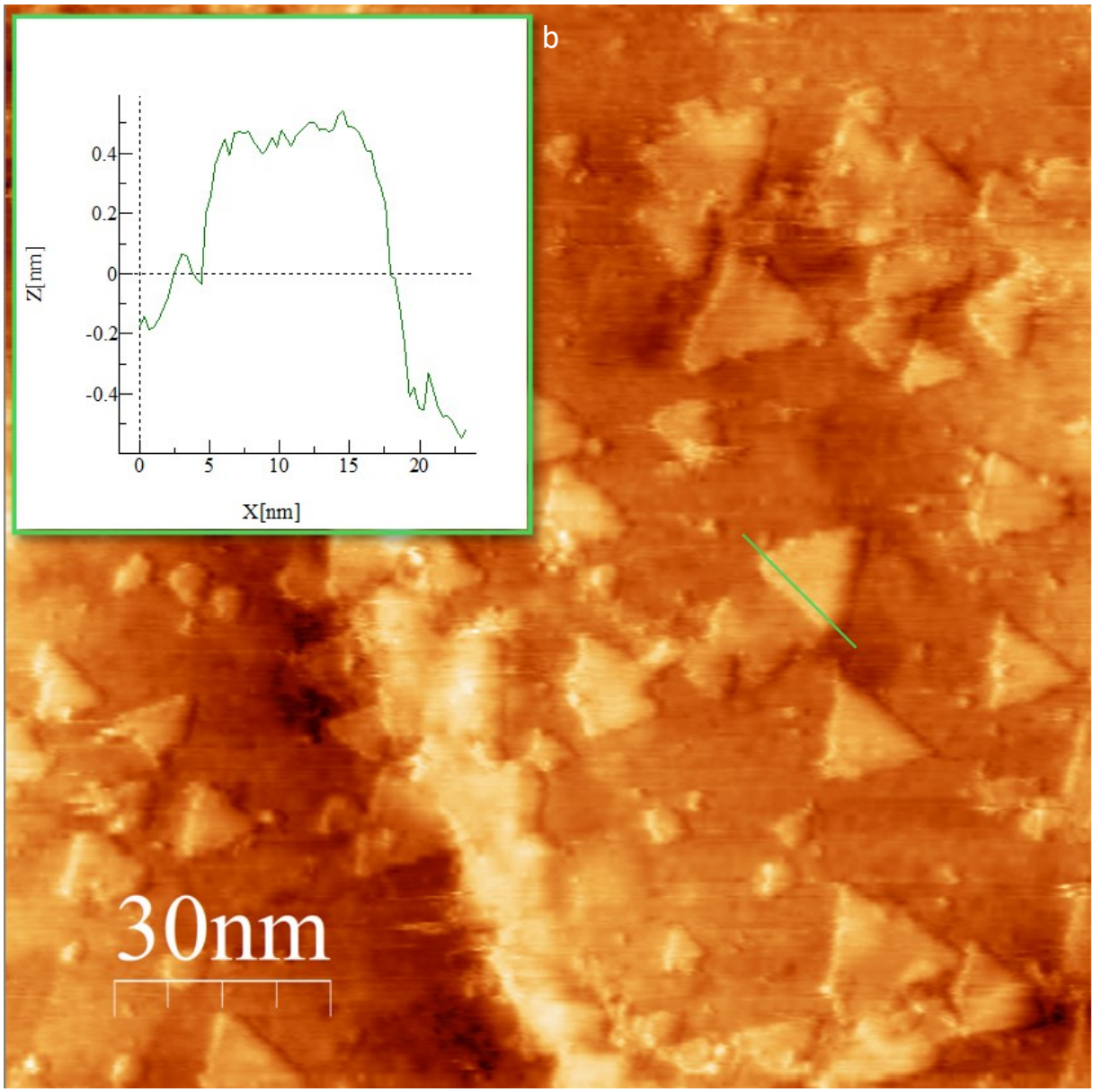

Figure 3.29 - (I= 1.0 nA, V = 1.5 V, 150x150 nm) A step edge that shows the accumulation of triangular islands of MoS_2; inset shows the rough dimensions of one of the islands from a line profile.

From figure 3.19 it can be observed that the MoS_2 forms new islands on previously completely formed layers of material, suggesting a Stranski-Krastanow type growth. These islands cover, on average, about 20% of the surface and have an average size between 13 and 19 nm. The triangular shaped holes and junction lines, as seen in figure 3.20 suggest the migration and coalescence of already formed triangular islands to form larger islands and terraces. [22]

The fifth deposition was the most successful and resulted in a pure, ordered film of MoS2, as was observed from the LEED and XPS measurements. The following images were all recorded on the film obtained in this deposition.

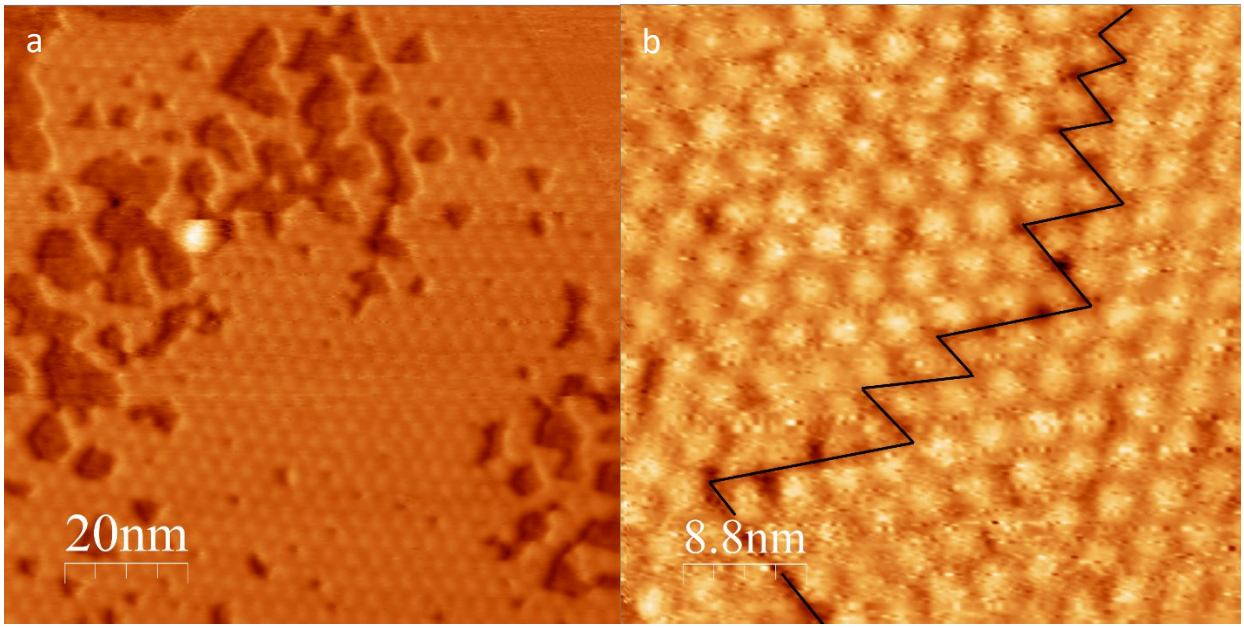

Figure 3.30 – (I=1.0 nA, V=1.0 V, 100x100 nm) (a) Layer of material that displays both Moiré pattern and triangular holes. (I=1.0 nA, V=0.2 V, 44x44 nm) (b) Junction, marked by a black line, found in the Moiré pattern on a layer of MoS_2 formed in the fifth deposition.

3.2.2 Moiré pattern

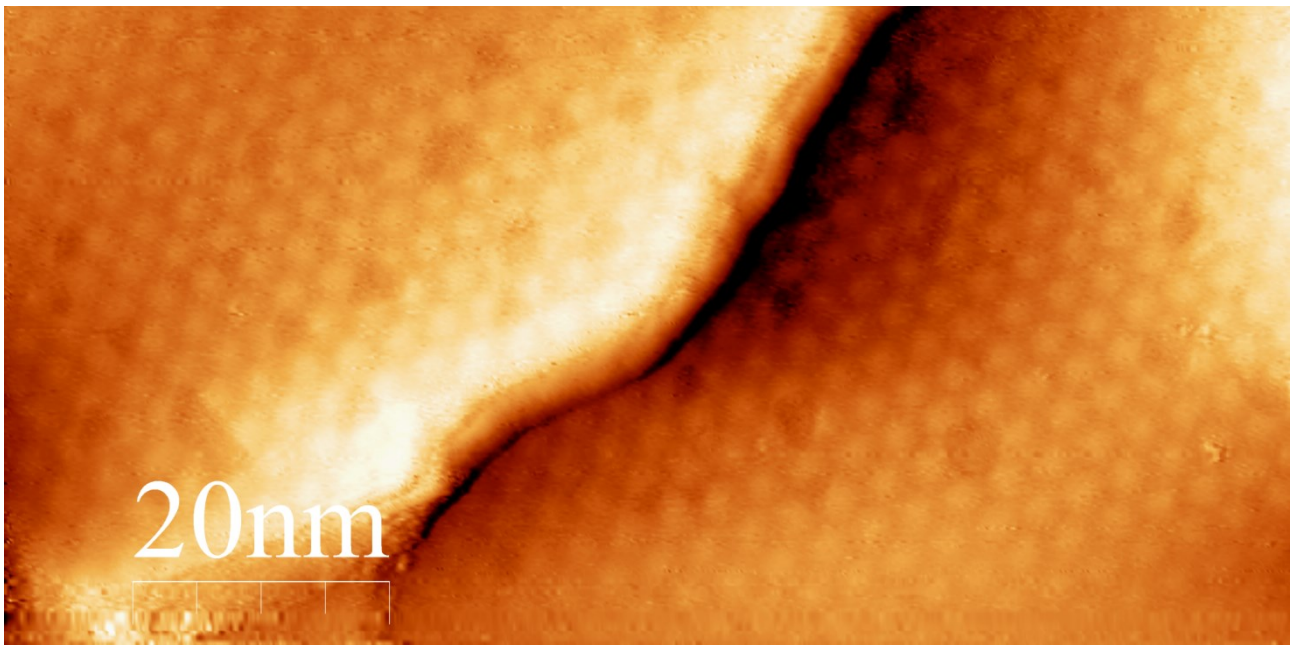

Figure 3.31 - (I=0.3 nA, V=1.0 V, 100x50 nm) Two terraces covered with the MoS2 film, separated by a step edge. Especially near the step edge of the upper (left) terrace and in some points of the lower (right) terrace, it is possible to see holes in the Moiré pattern, which correspond to vacancies left from the coalescence of the triangular islands in the formation of the film.

Moiré patterns may be observed whenever two patterns differ slightly, such as in the case of two overlapping layers of atoms. The pattern is observed because of lattice mismatch or presence of a twist angle between the structures of the overlayer and substrate. Although it is not an exact model, since it does not take into account wave decay effects that occur at this scale, [23] the usual explanation for Moiré patterns is the Simple Superposition Model (SSM). In this model the Local Density of States (LDOS) is affected by the mismatch in periodicity between substrate and overlayer, which gives either constructive or desctructive interference. The resulting effect is the periodic modulation of the topographic height that is now convoluted with the variation of the electronic structure. [24] In the SSM the layers are defined by their respective basis vectors (rigid layers) and the overlayer can shift with respect to the underlayer without affecting the periodicity and angle of fringes of the Moiré pattern. [23,24]

The observed Moiré pattern (figure 3.21) is the results of the overlap between the Au (111) lattice with 0.288 nm spacing and the 2H-MoS_2 with 0.316 nm and it was measured to have an average pitch of 3.23 nm ±0.05 (measured over 5 images), with the material covering on average 65% of the surface. Moreover, from the coverage measurements it is possible to calculate that the evaporator, combined with the flow of S vapor, deposits on average 0.026 ML/min.

The average periodicity of the Moiré patten is slightly different that the one reported in literature of 3.33 nm, [14,24] however this discrepancy can be attributed to the distortions in the pattern given by incomplete coalescence of the islands to from the MoS_2 layer and possible junctions in the film.

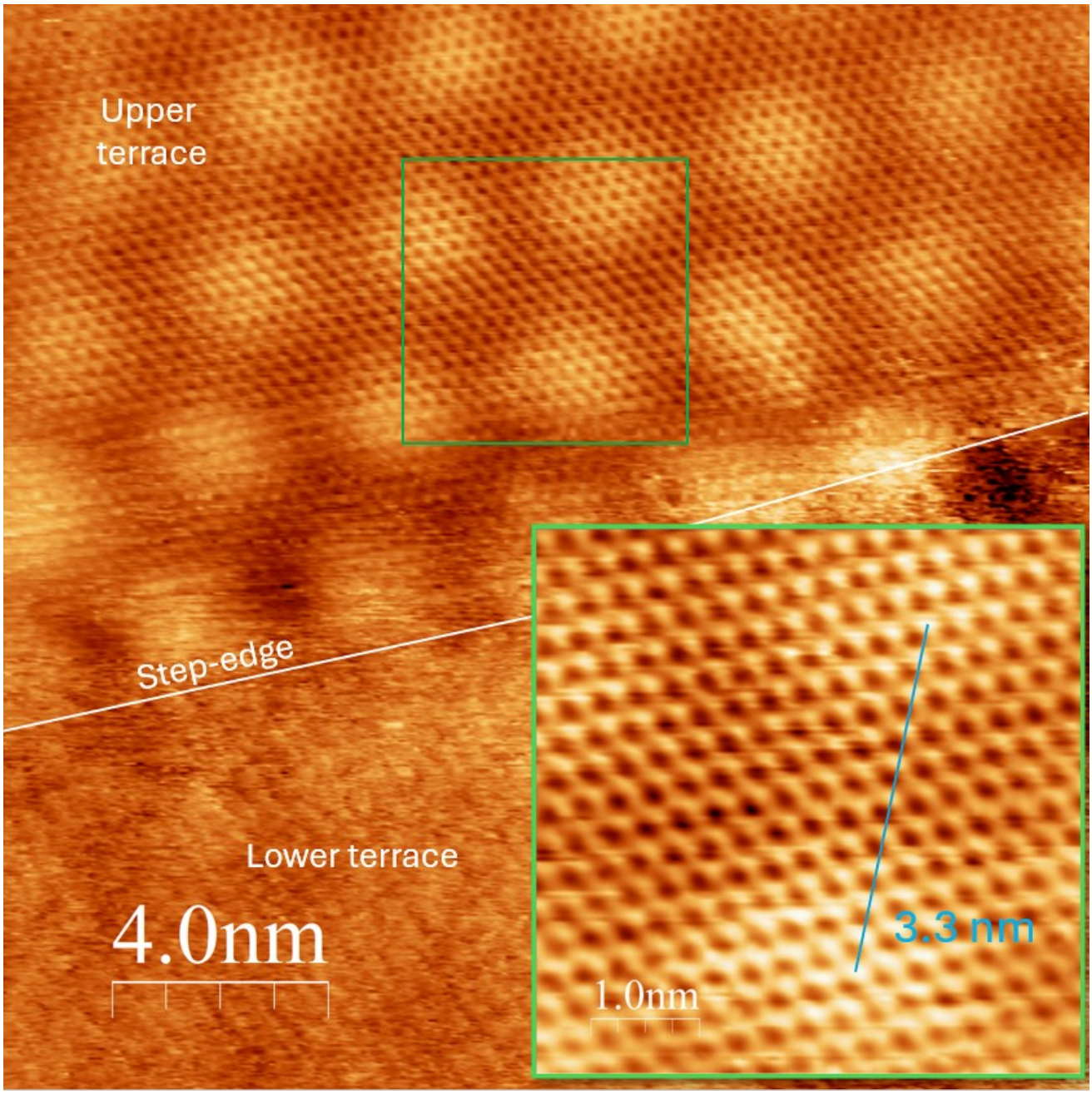

Figure 3.32 - (I=1.0 nA, V=1.0 V) Moiré and atomic resolution image near multiple steps, formed in the fourth deposition (100x100 nm); on the step adjecent to the terrace that shows the Moiré pattern it is possible to faintly see the reconstruction given by sulfur deposited gold. In the inset (5x5 nm) is shown a zoom on the terrace, with the distance between centers of the Moiré pattern highlighted with a blue line.

3.2.3 Atomic resolution images

As shown in figure 3.22 and in figure 3.23, it was possible to achieve atomic resolution for some of the images.

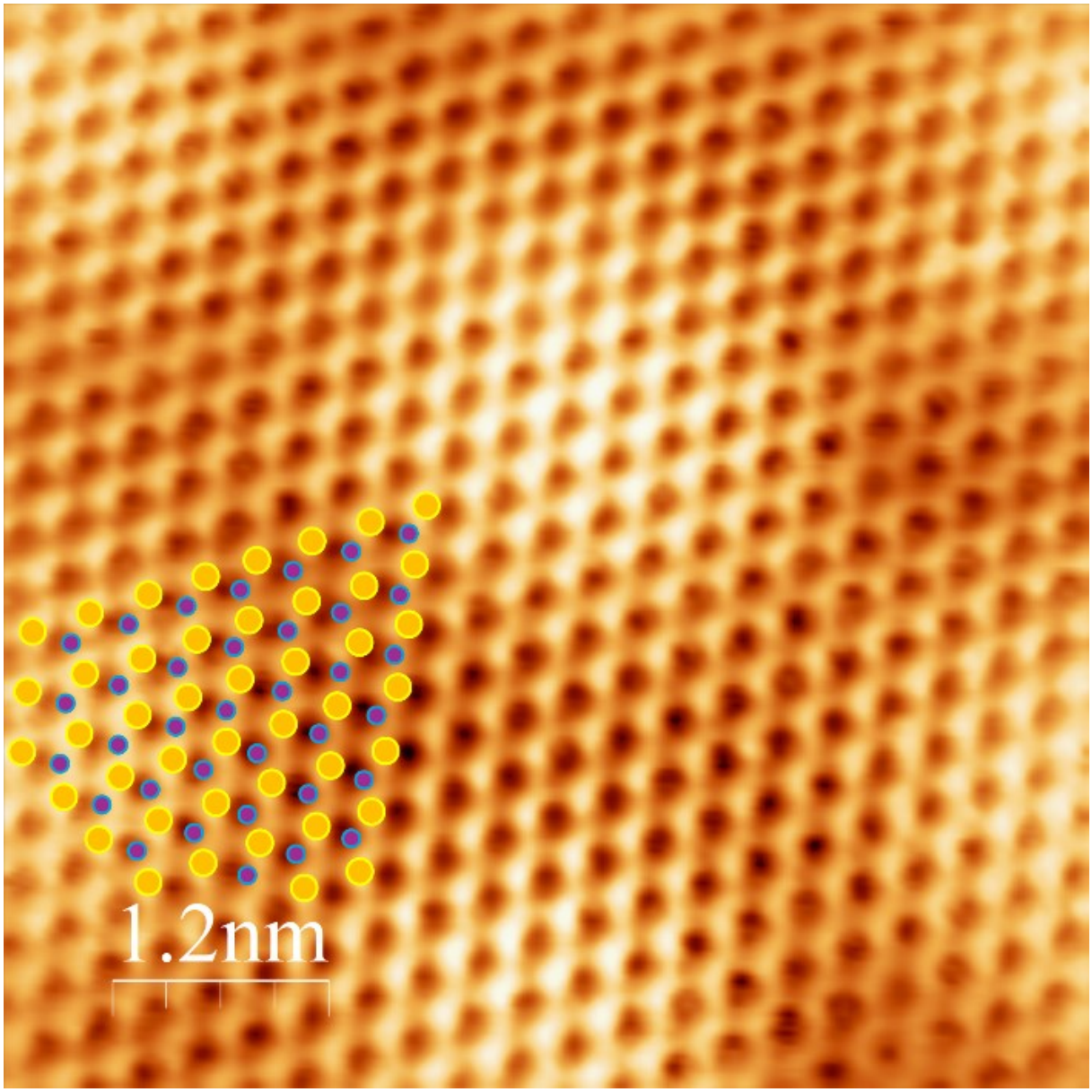

Figure 3.33 - (I=1.0 nA, V=0.1 V, 8x8 nm) Atomic resolution image of the MoS_2 layer produced in the fourth deposition; shown with yellow and purple dots, representing sulfur and molybdenum respectively, is a schematic view of the MoS_2 mesh.

The atoms visible in the images obtained appear to be the topmost sulfur atoms of the sandwich-like structure of the MoS_2 monolayer. In figure 3.24, which shows a a hole in the MoS_2 mesh, it is possible to see sulfur atoms at the edge of the hole, as expected from the heavily sulfurization of the material. [24–26] The average distance between atomic centers is measured to be 0.319 nm ± 0.03 (measured over 4 images), which corresponds to the value reported in the literature. [13,22,27] From the atomic resolution images, it is possible to see that the MoS_2 deposited on the surface is formed in the 1H phase. [28]

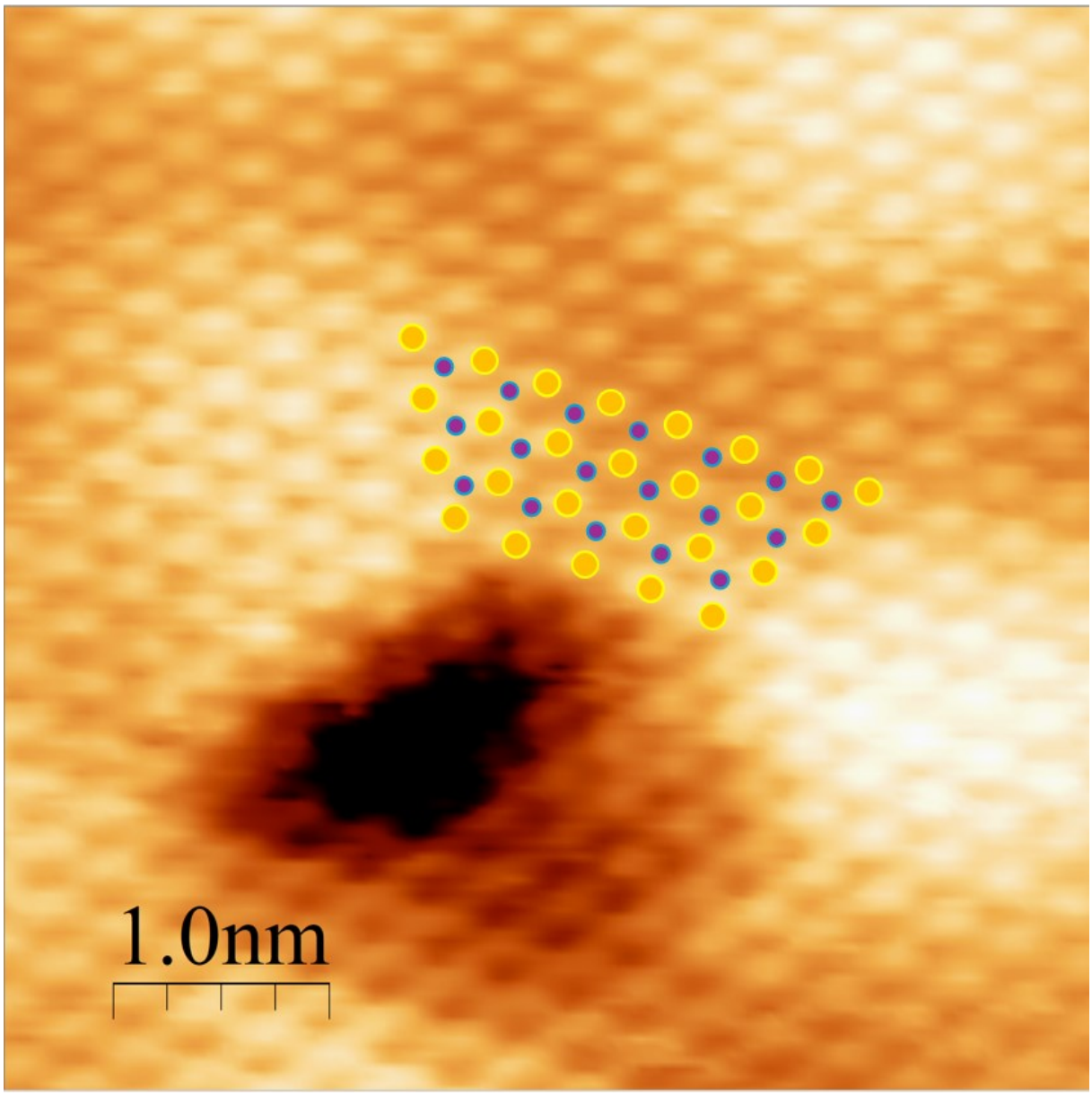

Figure 3.34 - (I=1.1 nA, V=0.3 V, 5x5 nm) Atomic resolution image of the MoS_2 layer produced in the fifth deposition with a clearly visible hole in the film. The MoS_2 mesh is shown again for clarity.

Bibliography for Chapter 3

1. Cattelan, M. *et al.* New Strategy for the Growth of Complex Heterostructures Based on Different 2D Materials. *Chem. Mater.* **27**, 4105–4113 (2015).
2. do Amaral, G. M. *et al.* Epitaxial growth, electronic hybridization and stability under oxidation of monolayer *MoS*2 on Ag(1 1 1). *Appl. Surf. Sci.* **538**, 148138 (2021).
3. Salazar, N., Beinik, I. & V. Lauritsen, J. Single-layer MoS 2 formation by sulfidation of molybdenum oxides in different oxidation states on Au(111). *Phys. Chem. Chem. Phys.* **19**, 14020–14029 (2017).
4. Li, X. *et al.* Pseudo metallic (1T) molybdenum disulfide for efficient photo/electrocatalytic water splitting. *Appl. Catal. B Environ.* **307**, 121156 (2022).
5. Molybdenum | XPS Periodic Table - IT. https://www.thermofisher.com/uk/en/home/materials-science/learning-center/periodic-table/transition-metal/molybdenum.html.
6. Mikhlin, Yu. *et al.* XAS and XPS examination of the Au–S nanostructures produced via the reduction of aqueous gold(III) by sulfide ions. *J. Electron Spectrosc. Relat. Phenom.* **177**, 24–29 (2010).
7. Bourg, M.-C., Badia, A. & Lennox, R. B. Gold−Sulfur Bonding in 2D and 3D Self-Assembled Monolayers: XPS Characterization. *J. Phys. Chem. B* **104**, 6562–6567 (2000).
8. Rodriguez, J. A. *et al.* Coverage Effects and the Nature of the Metal−Sulfur Bond in S/Au(111): High-Resolution Photoemission and Density-Functional Studies. *J. Am. Chem. Soc.* **125**, 276–285 (2003).
9. Syari'ati, A. *et al.* Photoemission spectroscopy study of structural defects in molybdenum disulfide (MoS $_2$) grown by chemical vapor deposition (CVD). *Chem. Commun.* **55**, 10384–10387 (2019).
10. Brown, N. M. D., Cui, N. & McKinley, A. An XPS study of the surface modification of natural MoS2 following treatment in an RF-oxygen plasma. *Appl. Surf. Sci.* **134**, 11–21 (1998).
11. Chen, P. *et al.* Thermal Degradation of Monolayer MoS2 on SrTiO3 Supports. *J. Phys. Chem. C* **123**, 3876–3885 (2019).
12. Chang, K. *et al.* Targeted Synthesis of 2H- and 1T-Phase MoS2 Monolayers for Catalytic Hydrogen Evolution. *Adv. Mater.* **28**, 10033–10041 (2016).

13. Bana, H. *et al.* Epitaxial growth of single-orientation high-quality MoS2 monolayers. *2D Mater.* **5**, 035012 (2018).
14. Grønborg, S. S. *et al.* Synthesis of Epitaxial Single-Layer MoS2 on Au(111). *Langmuir* **31**, 9700–9706 (2015).
15. Yang, Y. W. & Fan, L. J. High-Resolution XPS Study of Decanethiol on Au(111): Single Sulfur−Gold Bonding Interaction. *Langmuir* **18**, 1157–1164 (2002).
16. Lince, J. R. *et al.* Photoelectron spectroscopic study of the interaction of thin Fe films with the MoS2(0001) surface. *Surf. Sci.* **223**, 65–81 (1989).
17. Wang, H. W., Skeldon, P. & Thompson, G. E. XPS studies of MoS2 formation from ammonium tetrathiomolybdate solutions. *Surf. Coat. Technol.* **91**, 200–207 (1997).
18. Didziulis, S. V., Lince, J. R., Shuh, D. K., Durbin, T. D. & Yarmoff, J. A. Photoelectron spectroscopy of MoS2 at the sulfur 2p absorption edge. *J. Electron Spectrosc. Relat. Phenom.* **60**, 175–192 (1992).
19. Favaro, M. *et al.* In Situ Study of Graphene Oxide Quantum Dot-MoSx Nanohybrids as Hydrogen Evolution Catalysts. *Surfaces* **3**, 225–236 (2020).
20. Casalongue, H. G. S. *et al.* Operando Characterization of an Amorphous Molybdenum Sulfide Nanoparticle Catalyst during the Hydrogen Evolution Reaction. *J. Phys. Chem. C* **118**, 29252–29259 (2014).
21. Tran, P. D. *et al.* Coordination polymer structure and revisited hydrogen evolution catalytic mechanism for amorphous molybdenum sulfide. *Nat. Mater.* **15**, 640–646 (2016).
22. Li, J. *et al.* Single-Crystal MoS2 Monolayer Wafer Grown on Au (111) Film Substrates. *Small* **17**, 2100743 (2021).
23. Kobayashi, K. Moir\'e pattern in scanning tunneling microscopy: Mechanism in observation of subsurface nanostructures. *Phys. Rev. B* **53**, 11091–11099 (1996).
24. Krane, N., Lotze, C. & Franke, K. J. Moiré structure of MoS2 on Au(111): Local structural and electronic properties. *Surf. Sci.* **678**, 136–142 (2018).

25. Davelou, D., Kopidakis, G., Kioseoglou, G. & Remediakis, I. N. MoS2 nanostructures: Semiconductors with metallic edges. *Solid State Commun.* **192**, 42–46 (2014).
26. Hosoki, S., Hosaka, S. & Hasegawa, T. Surface modification of MoS2 using an STM. *Appl. Surf. Sci.* **60–61**, 643–647 (1992).
27. He, Z. & Que, W. Molybdenum disulfide nanomaterials: Structures, properties, synthesis and recent progress on hydrogen evolution reaction. *Appl. Mater. Today* **3**, 23–56 (2016).
28. Wu, F. *et al.* Formation of Coherent 1H–1T Heterostructures in Single-Layer MoS2 on Au(111). *ACS Nano* **14**, 16939–16950 (2020).

Chapter 4 – Iron doping

In this work, we wanted to find a method to obtain thin films of MoS_2 modified by the incorporation into the lattice of atoms of other elements. In chapter 3 the deposition attempts alway result in a 1H-MoS_2 surface and as stated in chapter 1, this phase is less active than the metallic 1T phase of MoS_2. Yu et al. report that a possible way to give the 1H-MoS2 a quasi-1T structure is the incorporation of Fe atoms in the lattice, by creating a structure resembling a distorted 1T-MoS_2 phase and resulting in a modification of the material's electronic structure. [1] Other authors on the other hand, supported the idea that atomically disperse Fe atoms into the MoS_2 lattice represent catalytic centers with a very favorable hydrogen adsorption energy and therefore potentially possess a high chemical activity for the Hydrogen Evolution Reaction. [2–4]

Note that the spectra of Fe will report only the $2p_{3/2}$ spin-orbit peak, in order to make them more easily readable.

4.1 Direct Iron Deposition

Initially, the surface modification of the MoS_2 surface is attempted by direct iron deposition on the surface of the material at room temperature, while under UHV.

First, a clean surface of MoS_2 is prepared following the procedure described in chapter 3 for the final deposition attempt. Figure 4.1 reports the XPS spectra obtained for this prepared surface.

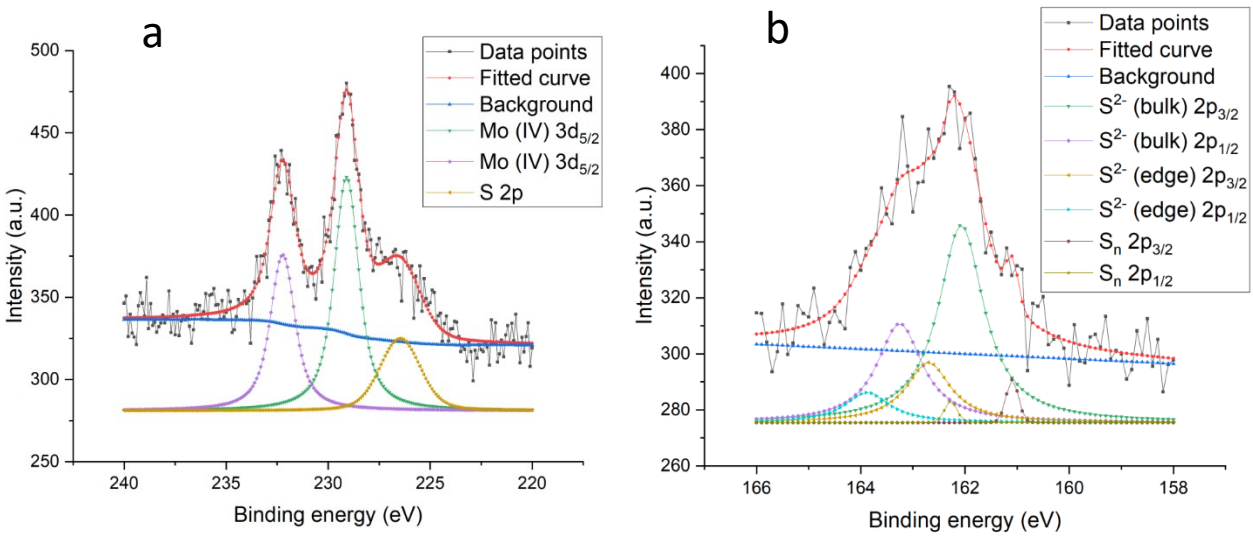

Figure 4.35 - XPS spectra of Mo 3d and S 2p of the prepared MoS_2 surface before the deposition.

The spectra in figure 4.1 are very similar to the spectra of pure MoS_2, already discussed in chapter 3.

The deposition of iron on the prepared MoS_2 surface is done though the use of a second electron beam evaporator, loaded with a Fe rod, opening its shutter for 10 minutes. The operating conditions set for the Fe

evaporator are: applied bias of 0.8 kV, emission current of 8 mA, and filament current of 2.7 A, i.e. with a power of 6.4 W directly through the metal rod.

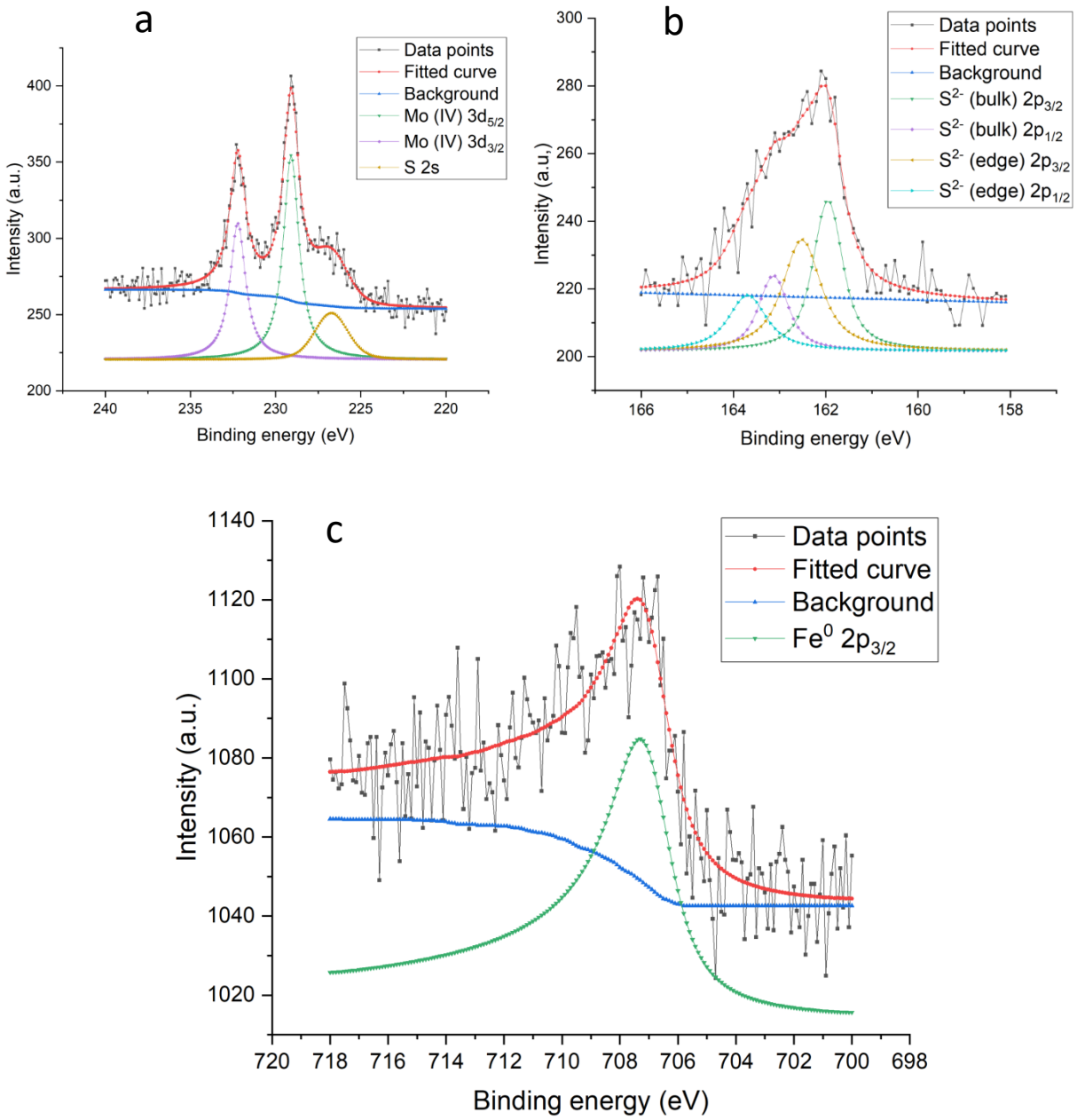

Figure 4.36 - XPS Mo 3d, S 2p and Fe 2p spectra of the MoS_2 surface after the Fe deposition.

In figure 4.2c, the peak of Fe 2p is found at BE of 707.0 eV, likely only in its metallic form [5–7] because during the deposition on the MoS_2 surface the sample was not given energy to activate a reaction to incorporate it inside the host lattice. The asymmetry in the line shape is often observed often in the 2p spectra of first-row transition metals and is an effect given by the unequal exchange interaction between electrons with parallel and anti-parallel spin.

While the exchange interaction is balanced between closed shells, it is not for interactions between core and unpaired electrons, resulting in a slight spatial displacement between the parallel and anti-parallel spin wave functions of core electrons. [8,9] It has to be noted that the Mo 3d and S 2p spectra, in figure 4.2, are not modified significantly from the addition of Fe on the surface of the film.

The LEED of the sample, shown in figure 4.3, before and after the deposition of Fe doesn't show any new reflections in the pattern, with the only difference between the two being that the points appear slightly blurrier after the deposition.

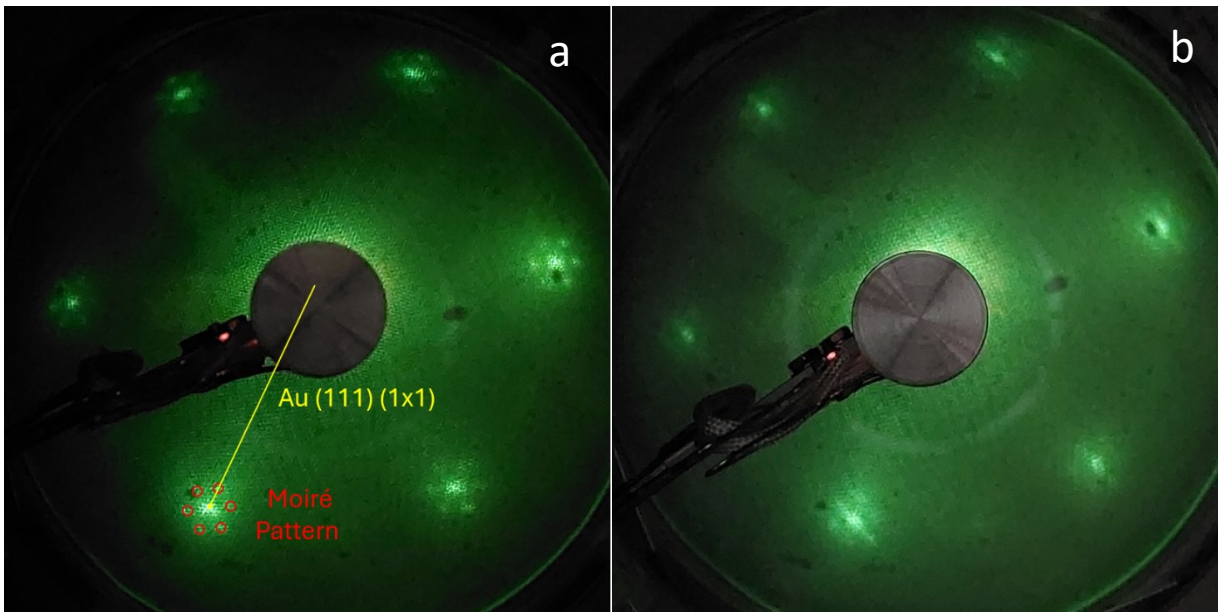

Figure 4.37 - Leed patterns before (a) and after (b) the deposition of Fe on the prepared MoS_2 sample.

While from a comparison of LEED patterns obtained, shown in figure 4.3, no appreciable difference is observed in the patterns before and after the deposition of Fe, through STM imaging it is possible to observe nanoparticles deposited on the surface of the sample (figure 4.4). These nanoparticles are likely metallic Fe, which, in contrast to the Stranski-Krastanov type growth of MoS_2, seems to form clusters and single particles adopting a Volmer-Weber type growth.

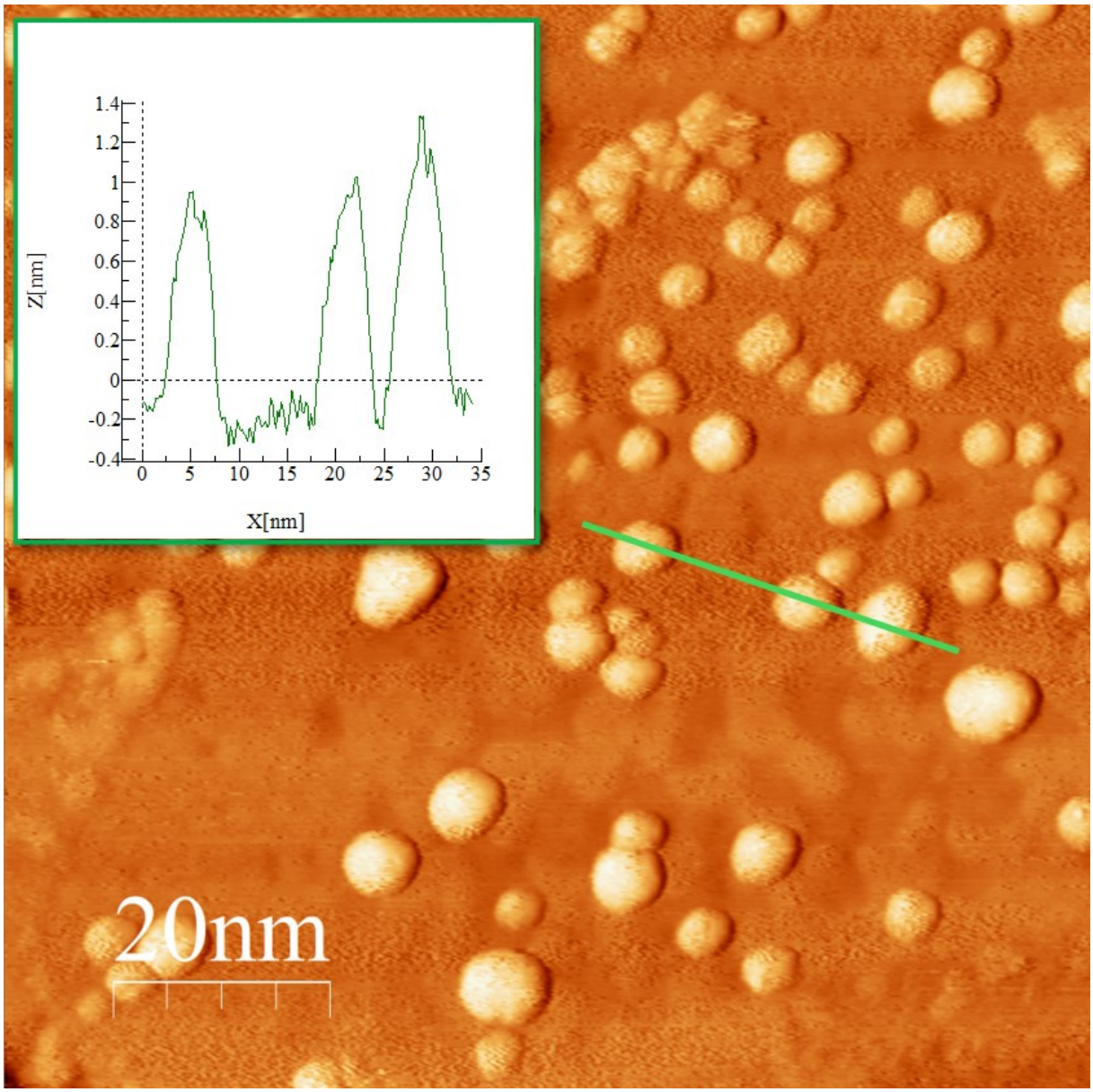

Figure 4.38 – (I=0.7 nA, V=0.9 V, 100x100 nm) Image of a flat MoS_2 surface, that presents some holes, with Fe nanoparticles distributed on the surface (the inset displays a line profile to show the height and diameter of the average NPs).

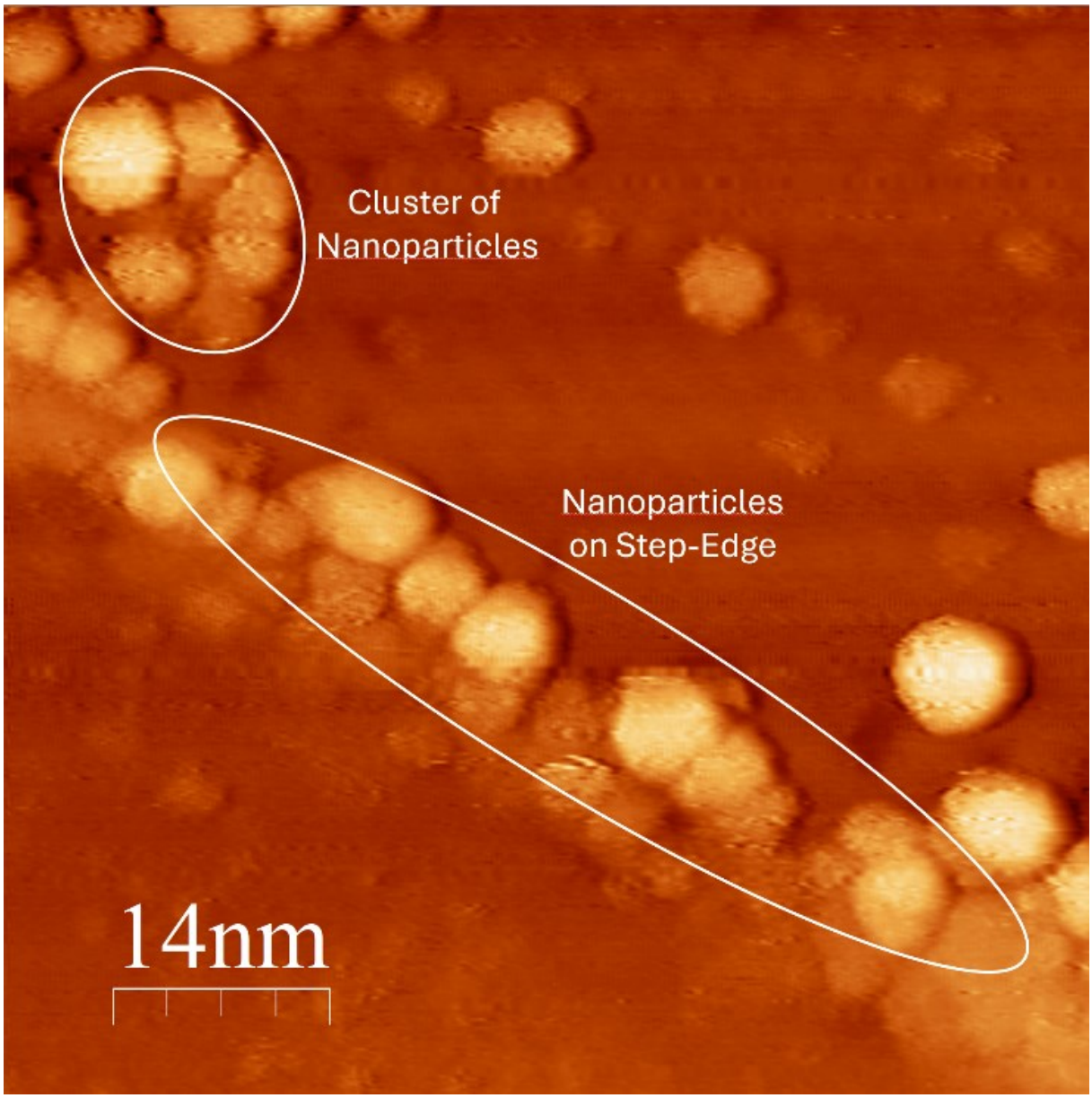

Figure 4.39 - (I=1.0 nA, V=0.6 V, 70x70 nm) Clusters of Fe nanoparticles located along a MoS2 step-edge.

The Fe nanoparticles on the surface have an average diameter of 4.98 nm ±1.02 and an average height of 1.37 nm ±0.22 (calculated over 5 images) and are located preferentially over some of the holes of the Moirè pattern, or along step-edges. These nanoparticles cover about 10% of the surface of the sample.

The sample is annealed twice at progressively higher temperatures, under a flow of sulfur vapors. These annealing cycles are attempts at modifying the deposited material either by direct sulfurization of the iron or by incorporation of the latter inside the lattice of the already present MoS_2.

The first annealing of the sample is performed by heating the sample for 30 minutes at 150 °C under a continuous flow of sulfur gas; the pressure in the preparation chamber reached 3.4×10^{-8} torr. The sulfur dosing is shut off and the sample is then cooled to room temperature.

The second annealing is perfomed in two steps: at first the sample is brought to 150 °C and kept at this temperature for 5 minutes, then the sulfur vapor is dosed in the preparation chamber, reaching the pressure of 4.2×10^{-8} torr. The temperature of the sample is raised and kept at 450 °C for 20 minutes, then the sulfur vapor is shut off and the sample is cooled at room temperature.

The cycles of annealing did not appreciably modify the XPS spectra and because of this only the spectra measured after the second annealing cycle are reported.

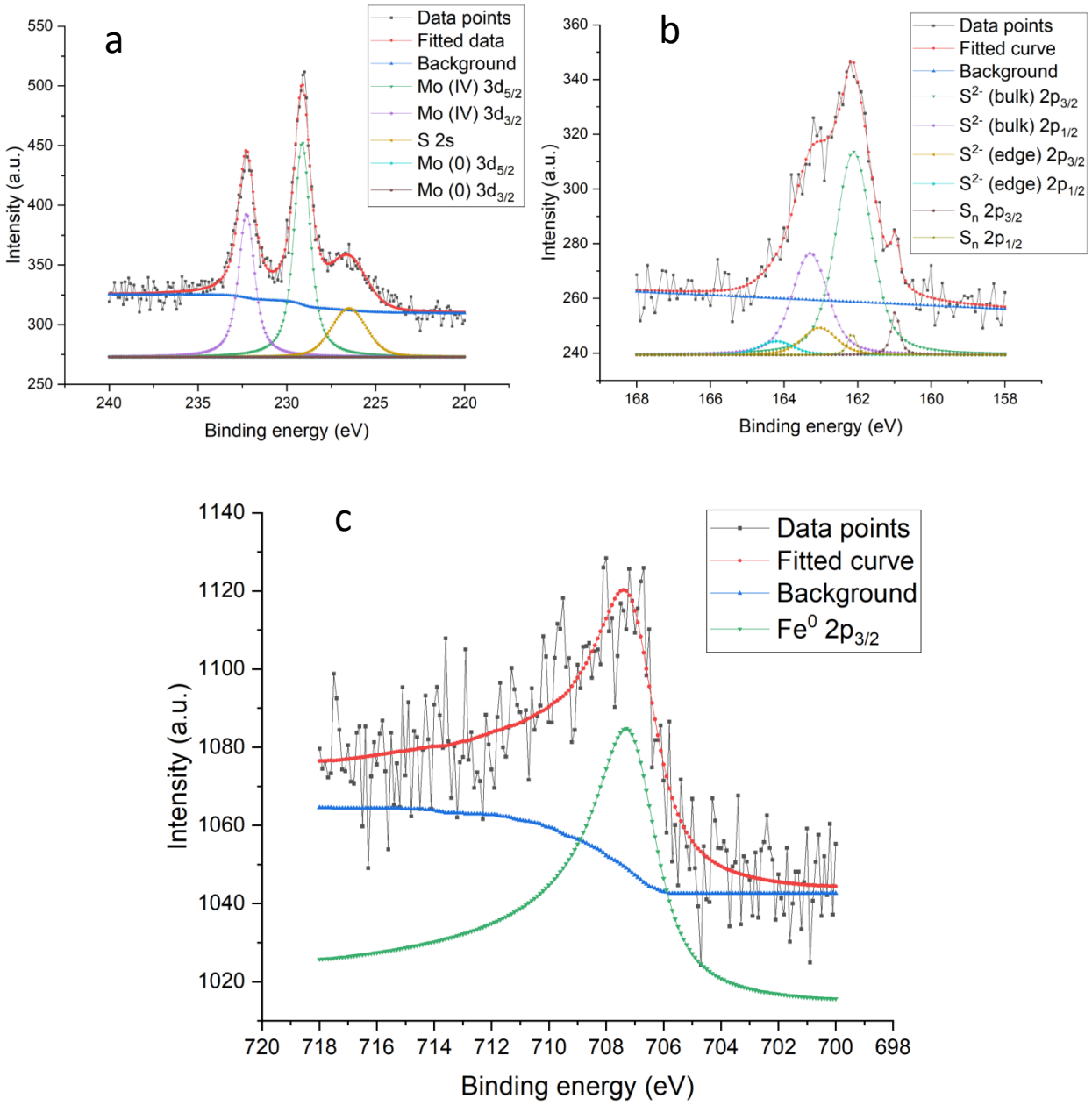

Figure 4.40 - XPS Mo 3d, S 2p and Fe 2p spectra of the Fe-nanoparticle decorated MoS_2 surface after the second annealing cycle.

The Fe 2p spectrum, in figure 4.6c, shows a shifted peak from 706.8 eV of the metallic iron to 707.7 eV, possibily indicating the sulfurization of part of the iron. However, due to the low quantity of iron present on the sample and the noise in the spectrum, it was not possible to properly fit the peak.

The annealing cycles failed to incorporate the iron atoms inside the lattice of the MoS_2 and the only appreciable difference between the sample before and after the annealing is the migration of the iron nanoparticle towards the step-edges of the sample, which form larger clusters of nanoparticles, as it is possible to see in figure 4.6.

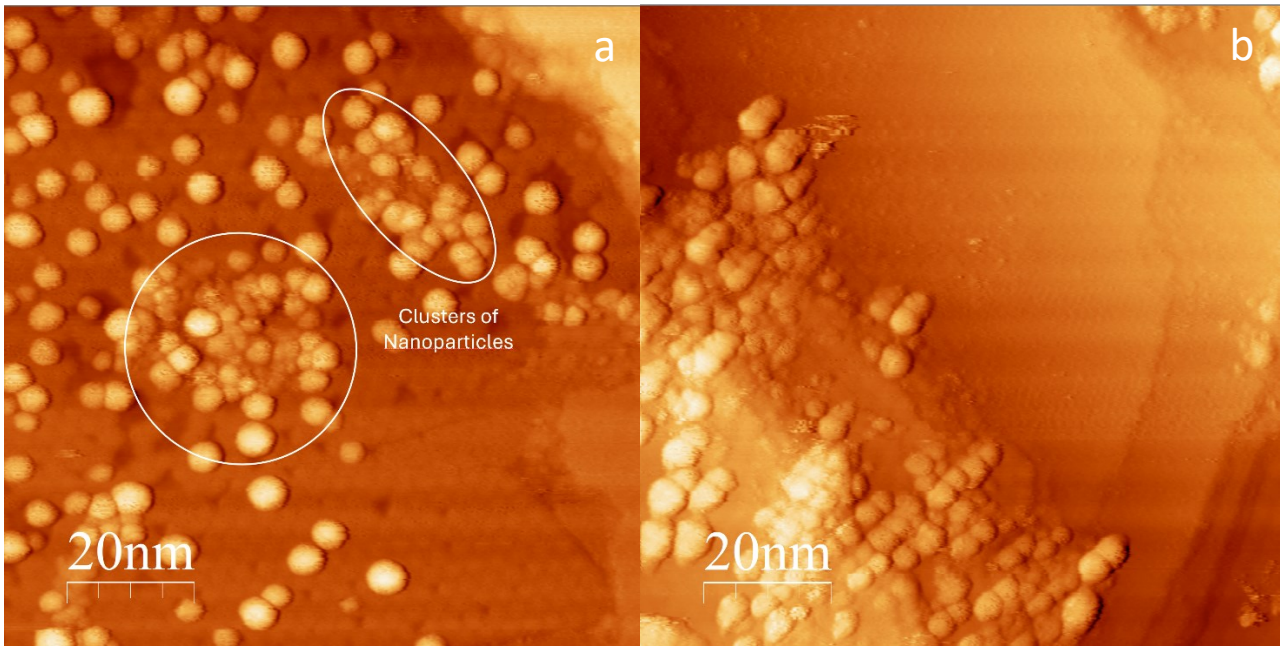

Figure 4.41 - (a) (I=0.8 nA, V=0.6 V, 100x100 nm) Aggregation of Fe nanoparticles after thermal annealing. (b) (I=0.7 nA, V=0.6 V, 100x100 nm) Migration of Fe Nanoparticles towards the step-edges after thermal annealing. Next to the step edge it is possible to observe a large terrace depleted of nanoparticles.

As discussed in chapter 3, MoS_2 was deposited on the Au substrate, then the prepared sample was placed in a vacuum vessel and brought to the Elettra synchrotron in Trieste. A new attempt at direct iron deposition is made on the same sample that was initially measured by XPS (figure 4.7), depositing 0.2 ML of Fe on the sample's surface.

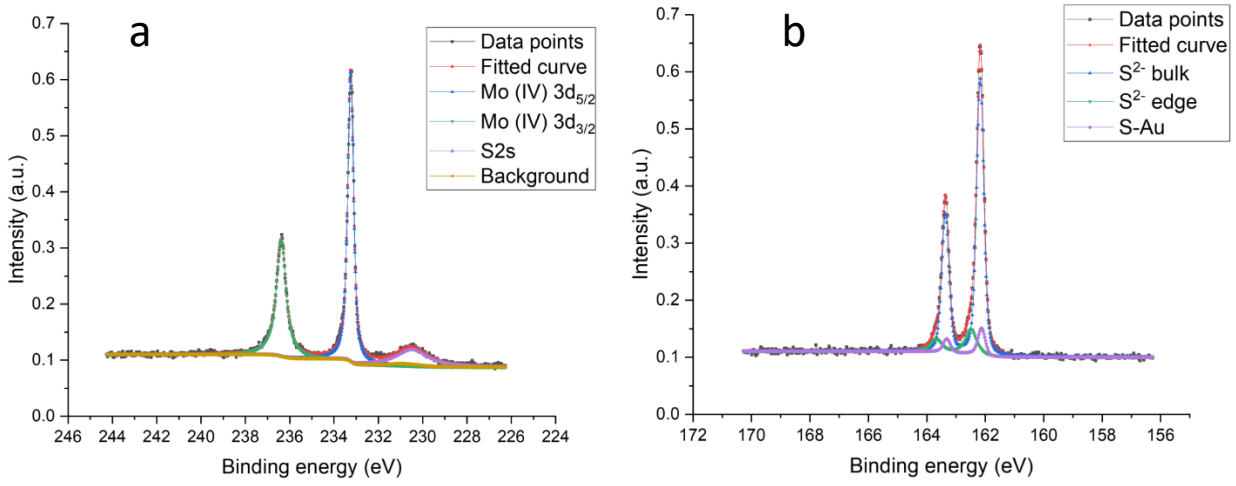

Figure 4.42 - XPS spectra of Mo 3d and S 2p before the deposition. (Reported again for clarity from chapter 3)

The effect of Fe is clearer from the Mo 3d lines (figure 4.9a), where it is visible a shoulder of about 6.5% of intensity at 0.9 eV lower binding energy with respect to the main peak. The shoulder at low binding energy of Mo 3d has been linked in the literature to defective unsaturated Mo, [3] but this interpretation can be excluded for the well-defined Mo 3d peak observed in the as-prepared sample due to the strong excess of sulfur during growth. Therefore, this change in Mo 3d is attributed to the sharing of sulfur from MoS_2 to the Fe NP surface. This new component has a Gaussian profile, in contrast to the Lorentzian profile of the main MoS_2, indicating possible slightly different chemical shifts not resolvable by XPS. The low intensity of this new component, compared to a theoretical iron coverage of 20%, is related to the formation of NPs, which expose only a small part of Fe to MoS_2, while the majority of Fe is within the NPs and thus not directly interacting with MoS_2. After the deposition of Fe a shoulder, at slightly lower BE, can be observed in the Mo 3d spectra, previously not observed.

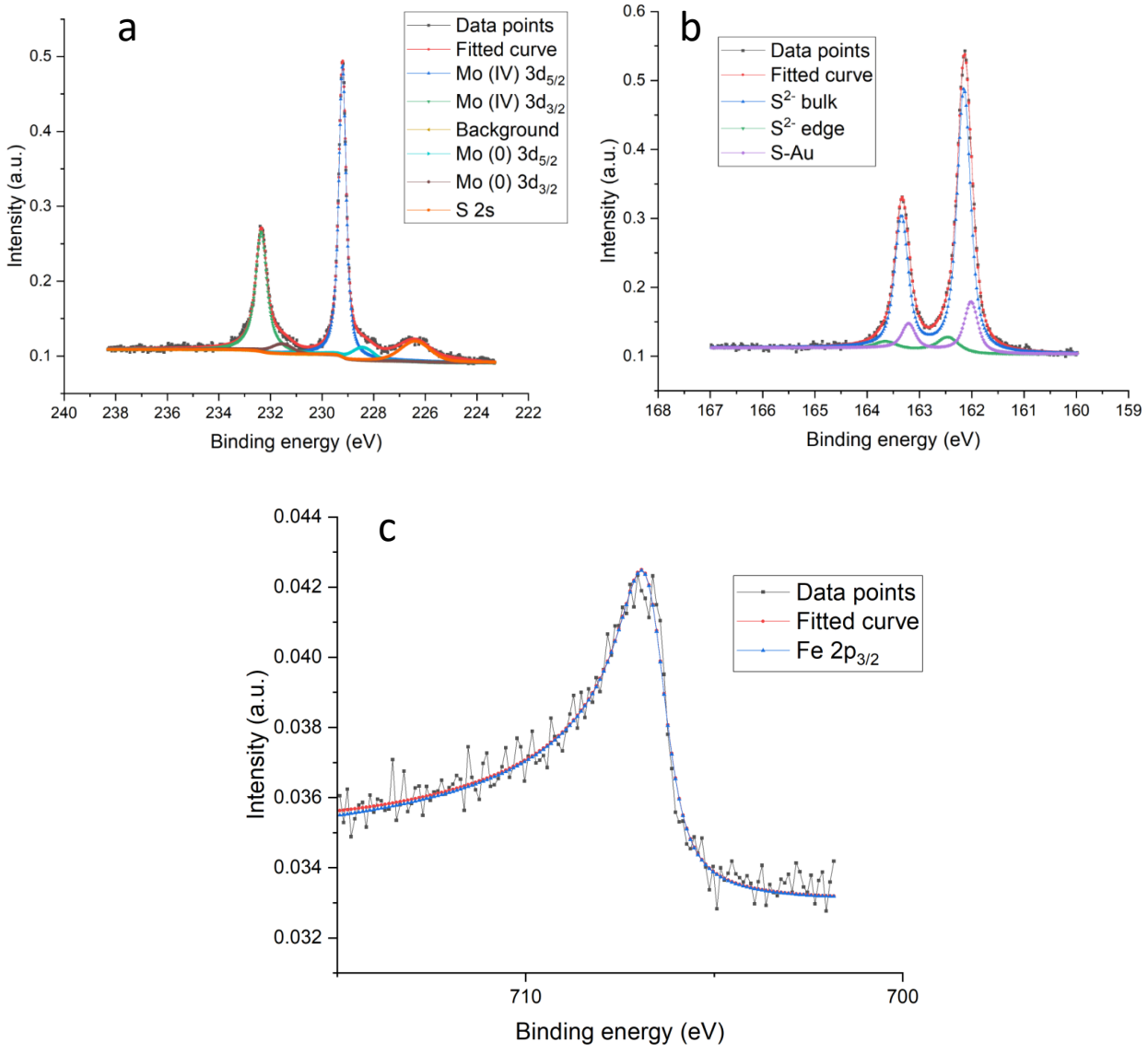

Figure 4.43 - Syncrotron XPS spectra of Mo 3d, S 2p and Fe 2p after the deposition of Fe nanoparticles, obtained with radiation at 1020 eV.

After the Fe deposition the S 2p spectrum shows a similar amount of defective sulfur at high binding energy compared to as-prepared sample and a very small, almost negligible, new component at low binding energy. This can prove how the Fe is not affecting the fractal edge but just sitting on the MoS_2 surface. This hint, combined with the Gaussian profile of the low binding energy peak in Mo 3d, suggests the random nucleation of Fe NPs independently on the edge of the MoS_2, as proved by STM. As shown in figure 4.9, the spectrum of the S 2p remains unchanged after the Fe deposition.

The Fe 2p peak shows a predominantly metallic phase with a sharp Fe $2p_{3/2}$ at 707 eV, confirming that most of the signal comes from the core of the NPs.

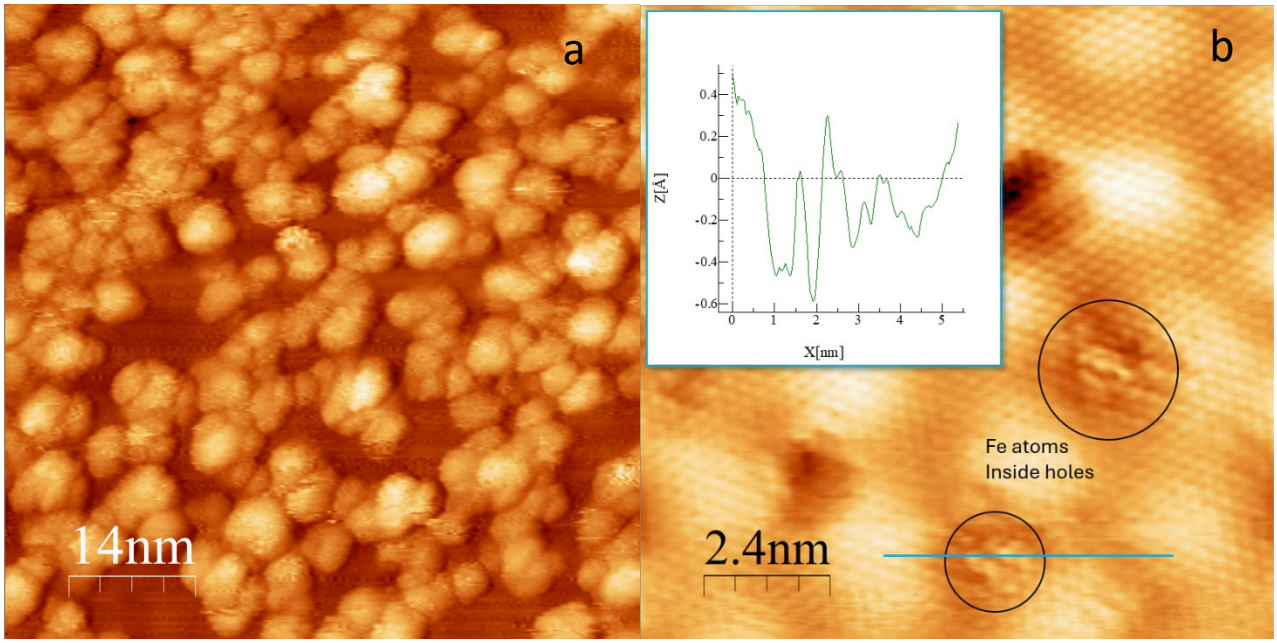

Figure 4.44 - Surface of the sample after the measurements performed at the Elettra synchrotron, that display the possible nanoparticles found. (a) (I=0.2nA, V=1.0V, 70x70nm) An area covered with iron nanoparticles. (b) (I=1.1nA, V=0.3V, 10x10nm) Atomic resolution image, in some of the holes in the MoS2 lattice it is possible to see amorphous nanoparticles of iron.

From the STM imaging done after the sample was brought back from the Elettra synchrotron, atoms of iron are present inside holes in the MoS_2 lattice; these likely act as nucleation centers for the subsequent growth of the NPs. Since the sample was exposed to air for a prolonged period of time, the visible inclusions within the vacancy islands of the could also be contaminations of carbon and oxides.

4.2 Sulfurized iron deposition

In order to properly characterize what can be achieved using the same parameters set for the deposition of sulfurized Fe in UHV a film of Fe_xS_y is deposited on the Au (111) crystal. Note that chronologically this deposition was performed in between the first and second attempt at a mixed Mo/Fe deposition.

The procedure closely mirrors that of the mixed material deposition, and it starts by heating Au (111) crystal to the deposition temperature, T_d, followed by introducing the flow of S vapor in the preparation chamber 5

minutes before the deposition; the flow of S vapors in this deposition raises the pressure to $1.5x10^{-7}$ torr. The shutter of the Fe evaporator is kept open for 25 minutes; the conditions for the temperature control and the Fe evaporator are reported in table 4.1. After the deposition, the sample is kept at T_d and under the flow of S vapor for 15 minutes. The temperature of the sample is then brought and kept for 5 minutes at annealing temperature, T_a. Afterward, the S vapor flow is shut off and the sample is cooled to room temperature.

Table 4.1 - Conditions for the temperature control and e-beam evaporators of the sulfurised iron deposition.

Temperature control parameters			
Heating speed	**22 K/min**	**Cooling speed**	**16.5 K/min**
T_d (°C)	**350**	**T_a (°C)**	**250**
E-Beam evaporator parameters			
	Applied bias (kV)	**Emission current (mA)**	**Filament current (A)**
Fe E-beam parameters	**0.8**	**10.0**	**2.65**

Comparing the spectra, as shown in figure 4.11, it is possible to see a shift in BE between the spectra of the Fe NPs and the spectra obtained both in the mixed and the sulfurized iron depositions.

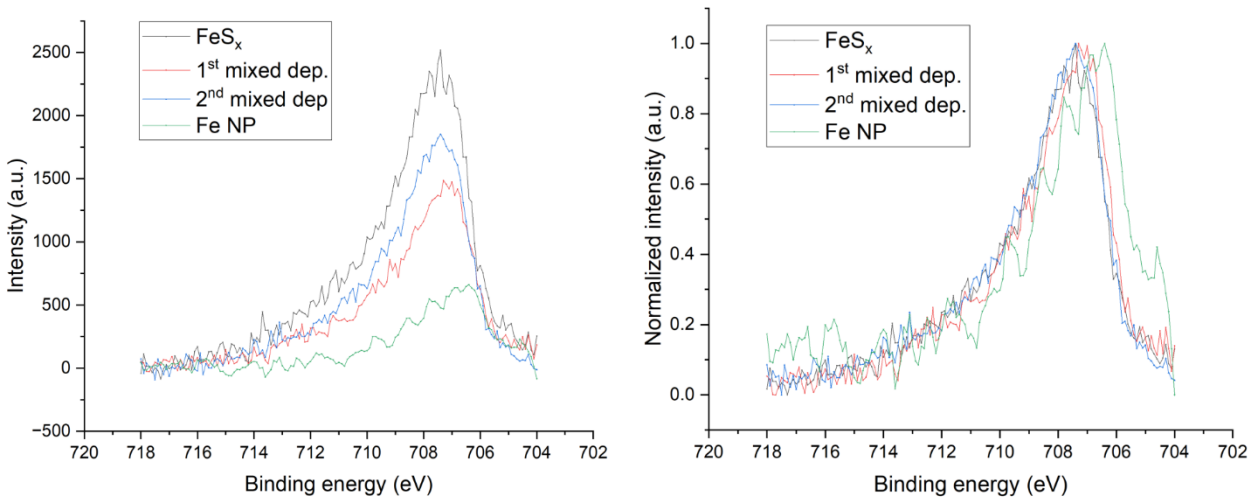

Figure 4.11 – (a) Comparison of the initial Fe 2p spectra obtained in the different Fe deposition attempts (note that the Fe 2p spectrum of the Fe Nanoparticles is scaled up by a factor of 100). (b) Comparison of the same Fe 2p spectra normalized between 0 and 1.

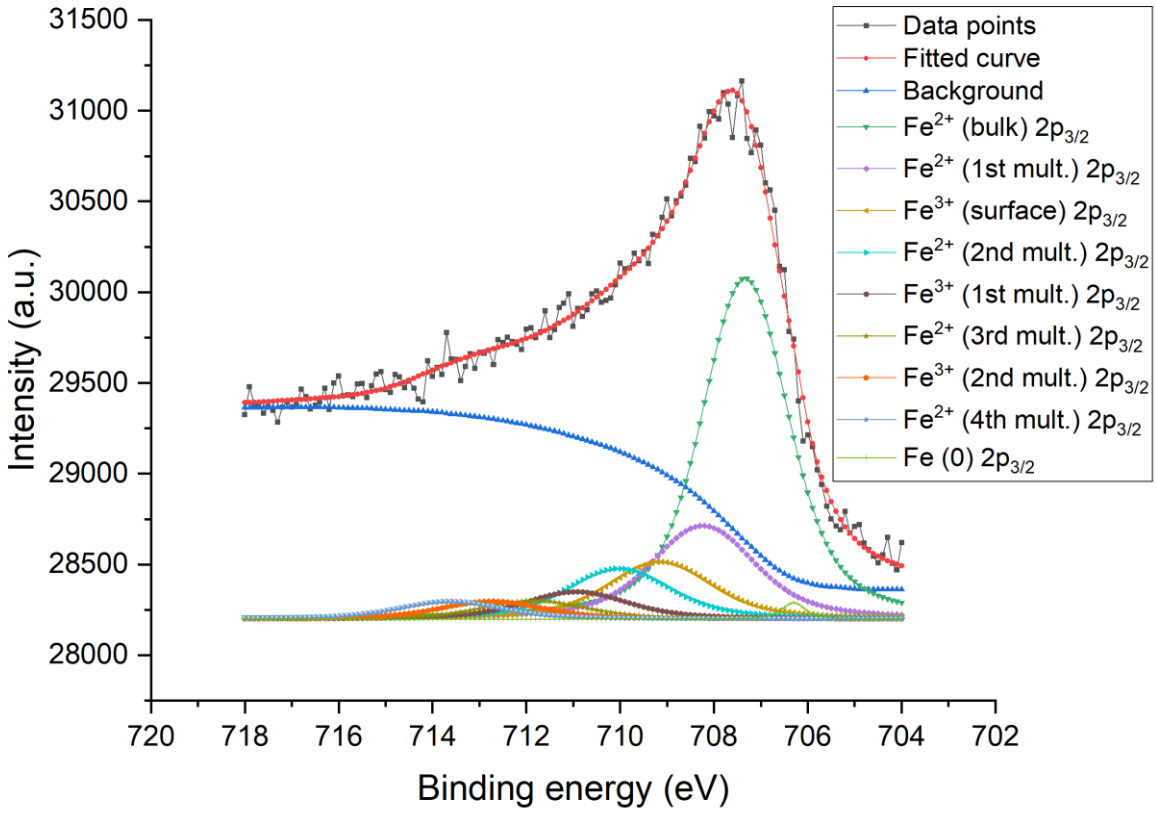

Figure 4.12 - XPS Fe 2p spectrum of the sulfurised iron material.

The Fe 2p spectrum of pyrite presents a strong near-symmetric component, centered around 707 eV, and a "tail" toward higher binding energies, which contains the signal coming from multiplets and from iron in other oxidation states, intrinsically present in the sulfides. Similarly, the obtained Fe 2p spectra has a main component found at 707.3 eV, which is attributed to Fe^{2+} bulk sites, and the tail of the curve could originate either from Fe^{3+} surface states or as an energy loss feature associated with bulk states. As reported by Nesbitt et al., the presence of Fe^{3+} is explained by the transfer of an electron from Fe^{2+} surface species to S^{-} ions to produce Surface Fe^{3+} and S^{2-} ions:

$$Fe^{2+}_{surface} + S^{-}_{surface} \rightarrow Fe^{3+}_{surface} + S^{2-}_{surface}$$

This electron transfer occurs during the surface relaxation, due to the instability of S- monomers. [10]

The tail, at higher binding energies, contains multiplets that arise from surface states; the main component of the curve is associated with low spin states for Fe^{2+} in the material's bulk, while the Fe^{2+} ions at the surface or on edges are found in an intermediate spin state and are associated with multiplets found in the "tail" of the curve, at higher binding energies. Alongside the peaks for Fe^{0}, at 706.3 eV, negligible in our case, and the main peak of bulk Fe^{2+}, at 707.3 eV, other multiplets, separated by about 1 eV, are found in the spectrum

(figure 4.12), at 708.2, 710.0, 711.8 and 713.7 eV, for the Fe^{2+} ions, with three more peaks that account for Fe^{3+} ions at 709.1, 711 and 712.8 eV. The area of the multiplets of Fe^{2+} ions accounts for about 18% of the total area of the curve, while the multiplets of Fe^{3+} ions account for 12% of the total area of the curve. [11–13]

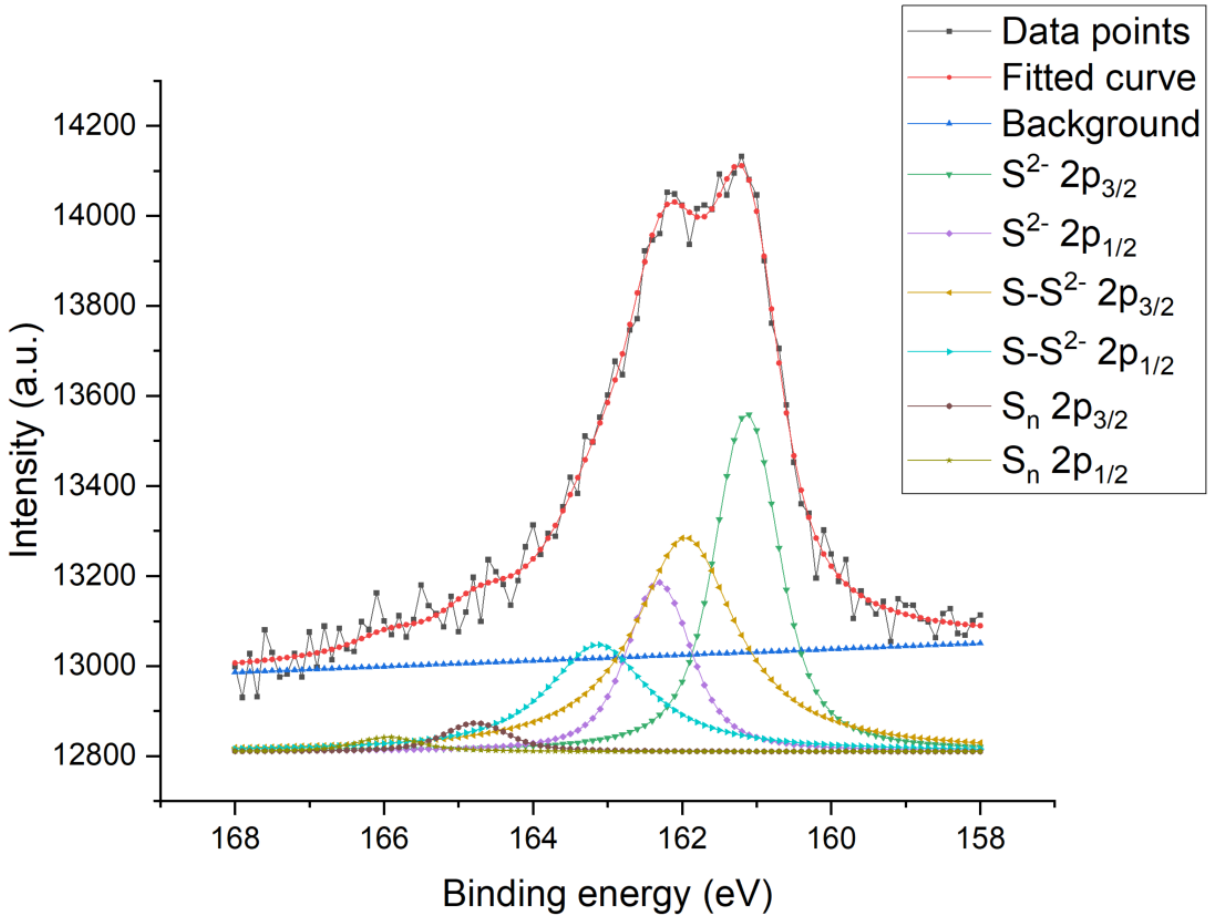

Figure 4.13 - XPS S 2p spectrum of the sulfurized iron film.

The spectrum of S $2p_{3/2}$, in figure 4.13, shows a different structure from the other spectra of S 2p previously shown. The fit of the obtained curve shows two doublets, at 161.2 and 162.4 eV and at 162.1 and 163.3 eV, which are attributed to monosulfide (S^{2-}) and disulfide ($S\text{-}S^{2-}$) ions. Nesbitt et al. report that disulfide ions are the major component of the sulfur ions bonded to Fe in freshly cleaved pyrite, with a smaller presence of mono and polysulfides; however, in the XPS spectrum of the S 2p of the deposited material, the major peak is associated to the monosulfide ions. This discrepancy between the results found in this work and the data reported in the literature is explained by the results found by Bronold et al.: in the XPS spectra of sulfurized iron films the monosulfide ions component increases as the deposition temperature increases. These results show that a noticeable peak, associated with monosulfide ions, is found when the FeS films are grown at a temperature very close to the one used for the deposition reported in this work. [10,13,14] In this spectrum, likely because of the excess presence of S vapor in the preparation chamber, there is a tail towards higher BE, which could indicate the presence of clusters of elemental sulfur.

The sulfurised iron surface presents triangular islands on material, as shown in figure 4.14.

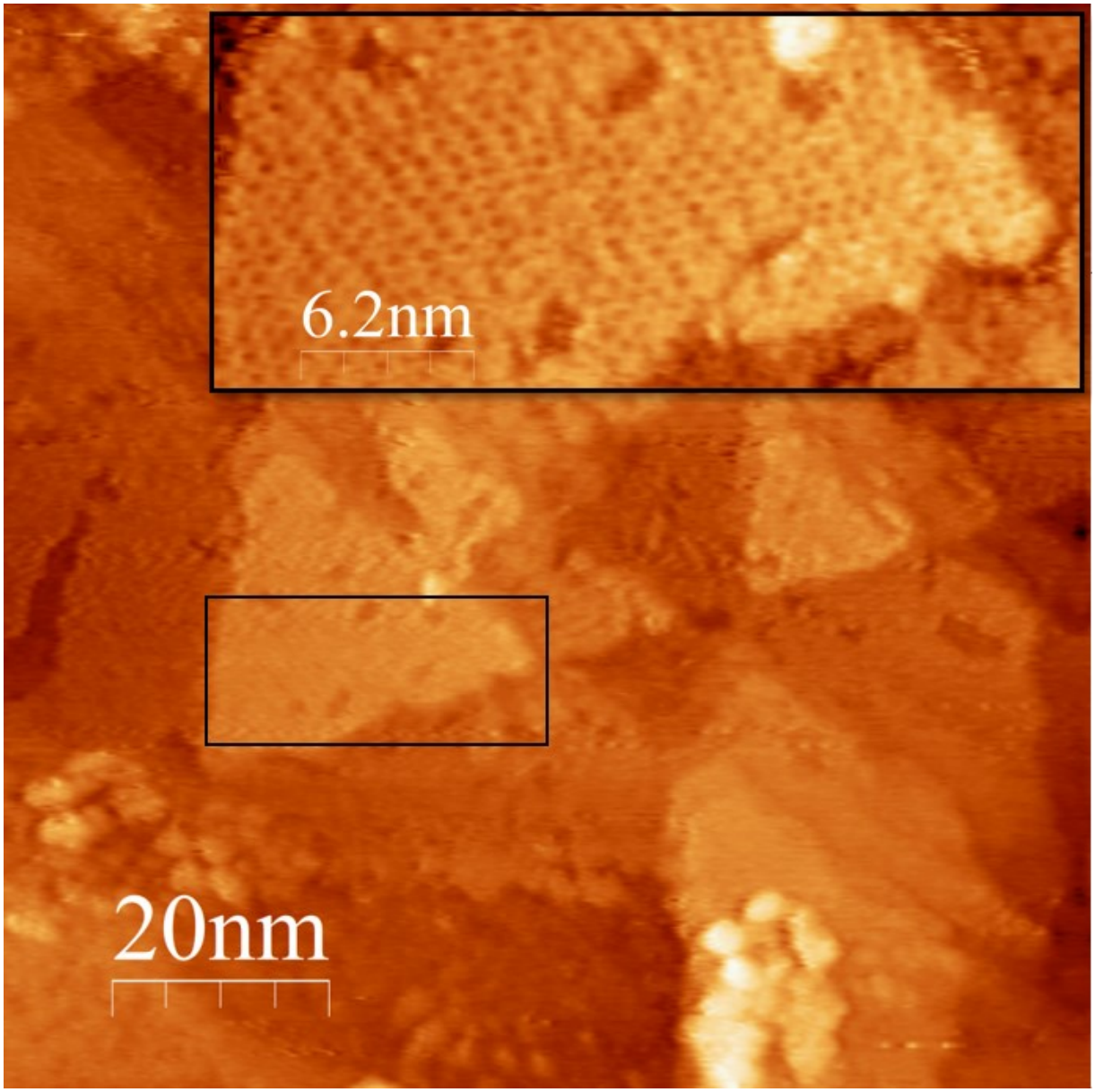

Figure 4.14 - (I=1.5nA, V=-0.6V, 100x100nm) Triangular islands of FeSx. (Highlited in the inset, I=1.5nA, V=-1.4V,31x13nm) Atomic resolution image near an edge of a triangular FeSx island.

The material deposited does not show the same electronic modulation effect as was the case of the Moiré pattern in the MoS_2 layers.

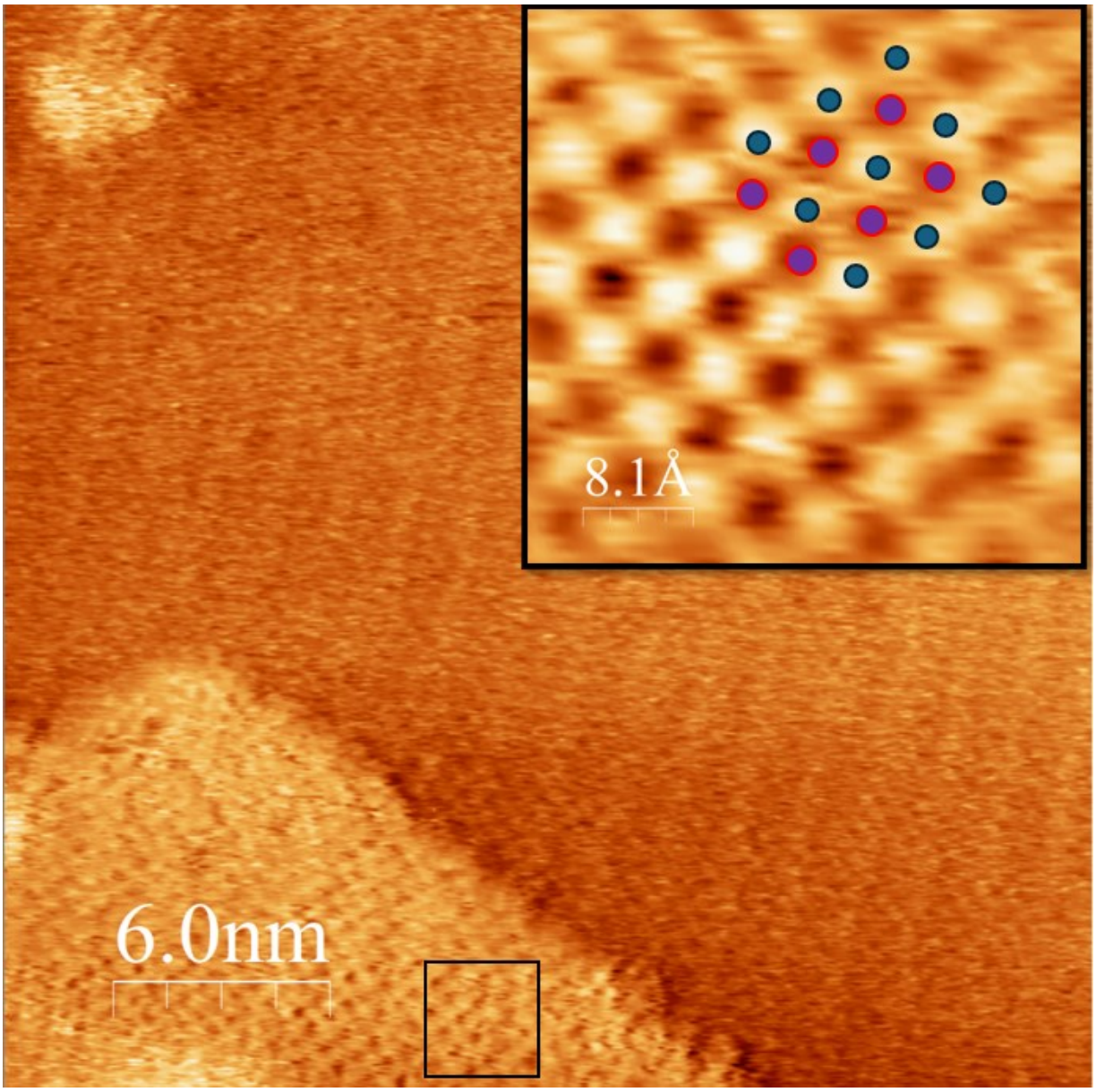

Figure 4.15 - (I=2.5nA, V=-1.4V, 30x30nm) Atomic resolution image of a terrace of sulfurized iron. Below the terrace is a second, more extensive, terrace of FeSx. (Highlighted in the box) Atomic disposition of Fe (blue dots) and S (purple dots) atoms in the lattice.

From the atomic resolution images (figure 4.15), the average distance between atomic centers is measured to be 0.538 nm ± 0.03 and the average distance obtained in the second mixed material deposition seem to be close to the reported lattice parameters of ~0.550 nm of Pyrite (100) and Marcasite (010). [15–17] Davis et al. report that, using a similar procedure for the sample preparation, a layer of pyrrhotite-like FeS is produced on the surface of Au (111). [18,19] However, the material obtained in this work does not share a hexagonal structure with pyrrhotite but seems to have a structure more similar to pyrite (100). The material obtained in this work is possibly a form of pyrite, that possesses a slightly modified unit cell due to surface relaxation or by the interaction with the Au support. [15,20,21]

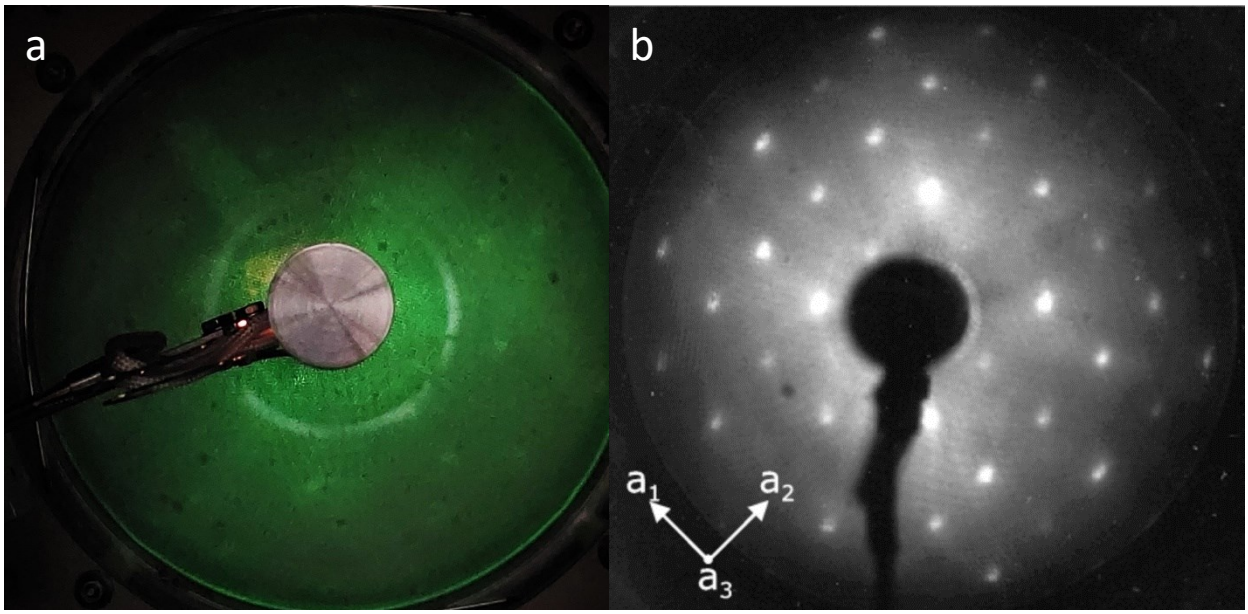

Figure 4.16 - Comparison between LEED patterns for (a) the material deposited in this work, using a beam energy of 80 eV, and (b) the pattern for cleaved pyrite {100}, using a beam energy of 134 eV, as reported by Rosso et al. [15]

The LEED pattern of the sulfurized iron film, obtained in this deposition, is very diffucult to interpret because in the pattern there are several points with a very low intensity. These points allow us to faintly glimpse a crystalline cell, but they are not sufficent for a correct interpretation. The LEED pattern in figure 4.16b is the one reported by Rosso et al. for a in-vacuum cleaved pyrite surface, which presents a cubic cell with a c(2x2) superstructure. [15]

4.2 Mixed Deposition

Since the direct deposition of Fe on a prepared MoS_2 surface failed to produce a solid solution or a mixed nanocomposite, the simultaneous deposition of MoS_2 and FeS is attempted to try to directly incorporate sulfurized iron into the MoS_2 lattice. This deposition is adapted from the depositionthat resulted in a clean, pure surface of MoS_2, described in chapter 3. The sulfur in these depositions is transformed in its vapor form by sublimation but, unlike previous deposition attempts, it is further atomized through the use of a homemade cracker, as described in chapter 2.

4.2.1 First mixed deposition

The Au (111) crystal is first heated to deposition temperature, T_d. The sulfur is dosed on the sample 5 minutes before the deposition, raising the pressure of the preparation chamber to 1.4×10^{-7} torr. The shutters of both the Mo and Fe evaporators are kept open for 25 minutes and after the deposition, the sample is kept under a flow of S vapor for 15 more minutes. The conditions for the evaporators and the temperature control are shown in table 4.2.

The temperature is then lowered to the annealing temperature, T_a, and kept at this value for 5 minutes before shutting off the flow of sulfur vapor and letting the sample cool to room temperature.

Table 4.2 - Conditions for the temperature control and e-beam evaporators of the first mixed deposition.

Temperature control parameters			
Heating speed	**22 K/min**	**Cooling speed**	**16.5 K/min**
T_d (°C)	**550**	**T_a (°C)**	**250**
E-Beam evaporator parameters			
	Applied bias (kV)	**Emission current (mA)**	**Filament current (A)**
Mo E-beam parameters	**1.00**	**40.0**	**7.8**
Fe E-beam parameters	**0.8**	**10.0**	**2.65**

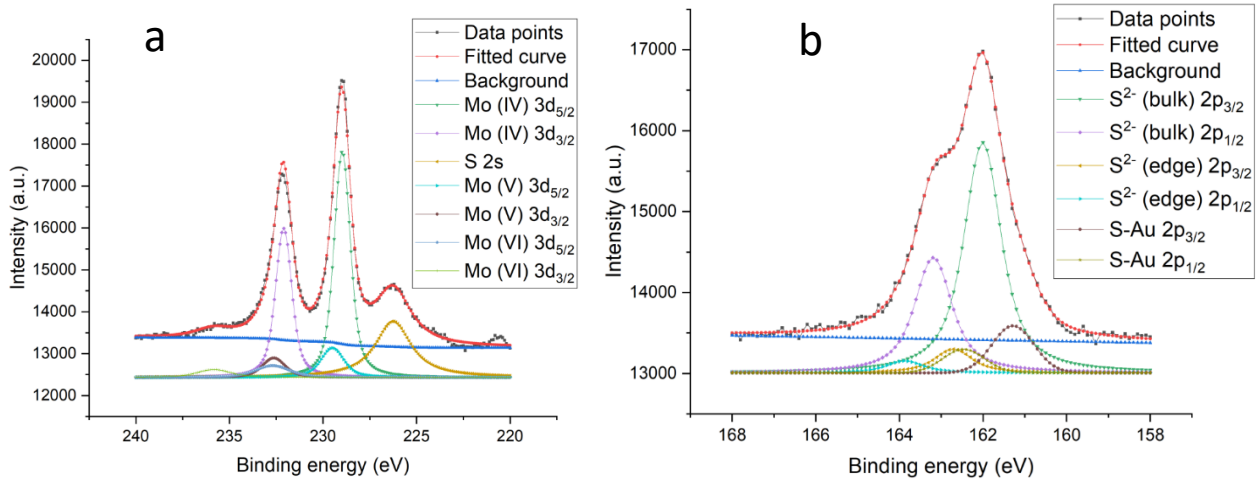

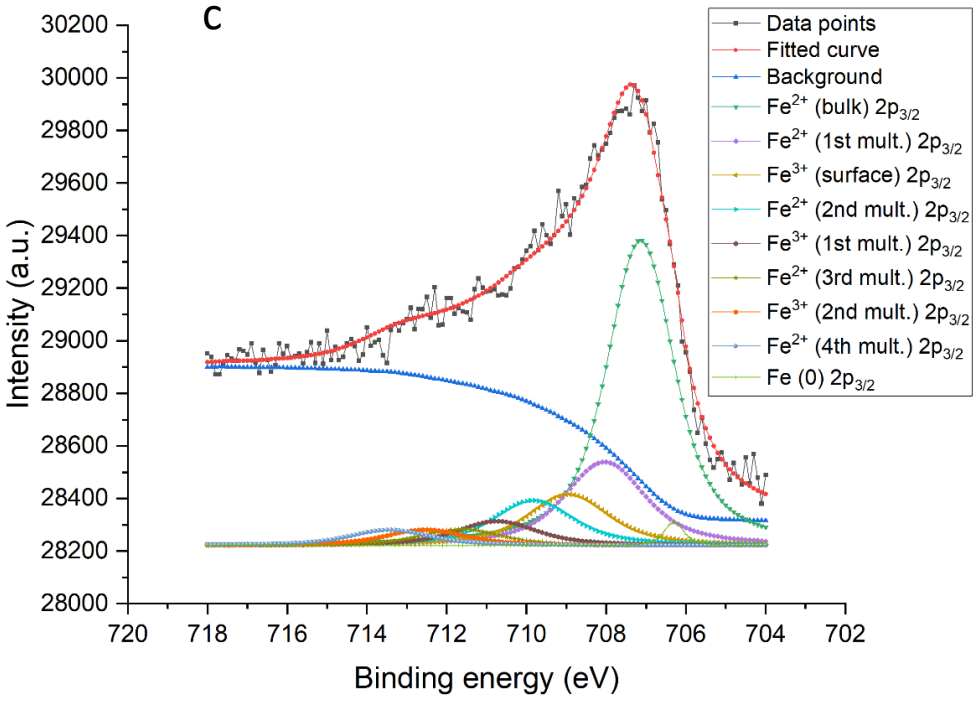

Figure 4.17 - XPS Mo 3d, S 2p and Fe 2p of the first attempt at a mixed deposition.

The spectrum of Mo 3d (figure 4.17a) comprises a doublet at 229.9 and 233.1 eV, corresponding to Mo^{5+}, and a doublet at 232.5 and 235.8 eV, corresponding to Mo^{6+}. Both of these doublets were not present in the spectra of previous depositions, and possibly indicates the presence of pairs of defects of Fe^{3+} and Mo^{5+} or Fe^{2+} and Mo^{6+} ions in contact with each other, both of which are ionic pairs isoelectric to a pair of Mo^{4+} ions. [22–27] This observation is reinforced by the Fe 2p spectrum, which is different from the spectra previously registered for the direct iron deposition on a prepared MoS_2 surface. The Fe 2p spectrum in figure 4.10c also matches more closely the spectrum of sulfurized Fe, shown and discussed in section 4.3.

The S 2p spectrum, in figure 4.17b, the main peaks of the fit, at 162.0 and 163.2 eV correspond to the monosulfide in the bulk of the lattice (S^{2-}), while the monosulfide on the edges is attributed to the peaks at 162.7 and 163.9 eV. However, it should be noted that both Nesbitt et al. and Pratt et al. report that in pyrite the peaks located at 161.9 and 162.7 eV, are attributed to the monosulfide and disulfide ($S\text{-}S^{2-}$) ions respectively, and Brown et al. reports the peaks for the monosulfide ions, in the presence of Mo^{4+}, Mo^{5+} and Mo^{6+} ions, to be around 162.6 eV in modified MoS_2 surfaces. Lince et al. also attribute to the disulfide ions peaks at 162.7 eV, but associate the peaks at 162.0 and 161.7 eV to monosulfide ions, respectively bonded to Mo and Fe. [10,11,27,28] It is possible that the presence of iron shifts the binding energy of the monosulfide ions bonded to Mo to lower BE, but there are certain difficulties in the interpretation of the spectra. [28]

The sample is annealed twice after the deposition to observe whether or not surface modifications occur after annealing: in the first annealing the sample is heated to 550 °C and kept at this temperature for 30 minutes. However, no significant changes were observed.

In the second annealing, this time under a S vapor flow, the sample is heated and kept at 550 °C for 20 minutes; the sulfur vapor flow is opened when the sample is still at room temperature, raising the pressure in the preparation chamber to 4.0×10^{-7} torr. The sulfur vapor flow is shut off while the sample is cooling at around 200 °C. Again, only the XPS spectra registered after the second annealing are reported.

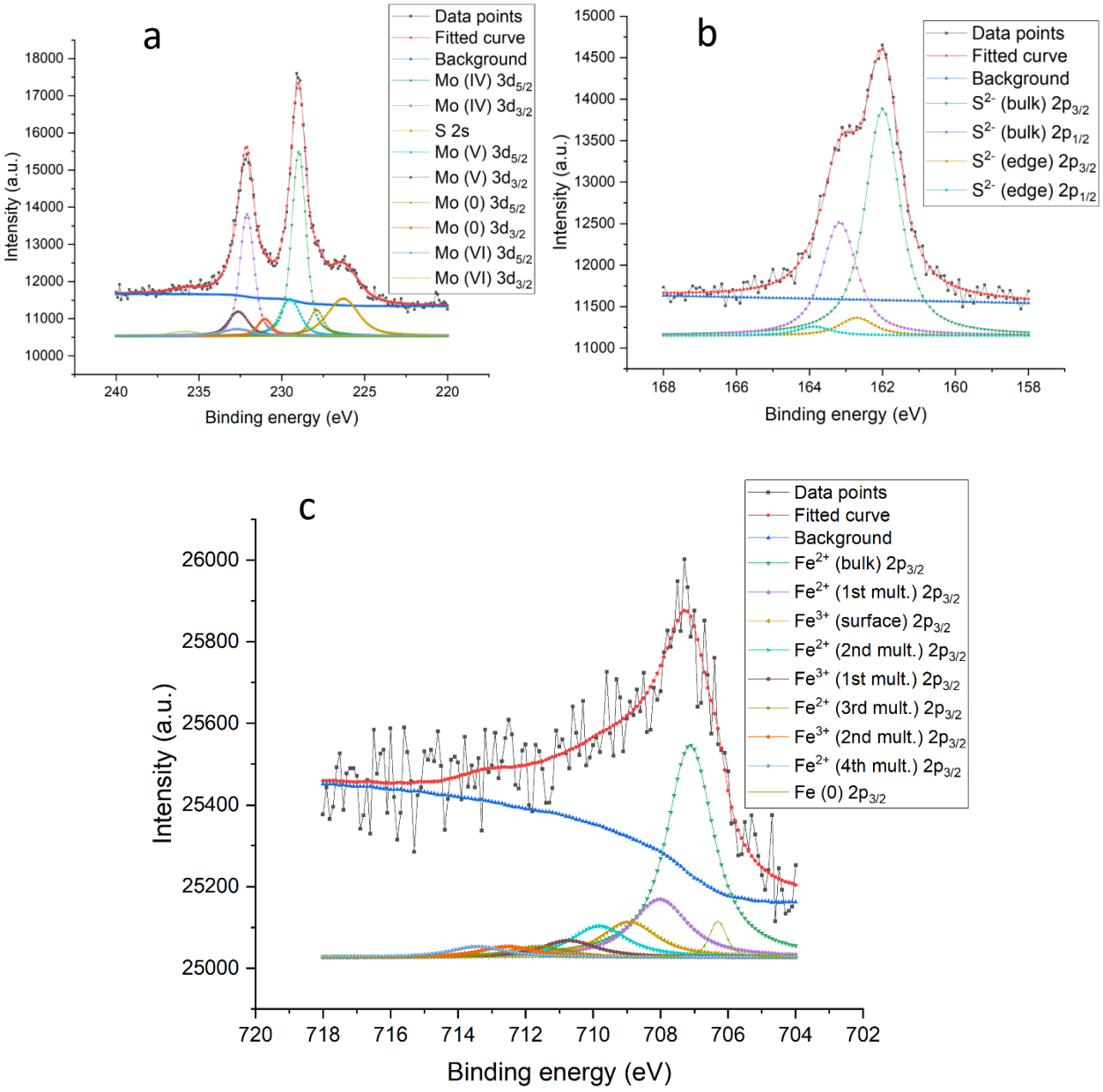

Figure 4.18 - XPS Mo 3d, S 2p and Fe 2p of the first mixed deposition after the second annealing cycle.

The spectrum of Mo 3d (figure 4.18a) after the annealing shows the presence of metallic Mo in the film, with peaks at 227.9 and 231.0 eV, indicating a degradation of the sample at higher temperatures and a significant change is observed in the spectra of Fe 2p.

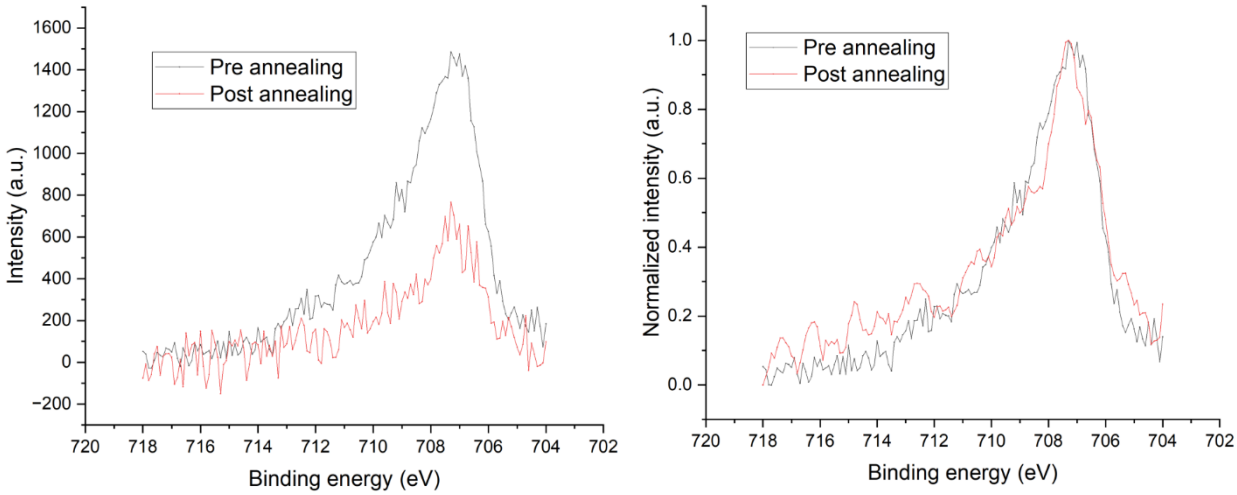

Figure 4.19 – (a) Comparison of the intensities of the Fe 2p XPS spectra after the initial deposition and the second annealing cycle. (b) Fe 2p spectra before and after the second annealing cycle, normalized between 0 and 1.

Both Lince et al. and Davis et al. report the degradation of the Fe_xS_y clusters starts at temperatures higher than 700 K. Lince et al. reported that after annealing, sulfur atoms detach from the corresponding Fe atoms and instead bond with metallic molybdenum defects. After annealing at about 550 °C, the intensity of the XPS signal of Fe 2p decreases drastically, as seen in figure 4.19a, likely because of the iron nanoparticles' degradation and subsequent submersion of the Fe atoms under the layers of MoS_2 and inside the lattice of the Au (111) substrate. [18,28] Because of this effect, one concern in the preparation is to keep the sample at a temperature high enough to allow for the reaction between Mo and S to occur, but low enough not to degrade the sulfurized iron deposited on the surface.

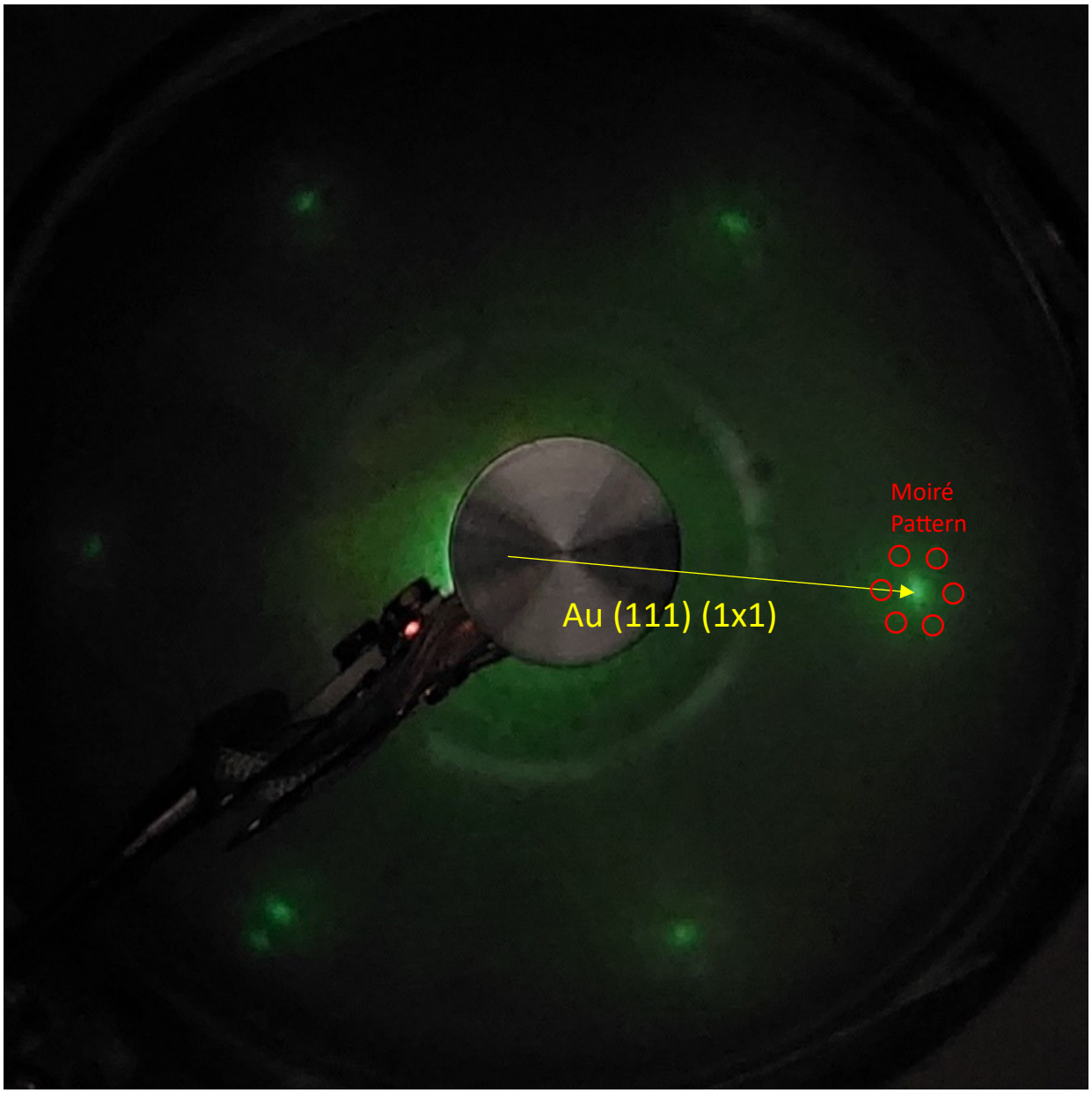

Figure 4.20 - LEED pattern of the mixed deposition after annealing.

The LEED pattern after the annealing does not differ from the pattern of the pure MoS_2, possibly because most of the iron was not incorporated or detached from the MoS_2 lattice, and it was instead submerged into the gold substrate.

The STM images of the mixed material show two separate phases present on the sample's surface.

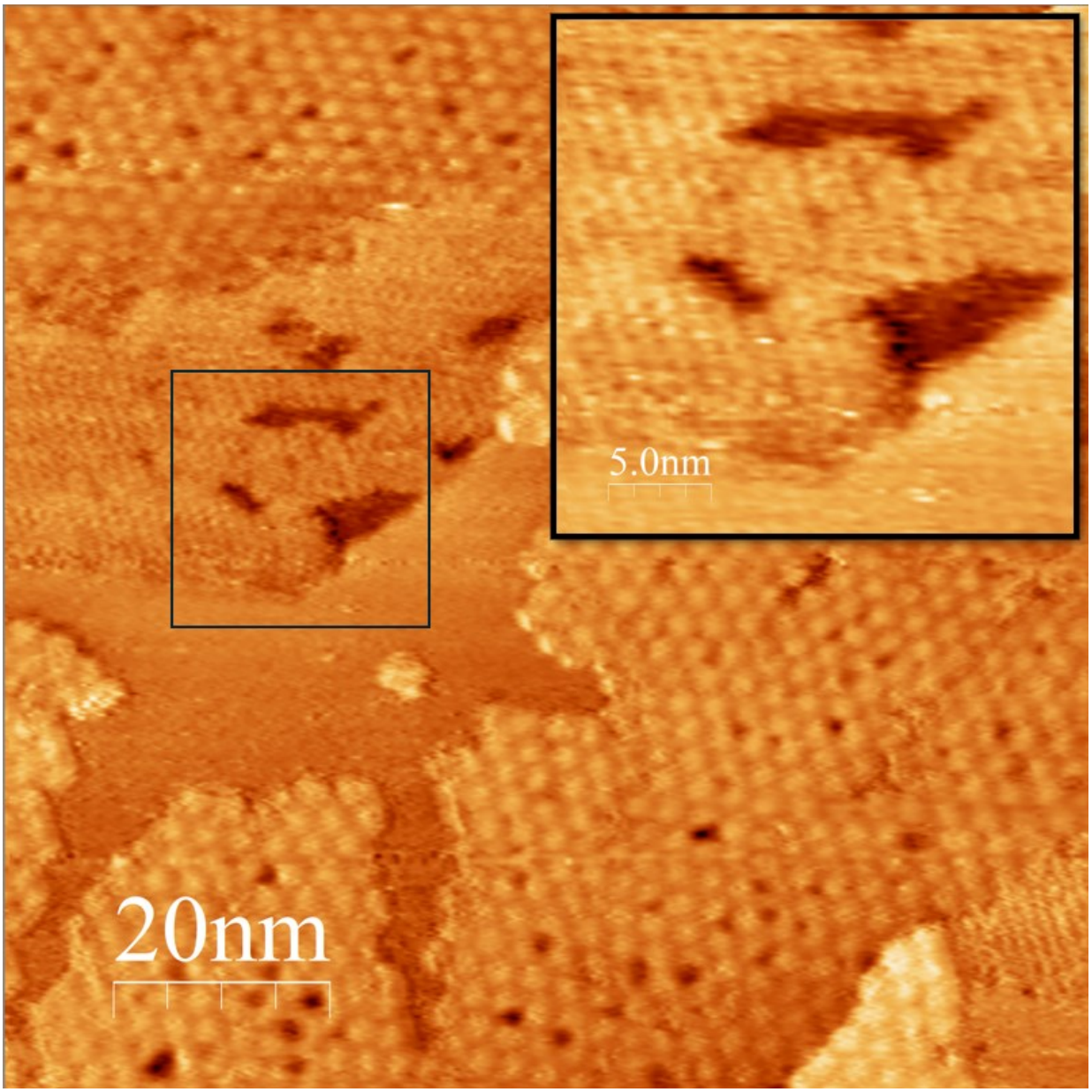

Figure 4.21 - (I=0.7 nA, V=0.8 V, 100x100nm) Different terraces of the surface that present different patterns. (inset) Zoom on the newly present pattern.

The surface is covered with islands that present the expected Moiré pattern, as well as other islands that display a different pattern, as it is shown in figure 4.21. The newtype of islands are difficult to resolve atomically but it was possible at least to identify a row structure with an average distance between lines of 1.22 nm ±0.03. Given that these islands types of structure were never observed when only Mo and S were deposited on Au, it is likely that these islands are formed from sulfurized iron that separated from the MoS_2 lattice to form its own phase. This second phase is also found as separate islands on the Au substrate (figure 4.22). In this case the resolution improved and it was indeed possible to resolve the unit cell, consisting in a hexagonal lattice with a 1.22 nm spacing

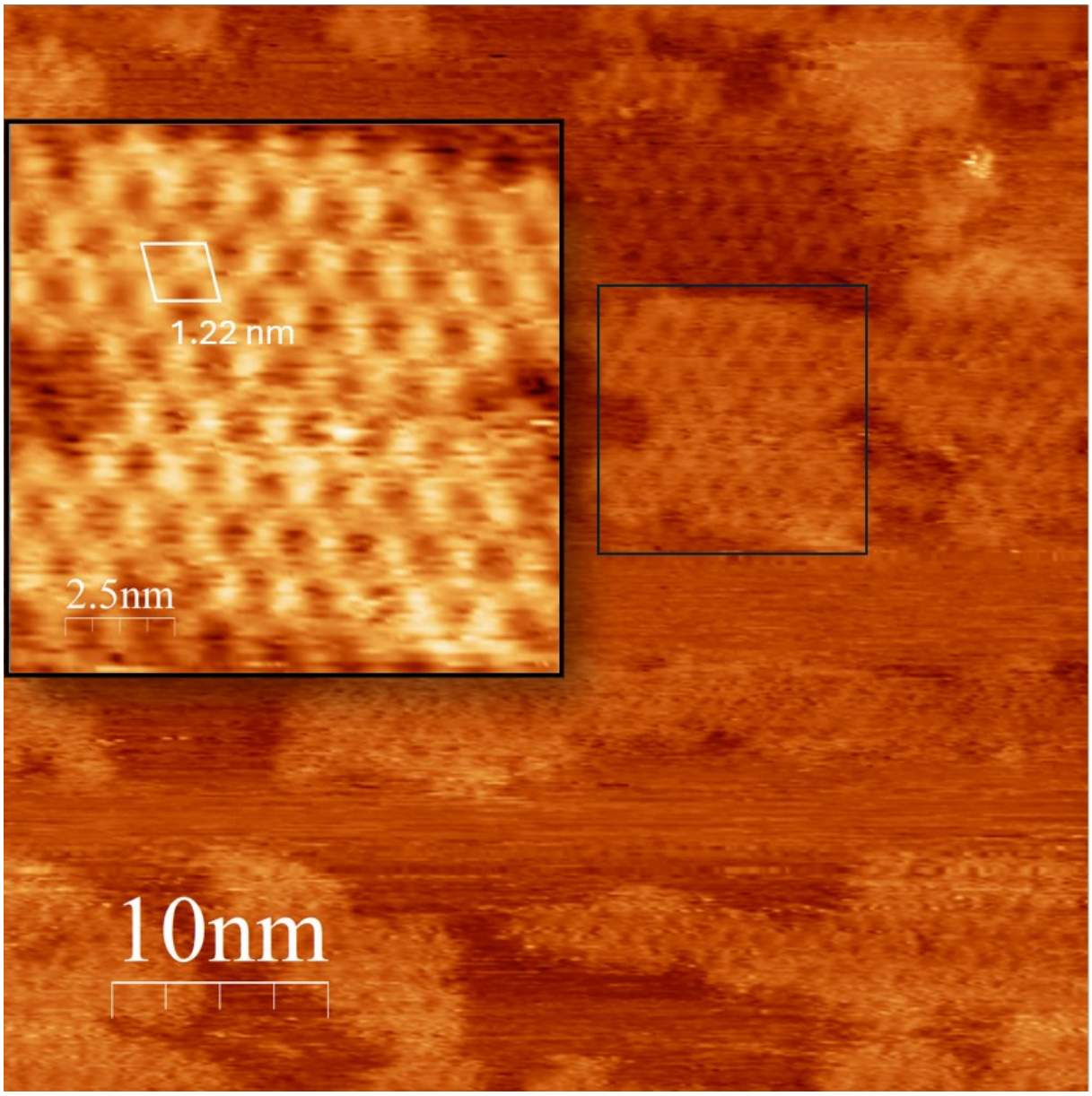

Figure 4.22 - (I=0.3 nA, V=1.3V, 50x50 nm) Islands of the newly presented sulfurized iron phase. (Inset) Zoom on one of the islands.

After the annealing of the material, fewer islands of the sufurized iron phase are present, likely because of the contemporaneous submersion of part of the Fe atoms and the desorption of some of the excess S atoms. Iron atoms also see to have migrated to decorate the step edges of MoS_2 terraces, as shown in figure 4.24 and figure 4.25. Considering the spacing of the newly presented lattice and the XPS spectrum of the obtained sample, the phase observed could be a reconstruction of hexagonal pyrite. [29] Since the sample was abundantly sulfurized, the film obtained could have the conditions necessary to stabilize a surface of pyrite (111), which is normally less stable than pyrite (100).[30] In the paper by Davis et al. the pyrrothite was reported to have a unit cell of about 7x7 Å, with a (1x1) epitaxial structure, while the phase obtained in this mixed deposition has a unit cell almost twice the size, possibly indicating a (4x4) epitaxial structure.

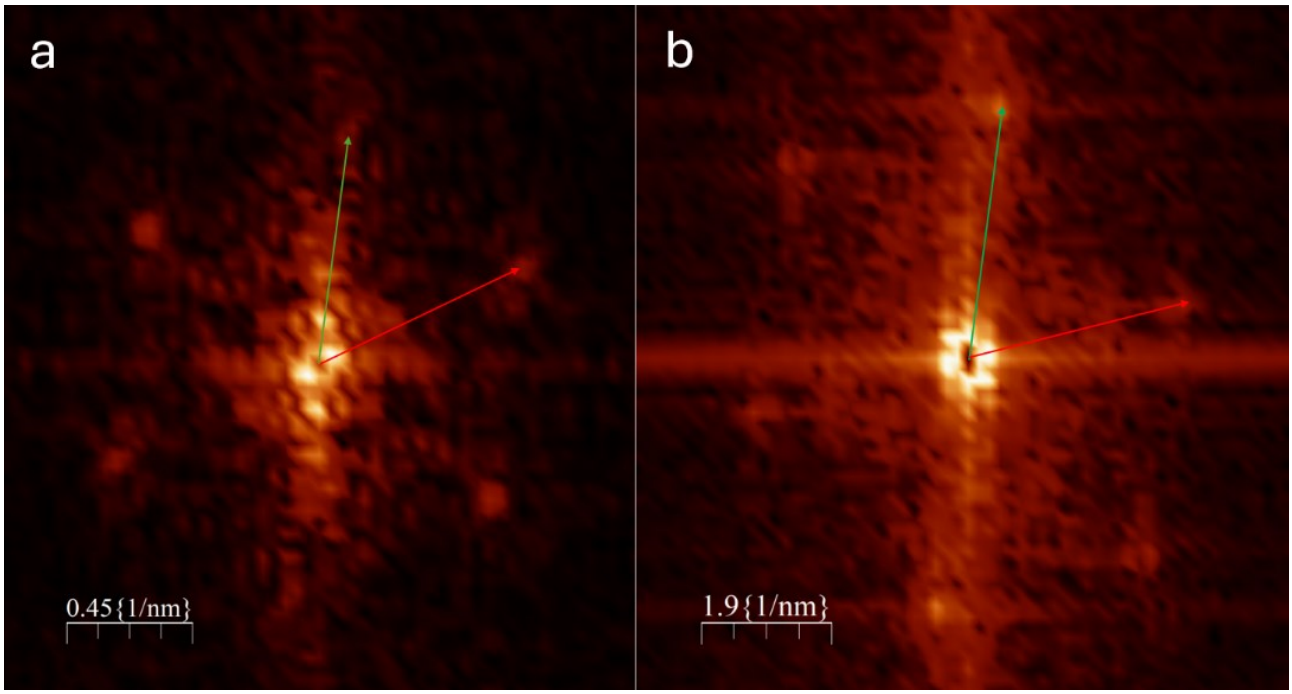

Figure 4.23 – FFT of (a) sulfurized iron and (b) MoS2 phases used to calculate the angle between the two phases.

From STM imaging it was also determined that the two hexagonal structures of the MoS_2 and the separate sulfurized iron, are 12° out of phase with respect to each other (figure 4.23); however, this angle is within the experimental error given by vertical drift in the STM, and the structures are otherwise practically parallel. The alignment of the MoS_2 film is parallel to that of the Au (111) crystal on which it is deposited and consequently, the alignment of the iron phase would also appear to be similarly aligned, parallel to the substrate. These observations seemingly confirm what was previously said regarding the formation of a (4x4) epitaxial structure of pyrite (111) on Au (111).

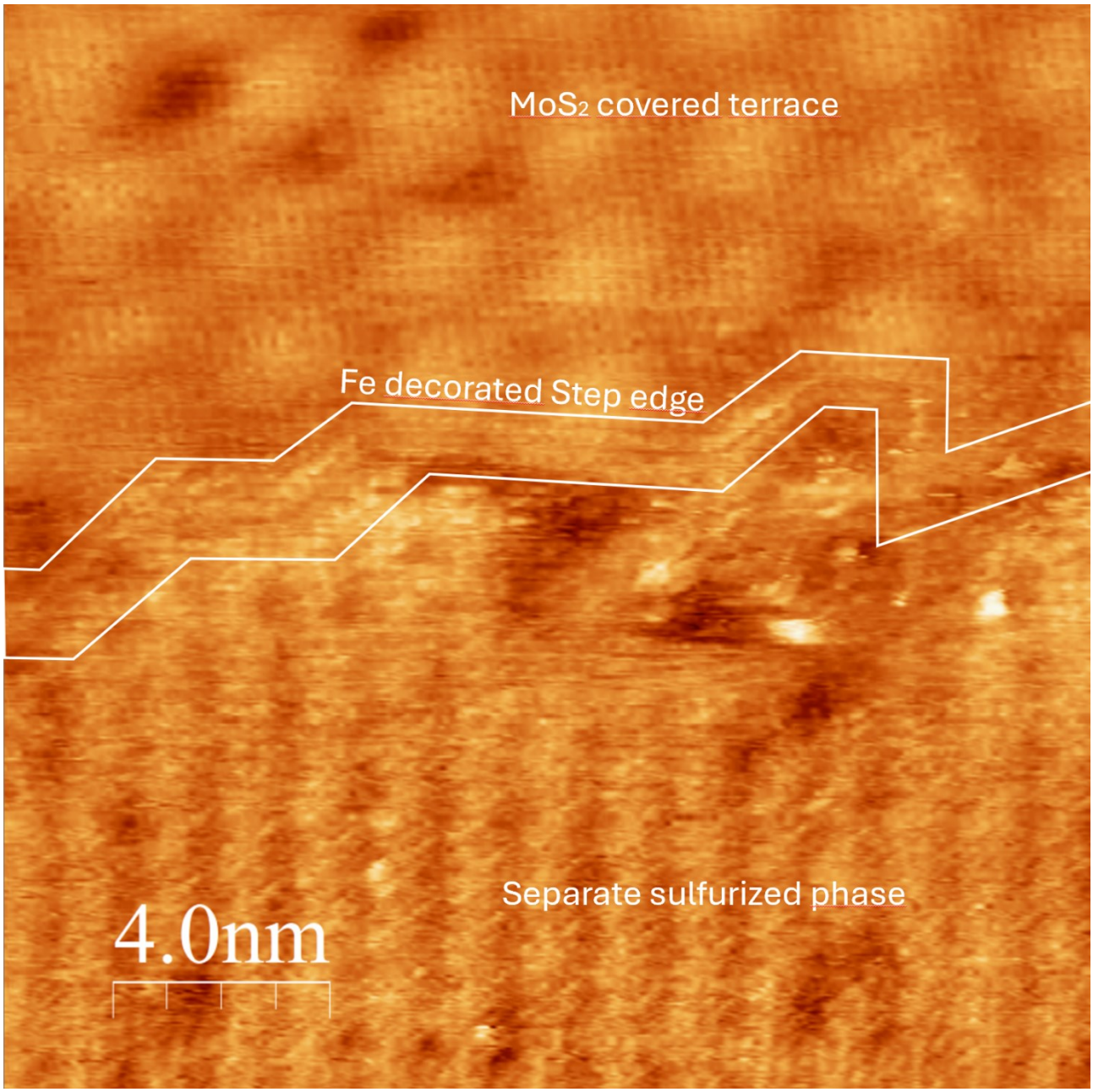

Figure 4.24 - (I=0.7 nA, V=0.8V, 20x20 nm) A step edge between a MoS2-covered terrace, with its characteristic Moirè pattern, and a terrace covered by the sulfurized iron phase.

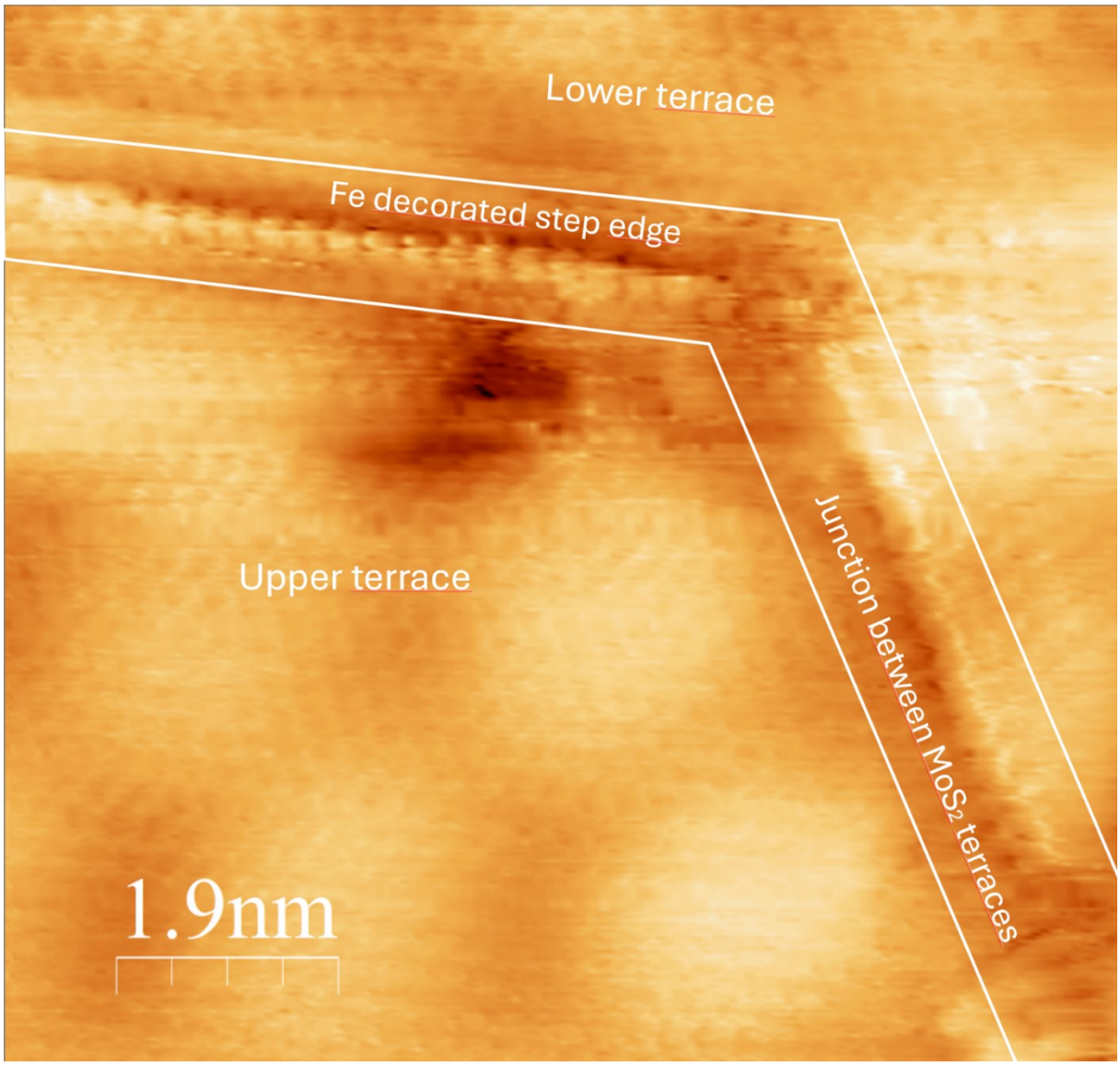

Figure 4.25 - (I=1.2 nA, V=0.4V, 10x10nm) Edge of a MoS_2 terrace, with a junction between two terraces on the same level and a Fe decorated step edge.

4.2.2 Second mixed deposition

Because of the degradation of the material at high temperatures, the mixed deposition is attempted a second time at lower temperature than previous depositions to ensure both that the molybdenum reacts with the sulfur as well as preservation of the sample. Again, the Au (111) crystal is heated to deposition temperature, T_d, before dosing sulfur on the surface of the sample. The sulfur is introduced in the preparation chamber 5 minutes before the deposition, raising the pressure to 1.4×10^{-7} torr. The shutters of both the evaporators of Mo and Fe are kept open for 25 minutes. The conditions for the evaporators and the temperature control are shown in table 4.3. After the deposition, the sample is kept under a flow of S vapor for 15 more minutes. Then the temperature is lowered and kept at annealing temperature, T_a, for 5 minutes before shutting off the flow of sulfur vapor and letting the sample cool to room temperature.

Table 4.3 - Conditions for the temperature control and e-beam evaporators of the second mixed deposition.

Temperature control parameters			
Heating speed	**22 K/min**	**Cooling speed**	**16.5 K/min**
T_d (°C)	**400**	**T_a (°C)**	**250**
E-Beam evaporator parameters			
	Applied bias (kV)	**Emission current (mA)**	**Filament current (A)**
Mo E-beam parameters	**1.00**	**40.0**	**7.8**
Fe E-beam parameters	**0.8**	**8.0**	**2.65**

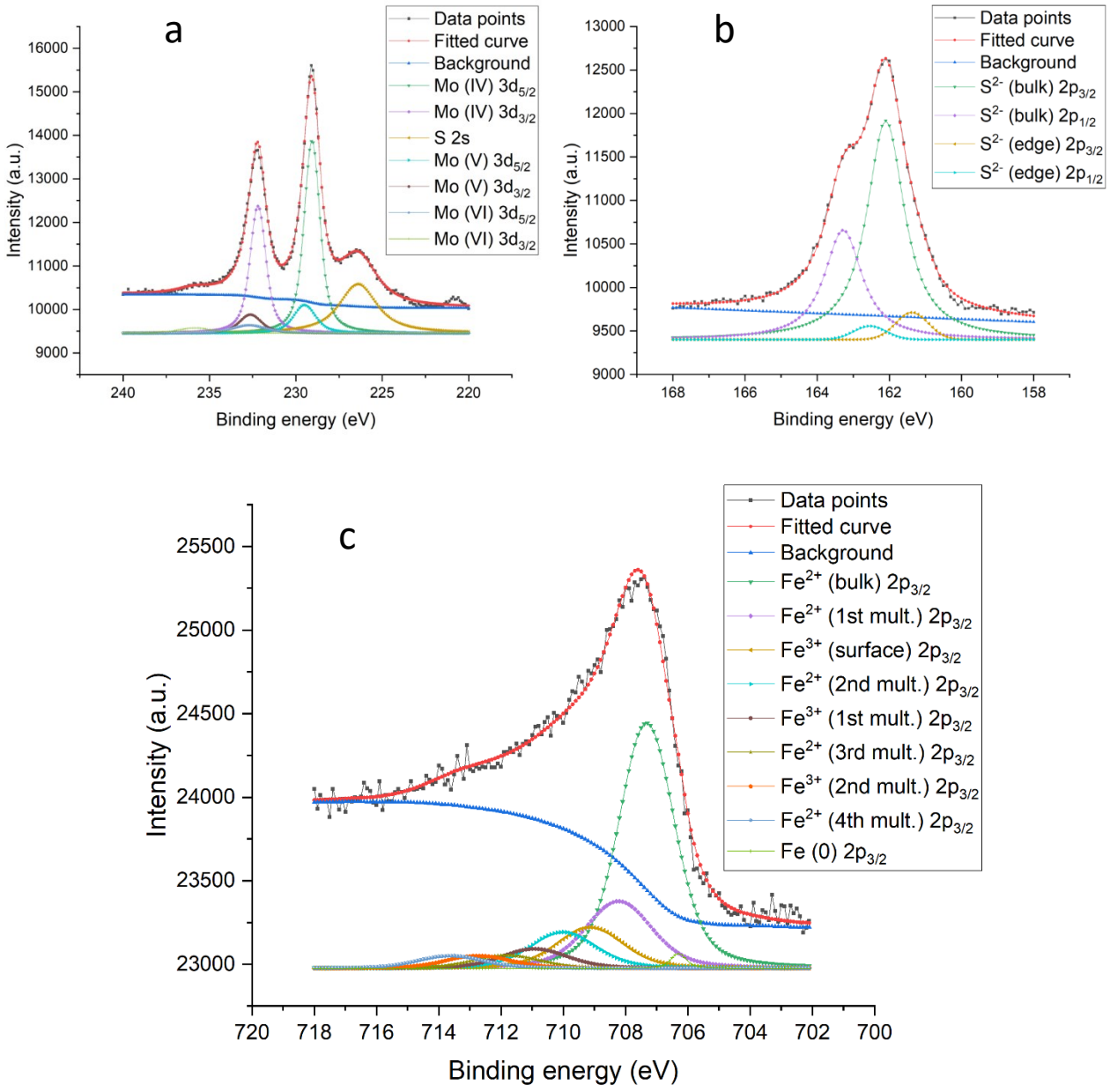

Figure 4.26 - XPS Mo 3d, S 2p and Fe 2p of the second attempt at a mixed deposition.

The XPS spectra of the second attempt at a mixed deposition (figure 4.26) are very similar to the first mixed deposition attempt and show that even at lower temperatures the reaction occurs, incorporating iron in the MoS_2 lattice. It is possible that the main difference between the two depositions is given by the structure that the two prepared films assume, without any discernible difference in the XPS spectra.

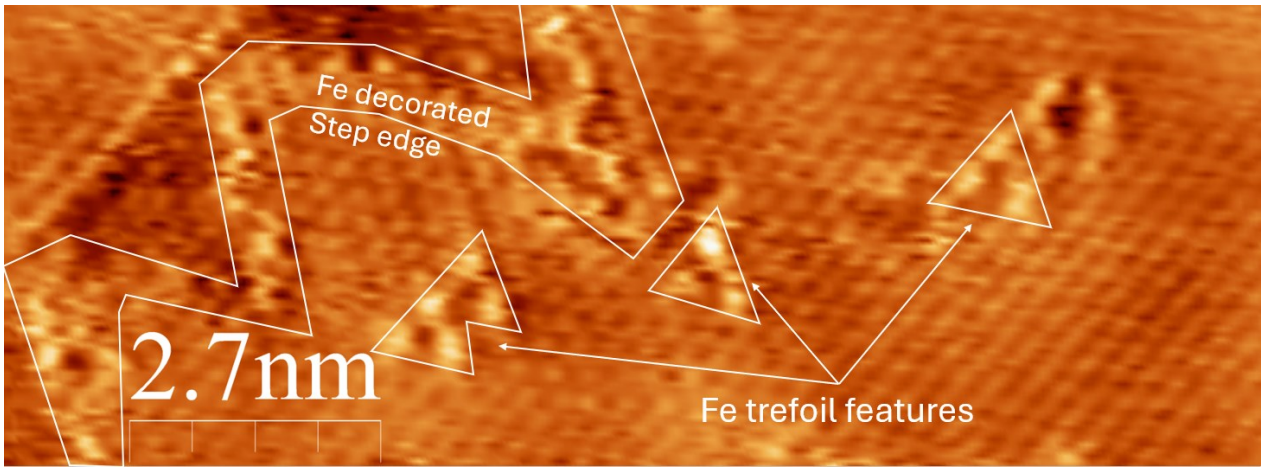

Figure 4.27 - (I=1.8nA, V=-0.6V, 14x5nm) Atomic resolution image showing both an Fe decorated step edge and characteristic trefoil features.

In contrast to what was observed in previous depositions, the deposited material seems to incorporate iron atoms that form rhomboidal or trefoil structures on the surface.

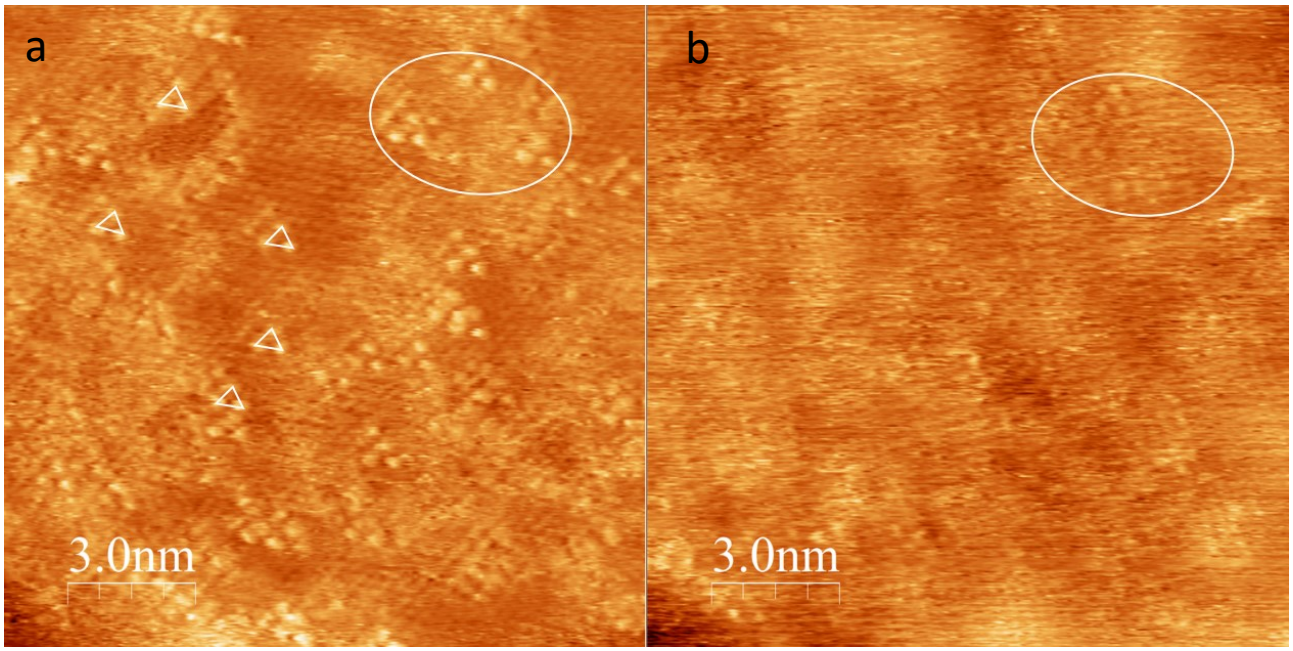

Figure 4.28 - (a) (I=2.4nA, V=-0.5V, 15x15nm) Atomic resolution image of the mixed material, with noticeable trefoils present on the surface, highlighted by white triangles. (b) (I=2.4nA, V=0.8V, 15x15nm) The same region imaged at opposite bias, which does not show the same trefoil features; highlighted in the white circle is the same area with now barely visible trefoil features.

The trefoil features were never observed in the as prepared MoS_2 and therefore are likely centers of iron incorporated into the MoS_2 lattice, in contrast to the separate phases observed in the first mixed deposition. These trefoils have an average distance between their atoms of 0.484 nm ±0.04 and are distributed seemingly

at random in the lattice. However, the trefoils all seem to orient their vertices preferentially along the direction of growth of the MoS_2 lattice, suggesting therefore that their bright features can be associated with specific crystallographic sites.

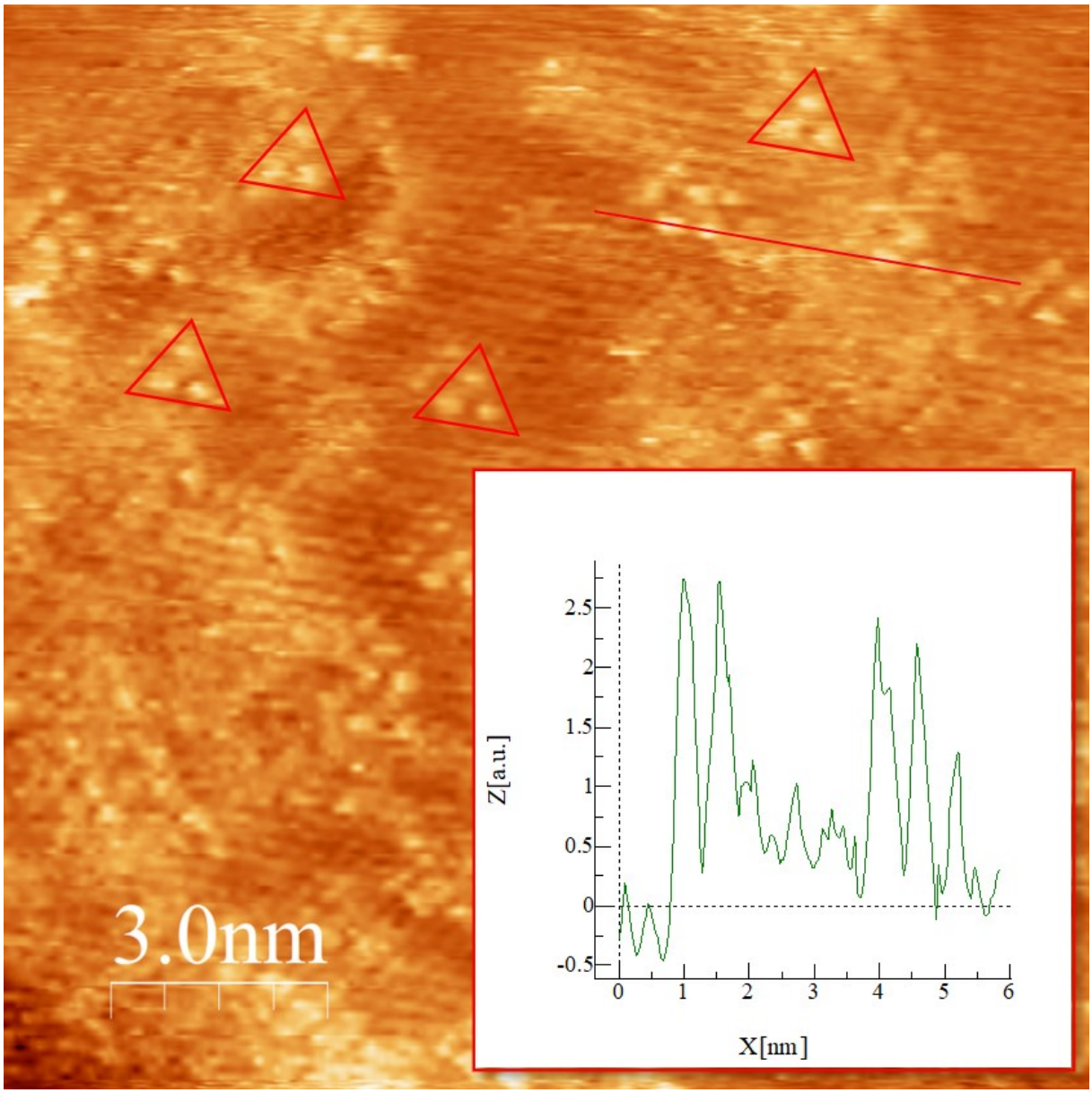

Figure 4.29 - (I=2.4nA, V=-0.5V, 15x15nm) Atomic resolution image of the film obtained in the mixed deposition; highlighted in red and shown in the inset is a line profile over four centers of two of the trefoils, which are highlighted in the red triangles.

The trefoils appeared brightly in the STM images only at negative biases, being only barely visible at any positive bias, as seen in the comparison in figure 4.28.

Both the observations for the first and second deposition of mixed Mo/Fe films indicate that the suflurized Fe/Mo phases tend to segregate on the surface of the Au (111) crystal and do not form a solid solution, detailing what was previously reported in the literature for FeS_2-loaded MoS_2 nanoparticles. [22,31] The trefoils observed in the second mixed material deposition seem to either form as inclusions into vacancies of the

MoS_2 film or the iron atoms decorating edges or holes. Previous theoretical works suggest indeed that the iron atoms likely do not enter the MoS_2 lattice, but prefer to adsorb on sites atop the Mo atom. [32] The formation of polynuclear iron sites on the MoS_2 surface is quite interesting from a catalysis perspective, since it has never been reported in the literature thus far, but on the other hand these species can exhibit useful and versatile reactivity patterns. For example, it is well known that poly-iron compounds allow for oxygen fixation and C–H bond hydroxylation and in the broad field of electrocatalysis these multinuclear metal species can trigger bifunctional mechanism and provide new concerted reaction path capable to escape scaling relationships. [33,34]

Bibliography for chapter 4

1. Yu. Antipina, L., G. Kvashnin, A., B. Sorokin, P. & A. Chernozatonskii, L. The possible formation of a magnetic FeS 2 phase in the two-dimensional MoS 2 matrix. *Phys. Chem. Chem. Phys.* **18**, 26956–26959 (2016).
2. Heift, D. Iron Sulfide Materials: Catalysts for Electrochemical Hydrogen Evolution. *Inorganics* **7**, 75 (2019).
3. Ehlen, N. *et al.* Orbital-selective chemical functionalization of MoS 2 by Fe. *Phys. Rev. B* **108**, 195430 (2023).
4. Shi, Y. *et al.* Energy Level Engineering of MoS2 by Transition-Metal Doping for Accelerating Hydrogen Evolution Reaction. *J. Am. Chem. Soc.* **139**, 15479–15485 (2017).
5. Biesinger, M. C. *et al.* Resolving surface chemical states in XPS analysis of first row transition metals, oxides and hydroxides: Cr, Mn, Fe, Co and Ni. *Appl. Surf. Sci.* **257**, 2717–2730 (2011).
6. bvcrist. Iron Spectra – Fe metal. *The International XPS Database 1* https://xpsdatabase.com/iron-spectra-fe-metal/.
7. Iron | XPS Periodic Table - IT. https://www.thermofisher.com/uk/en/home/materials-science/learning-center/periodic-table/transition-metal/iron.html.
8. Fadley, C. S. & Shirley, D. A. Multiplet Splitting of Metal-Atom Electron Binding Energies. *Phys. Rev. A* **2**, 1109–1120 (1970).
9. *Handbook of X-Ray Photoelectron Spectroscopy: A Reference Book of Standard Spectra for Identification and Interpretation of XPS Data*. (Perkin-Elmer Corporation, Eden Prairie, Minn, 1992).
10. Nesbitt, H. W., Bancroft, G. M., Pratt, A. R. & Scaini, M. J. Sulfur and iron surface states on fractured pyrite surfaces. *Am. Mineral.* **83**, 1067–1076 (1998).
11. Pratt, A. R., Muir, I. J. & Nesbitt, H. W. X-ray photoelectron and Auger electron spectroscopic studies of pyrrhotite and mechanism of air oxidation. *Geochim. Cosmochim. Acta* **58**, 827–841 (1994).
12. Nesbitt, H. W. *et al.* Synchrotron XPS evidence for Fe2+-S and Fe3+-S surface species on pyrite fracture-surfaces, and their 3D electronic states. *Am. Mineral.* **85**, 850–857 (2000).

13. Nesbitt, H. W. & Muir, I. J. X-ray photoelectron spectroscopic study of a pristine pyrite surface reacted with water vapour and air. *Geochim. Cosmochim. Acta* **58**, 4667–4679 (1994).
14. Bronold, M., Kubala, S., Pettenkofer, C. & Jaegermann, W. Thin pyrite (FeS2) films by molecular beam deposition. *Thin Solid Films* **304**, 178–182 (1997).
15. Rosso, K. M., Becker, U. & Hochella, M. F. Atomically resolved electronic structure of pyrite {100} surfaces; an experimental and theoretical investigation with implications for reactivity. *Am. Mineral.* **84**, 1535–1548 (1999).
16. Arrouvel, C. Surfaces, Interfaces and Crystal Growth of Marcasite FeS2. *Mater. Res.* **24**, e20200383 (2021).
17. Rosso, K. M., Becker, U. & Hochella, M. F. Surface defects and self-diffusion on pyrite {100}: An ultra-high vacuum scanning tunneling microscopy and theoretical modeling study. *Am. Mineral.* **85**, 1428–1436 (2000).
18. Davis, E. *et al.* Growth of Well-Ordered Iron Sulfide Thin Films. *Phys. Chem. Chem. Phys.* **21**, (2019).
19. Becker, U., Munz, A. W., Lennie, A. R., Thornton, G. & Vaughan, D. J. The atomic and electronic structure of the (001) surface of monoclinic pyrrhotite (Fe7S8) as studied using STM, LEED and quantum mechanical calculations. *Surf. Sci.* **389**, 66–87 (1997).
20. Waychunas, G. A. Structure, Aggregation and Characterization of Nanoparticles. *Rev. Mineral. Geochem.* **44**, 105–166 (2001).
21. Rickard, D. Metastable Sedimentary Iron Sulfides. in *Developments in Sedimentology* vol. 65 195–231 (Elsevier, 2012).
22. Yang, Y. *et al.* MoS2/FeS Nanocomposite Catalyst for Efficient Fenton Reaction. *ACS Appl. Mater. Interfaces* **13**, 51829–51838 (2021).
23. Favaro, M. *et al.* In Situ Study of Graphene Oxide Quantum Dot-MoSx Nanohybrids as Hydrogen Evolution Catalysts. *Surfaces* **3**, 225–236 (2020).
24. He, W. *et al.* Variable valence Mo5+/Mo6+ ionic bridge in hollow spherical g-C3N4/Bi2MoO6 catalysts for promoting selective visible light-driven CO2 photoreduction into CO. *J. Energy Chem.* **80**, 361–372 (2023).

25. Gong, M. *et al.* A giant polyoxomolybdate molecular catalyst with unusual Mo6+/Mo5+ synergistic mechanism for oxidation of hydroxyfurfural under atmospheric pressure. *Fuel Process. Technol.* **242**, 107635 (2023).
26. Lunardon, M. *et al.* Catalytic Activity of Defect-Engineered Transition Me tal Dichalcogenides Mapped with Atomic-Scale Precision by Electrochemical Scanning Tunneling Microscopy. *ACS Energy Lett.* **8**, 972–980 (2023).
27. Brown, N. M. D., Cui, N. & McKinley, A. An XPS study of the surface modification of natural MoS2 following treatment in an RF-oxygen plasma. *Appl. Surf. Sci.* **134**, 11–21 (1998).
28. Lince, J. R. *et al.* Photoelectron spectroscopic study of the interaction of thin Fe films with the MoS2(0001) surface. *Surf. Sci.* **223**, 65–81 (1989).
29. Mondal, I., Moon, S. Y., Lee, H., Kim, H. & Park, J. Y. Two-dimensional FeS2-encapsulated Au: a quasi-epitaxial heterojunction for synergistic catalytic activity under photoelectrocatalytic water reduction. *J. Mater. Chem. A* **7**, 19258–19268 (2019).
30. Xian, H. *et al.* Environmental-sulfur-controlled surface properties of pyrite: a first principles PBE + U study. *Phys. Chem. Miner.* **48**, 20 (2021).
31. Xue, J.-Y. *et al.* In Situ Generation of Bifunctional Fe-Doped MoS2 Nanocanopies for Efficient Electrocatalytic Water Splitting. *Inorg. Chem.* **58**, 11202–11209 (2019).
32. Karthikeyan, J., Komsa, H.-P., Batzill, M. & Krasheninnikov, A. V. Which Transition Metal Atoms Can Be Embedded into Two-Dimensional Molybdenum Dichalcogenides and Add Magnetism? *Nano Lett.* **19**, 4581–4587 (2019).
33. Gunay, A. & Theopold, K. H. C−H Bond Activations by Metal Oxo Compounds. *Chem. Rev.* **110**, 1060–1081 (2010).
34. Huang, X. & Groves, J. T. Beyond ferryl-mediated hydroxylation: 40 years of the rebound mechanism and C–H activation. *JBIC J. Biol. Inorg. Chem.* **22**, 185–207 (2017).

Conclusions

In this thesis, a thin film of MoS_2 was produced on the surface of an Au (111) single crystal by Physical Vapor Deposition (PVD).

The Au crystal is first pre-heated and exposed to an atmosphere of sulfur vapor, keeping it in this environment, at high temperature, throughout the metal deposition and the subsequent post-deposition annealing to obtain optimal results. The e-beam evaporator introduces a stream of Mo vapor in the chamber and the reaction between sulfur and the metal occurs on the surface of the Au crystal. The prolonged exposure of the sample to sulfur vapors results in a MoS_2 film resistant to oxidization even after prolonged exposure to the atmosphere. During the synthesis, temperature control is crucial, and it is shown that a low temperature does not allow the reaction between molybdenum and sulfur on the surface of the crystal. State-of-the-art characterization techniques, such as XPS, STM, and LEED, show that the desired 2D film of MoS_2 is indeed produced on the surface of the Au crystal, with Mo^{4+} and S^{2-} ions forming a hexagonal mesh. Moreover, the film adopts a Stranski-Krastanov type of growth, by forming triangular islands that coalesce forming a first wetting layer, followed by the growth of 3D islands.

In the second part of the thesis, the direct deposition of iron vapors is attempted, however the Fe atoms form nanoparticles on the surface instead of being incorporated into the MoS_2 structure. The Iron atoms are not included in the film structure neither after annealing in sulfur atmosphere, but rather tend to migrate towards the step-edges and vacancies on the surface, eventually forming larger clusters of nanoparticles.

In order to force iron atoms inside the lattice of the MoS_2, an attempt was made to simultaneously deposit molybdenum and iron, sulfurizing them on the surface of the Au crystal, following a procedure similar to the one previously used to produce the pure MoS_2 film.

It was observed that an excessively high temperature leads to the degradation of the newly deposited material and to the diffusion of the iron metal atoms in the Au crystal, therefore the substrate temperature must be limited, but still high enough to guarantee an efficient sulfurization of the two metals. Eventually, by playing on different paraments (such as metal deposition rate, pressure of the sulfur vapor, etc.) and introducing post deposition thermal treatments it was possible to produce thin films of mixed molybdenum and iron sulfides.

Two different recipes were optimized: a first one at higher temperatures followed by annealing, which resulted in a MoS_2 film together with a segregated pyrite (111) phase, while the second one produced a MoS_2 layer densely decorated by highly dispersed iron atoms that present themselves as atoms decorating the step-edges or as previously unobserved trefoil-like structures. In either case it seems that on the Au (111) surface, FeS_2 and MoS_2 nucleate segregated from each other, and not even in the ultrathin regime a solid solution or interphase stabilized mixed phase can be formed.

As an internal reference, in order to understand the structural properties of the mixed phase, a film of pure sulfurized iron was deposited on the Au crystal, following a procedure similar to the other depositions.
In this case, quite unexpectedly the resulting material was a (100) oriented pyrite-like monolayer film on top of the Au (111) substrate. Both this pyrite-like structure and the trefoils features observed on the surface of the mixed Mo/Fe film are not reported in the literature and could be of interest for further studies as model catalysts.

Appendix A: UHV system

In this work the sample preparation, XPS, LEED and part of the STM characterization are done in a modified VG-Escalab MkII, shown in figure A1. At the center of the machine is the analysis chamber, surmounted by the XPS analyzer; the X-ray source can be seen just left of the analysis chamber, easily distinguishable by its red casing.

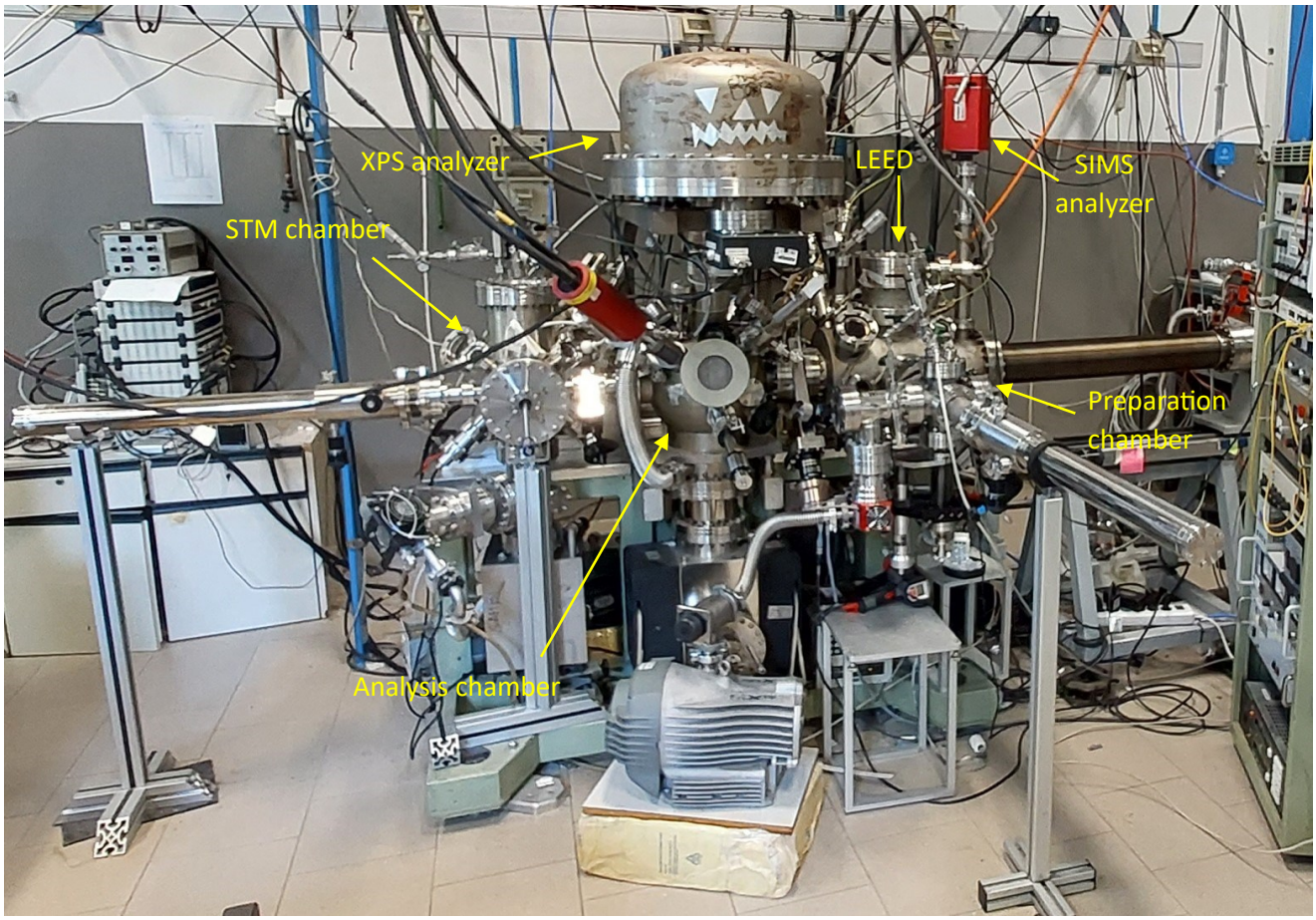

Figure A45 - VG-Escalab MkII with key components highlighted.

To the left of the analysis chamber lies the chamber that houses the STM, while to the right lies the preparation chamber. Just above the latter are visible the LEED housing (shown better in figure A2) and the SIMS analizer, also distinguishable by its red casing. Mounted on the sides of the STM and Preparation chamber are visible the housings of the manipulator arms used to move the sample inside the chambers.

In figure A2 is shown a close up of the preparation chamber (wrapped in aluminium foil) and the LEED housing above. Mounted on the preparation chamber is also visible the fast entry system used to introduce the samples inside the preparation chamber.

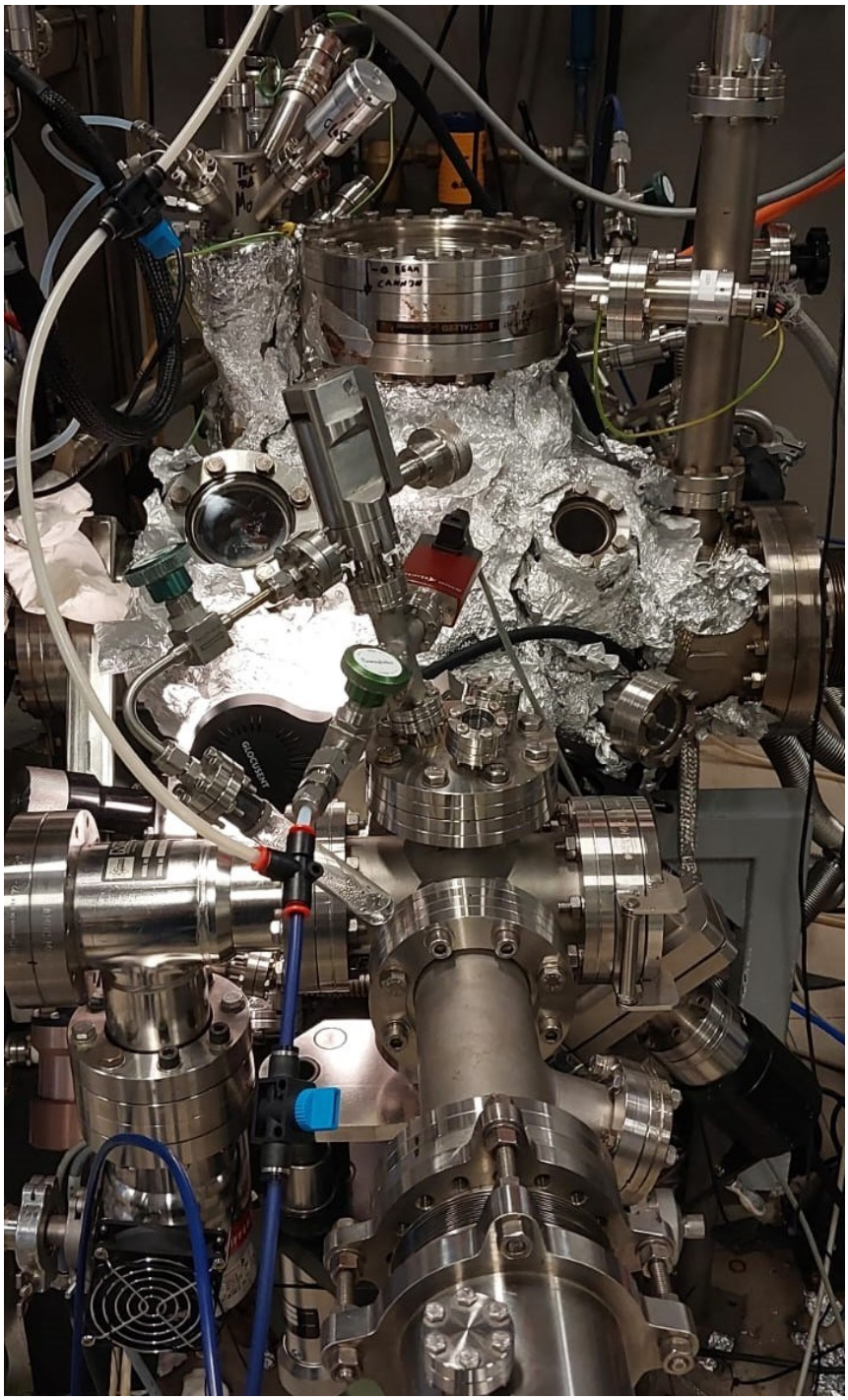

Figure A46 - Close up of the preparation chamber.

Appendix B: FeS_x fitting

In the following section are reported the reference values used to fit Fe 2p peaks obtained in the the FeS2 and mixed material depositions. The data was sourced from:

Nesbitt, H. W. *et al.* Synchrotron XPS evidence for Fe2+-S and Fe3+-S surface species on pyrite fracture-surfaces, and their 3D electronic states. *American Mineralogist* **85**, 850–857 (2000).

Type of peak	**Binding energy (eV)**	**FWHM (eV)**	**Peak Area (%)**
Fe^{2+} (bulk state)	707.0	0.85	50.3
Fe^{2+} (surface state)	707.7	1.10	16.5
1^{st} multiplet	708.2	1.10	8.9
2^{nd} multiplet	709.9	1.10	3.2
3^{rd} multiplet	712.1	1.10	3.1
Fe^{3+} (surface state)	708.9	1.10	10.1
1^{st} multiplet	709.8	1.10	4.8
2^{nd} multiplet	711.2	1.10	3.1

Ringraziamenti

Arrivato alla fine di questa spedizione in terra Patavina, penso che il Giangi abbia delle persone da ringraziare e di cui riconoscere l'importanza: tra gli alti e bassi sono grato di poter aver intrapreso questo percorso e di aver trovato molte persone e luoghi che ora sono incisi nella mia memoria.

Si ringraziano (in nessun ordine paricolare):

I miei genitori e la mia famiglia per avermi dato questa opportunità. Vi ho sempre voluto tantissimo bene e non posso ringraziarvi abbastanza per quello che avete fatto per me.

Al Prof. Agnoli e al Dr. Cattelan per la disponibilità e per avermi fatto affrontare una sfida che non è stata facile.

Alle ragazze e i ragazzi del Cadelfa, che mi hanno sopportato e che io ho dovuto sopportare in questi anni; ci si rivede la prossima riunione.

A Lucrezia, Enrico, Lavinia, Marco, Nicola, Martino, Matteo e gli altri amici della palestra, assieme a voi sono diventato più forte.

A Chiara, Ema, Alessandra, Michela, Ester, Gloria, Marco e gli altri amici di Padova, con cui ho condiviso bevute, mangiate, in alcuni casi overnight challenge, in altri casi un sacco di passi e in un caso in particolare delle gran cene.

A Bruno e alla Micky, sia per i caffé e le brioches, sia per le frasi di incoraggiamento e avermi spronato a continuare, nel bene e nel meno bene.

Al dipartimento di statistica per avermi ospitato per tutte quelle ore, nonostante non stessi studiando medicina.

Grazie ancora, ne è valsa la pena.